Subcycle dynamics of deep-strong light-matter coupling

DISSERTATION ZUR ERLANGUNG DES DOKTORGRADES DER NATURWISSENSCHAFTEN (DR. RER. NAT.) DER FAKULTÄT PHYSIK
DER UNIVERSITÄT REGENSBURG

vorgelegt von

Maike Halbhuber

aus Regensburg

im Jahr 2020

Das Promotionsgesuch wurde eingereicht am April 13, 2021.

Die Arbeit wurde angeleitet von Prof. Dr. Dominique Bougeard.

Prüfungsausschuss:

Vorsitzender:	Prof. Dr. John Schliemann
Erstgutachter:	Prof. Dr. Dominique Bougeard
Zweitgutachter:	Prof. Dr. Christian Schüller
Weiterer Prüfer:	Prof. Dr. Christoph Lange

Contents

1 Introduction

Quantum mechanics defines the intriguing concept of a quantum vacuum which is not empty, but rather permeated by zero-point electric field fluctuations. These fluctuations, called vacuum fluctuations, can be described by the creation and annihilation of virtual particle-antiparticle pairs on very short timescales. The population of vacuum fluctuations, existing in the ground state of every system, regardless of its boundary conditions, has fundamental implications: from the energy level shift of atoms, the Lamb-shift [1] to Unruh-Hawking radiation at the event horizon of black holes [2, 3]. The indirect detection, based on observation of effects caused by vacuum fluctuations, has been achieved for the Lamb-shift [1], the correction of the Landé g-factor [4] or the Casimir effect [5]. The direct detection of vacuum fluctuations, however, is quite challenging, as no energy can be extracted from the ground state of a system. A system where the quantum vacuum can still be directly studied is therefore highly sought after.

An interesting platform to study and control quantum vacua are light-matter coupled hybrid states in cavity quantum electro dynamics (cQED), where an electronic and a photonic excitation couple. The first observation of light-matter hybrid states, characterized by the repeated transfer of energy between a matter excitation, $\hbar\omega_{12}$ and a light mode $\hbar\omega_0$, has been achieved in 1983. Sodium atoms between a pair of mirrors, showed a periodic population and depopulation of an excited electron state within a few hundreds of nanoseconds [6]. As a result of this periodic absorption and emission novel light-matter hybrid states emerge. At resonance, the energy dispersion of these new eigenstates, called polaritons, is separated by the vacuum Rabi splitting. The interaction strength of light and matter is measured in terms of the vacuum Rabi frequency Ω_R, quantifying the rate of absorption and emission. Generally, a distinction between three different regimes of light-matter coupling is made: the weak coupling regime where losses exceed the energy

exchange rate, the strong coupling regime where the energy can be exchanged before it is lost from the system, and the ultrastrong coupling regime where the energy exchange rate is in the order of the frequency of the light mode.
For Ω_R approaching the carrier frequency of the light ω_0, anti-resonant interaction mechanisms affect the polaritons substantially, leading to an unusual ground state with a strongly increased population of virtual photons [7]. The ground state of these systems is, depending on the strength of coupling, a strongly modified, squeezed quantum vacuum populated with virtual cavity excitations [7]. Upon non-adiabatic modulation of the coupling, these excitations can be released as real radiation, providing an elegant way to directly detect vacuum photons [8].
In order to investigate virtual photons and control the quantum vacuum, a system that reaches ultimately high coupling strengths and whose ground state can be modulated on subcycle timescales is needed. Combining such a system with high sensitivity experiments opens up the possibility to measure vacuum photons. An experimental technique, where electric field correlations are analysed [9], very recently enabled the investigation of vacuum fluctuations in the terahertz (THz) frequency range [10]. Within the bandwidth of the electro-optic detection setup, this technique allowed for the analysis of the temporal and spatial coherence and the determination of the spectral components of vacuum fluctuations. Thus, this experimental scheme represents a very promising method to study vacuum photons released from the ground state of a time-modulated, ultrastrongly coupled system.
Since the unusual ground state of light-matter coupled systems strongly depends on the coupling strength, much effort has been put in the increase of the normalized coupling strength $\frac{\Omega_R}{\omega_0}$, eventually reaching the ultrastrong coupling regime. Here, Ω_R is in the order of ω_0. The first experimental demonstration of ultrastrong light-matter coupling with $\frac{\Omega_R}{\omega_0} > 0.1$ was achieved by intersubband polaritons in microcavity-embedded doped quantum wells [11], and has since been realized in various systems, such as superconducting circuits [12], Landau-quantized two-dimensional electron systems [13], organic molecules [14] or optomechanics [15]. Coupling strengths even exceeding unity have been reported [16, 17], accessing a new regime, the deep-strong coupling regime, characterized by coupling strengths $\frac{\Omega_R}{\omega_0} > 1$. Such high coupling strengths result in a considerably populated ground state, putting the detection of vacuum photons into reach.
Here, we concentrate on the most promising system for the realization of extremely strong

coupling in the deep-strong coupling regime: Landau-quantized electrons in high quality two-dimensional electron gasses dressed by the light field of sub-wavelength THz resonators [13]. Landau polariton systems are used to measure the effect of the vacuum field on the matter excitation in transport [18] and the Bloch-Siegert shift has been verified using Landau polaritons [19]. Further intriguing properties, such as light-matter decoupling [20], have been reported in these systems [17]. They also offer the possibility to custom tailor the vacuum mode through matter excitation and resonator design, making them perfect candidates to investigate the quantum vacuum and its effects, such as superradiant phase transitions [21, 22], the breakdown of the Purcell effect [20] and virtual photon induced nonlinear optics [23]. This system might unfold further possibilities to manipulate electronic properties, similar to light-induced superconductivity [24, 25], yet without injection of real photons. Cavity mediated superconductivity or cavity chemistry may also be realized in these systems.

The quantum vacuum of a light-matter coupled system and for it arising effects are defined by the coupling strength as well as by the dynamics of the system. Hence, this thesis is structured into two objectives:
Firstly, the enhancement of the coupling strength of inter-Landau transitions in two-dimensional electron gases (2DEGs) coupled to subwavelength THz resonators, by dedicated heterostructure development. This study will demonstrate unprecedentedly high coupling strengths, exceeding current records and opening up an interesting platform to study cQED effects.
Secondly, the non-adiabatic modulation of a deep-strongly coupled system, giving insight into the physics of decoupling on extremely subcycle timescales. Combination of high quality 2DEGs and an optically switchable THz resonator, designed within this thesis, will enable the femtosecond study of light-matter interaction dynamics.

This thesis is organized in the following way:
In Chapter 2 the fundamental concepts and fascinating properties of light-matter coupling in the deep-strong coupling regime are briefly reviewed. Here, we also discuss possibilities to enhance the coupling strength and increase the vacuum Rabi frequency Ω_R, concluding with the presentation of a very promising system for ultimately strong light-matter coupling. Chapter 3 summarizes relevant experimental methods to produce deep-strongly coupled

structures and study their dynamics. In Chapter 4 the experimental results of coupling different material systems to THz resonators are presented. We start with AlGaAs/GaAs heterostructures, comprising of a high number of tightly stacked quantum wells (QW) and continue the improvement of the matter part, by developing multi-QW stacks of InAlAs/InGaAs/InAs and AlSb/InAs heterostructures. Coupling a 6-fold QW stack of the later material system, results in a record high normalized coupling strength of $\frac{\Omega_R}{\omega_0} = 2.76$. In Chapter 5 we demonstrate an optically switchable resonator, compatible with AlGaAs/GaAs heterostructures. This resonator facilitates the selective intensity modulation of the field amplitude of the fundamental resonator mode in less than 1 ps, opening up the possibility of non-adiabatic modulation of deep-strong coupling. In Chapter 6 we show the decoupling dynamics of structures in the deep-strong coupling regime. Femtosecond reshaping of the light mode by photo-excitation of the subcycle switchable resonator, results in novel sub-polariton-cycle oscillations of the response function of the system. The findings of Chapter 5 and 6 have been reported in ref. [26]. Chapter 7 summarizes the results of this work and gives perspectives on possible directions joining ultimately strong coupling and subcycle switchable resonators.

2 Deep-strong light-matter coupling

In light-matter coupled systems, energy is periodically exchanged between a light mode and a matter excitation. A simple model of an optical resonator containing a two-level system, depicted in Fig. 2.1, can be used to describe light-matter coupling. At resonance, the resonance frequency ω_0 of the optical cavity is equal to the transition energy of the matter excitation $\hbar\omega_{12} = \hbar\omega_0$, with the transition frequency ω_{12}. This allows for the repeated exchange of energy, as a photon inside the cavity is absorbed and reemitted by the two-level system. This process is periodic with the vacuum Rabi frequency Ω_R and is limited by the losses of the system. The interaction of light and matter can be categorized into different regimes depending on the coupling strength Ω_R and the losses of the system. In the weak coupling regime, the loss rate γ is greater than the energy exchange rate Ω_R, therefore the energy is lost from the system before the energy is transferred from light to matter mode or vice versa. In this regime, the spontaneous emission is altered leading to the Purcell effect [27]. For strong coupling, γ is smaller than Ω_R: It is possible to observe the oscillatory

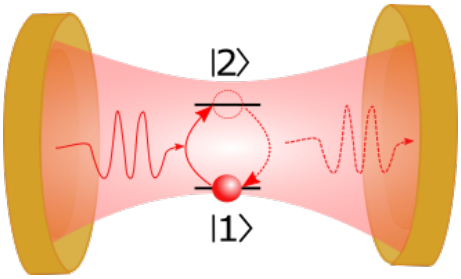

Figure 2.1: Light-matter coupling model. Scheme of a two-level system located in an optical resonator. The energy of the system is periodically exchanged between the matter excitation and the light mode: The photon (indicated by a wave function) is absorbed, exciting the two-level system, and subsequently reemitted.

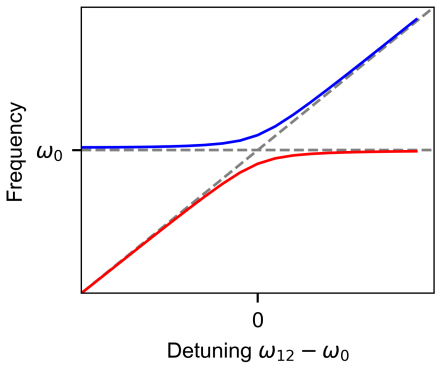

Figure 2.2: Anti-crossing of two resonances for strong coupling. The cavity resonance ω_0 and the tunable matter resonance ω_{12} do not cross at zero detuning (grey dashed lines), but split. The new eigenstates, the upper (UP, blue line) and the lower (LP, red line) polariton, are separated by $2\Omega_R$.

energy exchange between matter and light [28, 29]. This interaction, describable with the rotating-wave approximation [30], gives rise to new quasi-particle eigenstates, called cavity polaritons. Their energy is separated by $\Delta\omega = 2\Omega_\mathrm{R}$, proportional to the energy exchange rate. The energy splitting of the resonances of such a system is shown in Fig. 2.2, where the matter transition frequency ω_{12} is detuned with respect to the cavity frequency ω_0. At the anti-crossing point (ACP) where the detuning is zero, hence $\omega_0 = \omega_{12}$, the resonances do not cross, but are split by $2\Omega_\mathrm{R}$. The resulting new eigenstates are called upper polariton (UP, blue line in Fig. 2.2) and lower polariton (LP, red line in Fig. 2.2).

For a coupling strength that is even further increased a third regime is accessed: the ultrastrong coupling (USC) regime, where the normalized coupling strength $\frac{\Omega_\mathrm{R}}{\omega_0}$ approaches unity. If the ratio even exceeds unity, the deep-strong coupling regime is reached. In systems characterized by coupling strengths in the ultra- and deep-strong coupling regime, the rotating-wave approximation of light-matter interaction is no longer applicable, as anti-resonant coupling terms become relevant [7] and strongly influence the properties of the system.

2.1 Theoretical description of light-matter coupling

In the following, a quantum mechanical description of light-matter coupled systems and their inherent properties are presented. In order to describe light-matter interaction (LMI), we start with the quantum Rabi model [31], representing the interaction between a cavity mode and a single two level system. The Rabi Hamiltonian

$$\hat{H}_{\text{Rabi}} = \hbar\omega_0\hat{a}^\dagger\hat{a} + \hbar\frac{1}{2}\omega_{12}\hat{\sigma_z} + \hat{H}_{\text{int}}, \tag{2.1}$$

where $\hat{a}^\dagger$ and $\hat{a}$ are the creation and annihilation operators of the cavity, and $\hat{\sigma_z}$ the Pauli operator, representing $|e\rangle\langle e| - |g\rangle\langle g|$, with the excited state $|e\rangle$ and the ground state $|g\rangle$. $\hat{H}_{\text{int}}$, accounting for the interaction between the bosonic light field and the two level system, assumes the form:

$$\hat{H}_{\text{int}} = \hbar g_1(\hat{a}\hat{\sigma_+} + \hat{a}^\dagger\hat{\sigma_-}) + g_2(\hat{a}\hat{\sigma_-} + \hat{a}^\dagger\hat{\sigma_+}), \tag{2.2}$$

with the lowering ($\hat{\sigma_-}$), and raising ($\hat{\sigma_+}$) operator of the two-level system. g_1 and g_2, representing the coupling strengths, weight the two parts of light-matter interaction. The first part describes the resonant interaction: absorption and emission of a photon, keeping the total number of excitations N constant. The second part, on the other hand, which accounts for the anti-resonant terms, does not conserve N. Applying the rotating wave approximation ($g_2 = 0$), therefore omitting the anti-resonant terms, leads to the known Jaynes–Cummings model (JCM) [30], which is used to describe the weak and strong coupling regime. Yet in the deep- and ultrastrong coupling regime [32], where the interaction effectively extents over a large frequency range, the rotating wave approximation looses its validity and the anti-resonant terms become relevant. Following the quantum Rabi model the coupling strength $g = g_1 = g_2$ scales the anti-resonant terms. Concluding, in the ultrastrong coupling regime, processes that do not conserve the number of excitations N, define the characteristics of light-matter interaction.

To describe not only the interaction of a cavity with a single two level system, but also the coupling of light to an ensemble of excitations, a model of two coupled harmonic

oscillators is used. The ensemble of matter excitations is represented by the creation $\hat{b}^\dagger$ and annihilation operator $\hat{b}$. The purely bosonic multi-mode Hopfield model [33], enables such a treatment. The Hamilton for a single cavity mode (ω_0) coupling to a collective matter mode (ω_{12}) with the coupling strength represented by the vacuum Rabi frequency Ω_R reads in the simplified two-mode Hopfield model [7]:

$$\hat{H}_\mathrm{LMI} = \hat{H}_\mathrm{cavity} + \hat{H}_\mathrm{matter} + \hat{H}_\mathrm{int} + \hat{H}_\mathrm{dia}, \tag{2.3}$$

with

$$\hat{H}_\mathrm{cavity} = \hbar\omega_0 \hat{a}^\dagger \hat{a}, \tag{2.4}$$

$$\hat{H}_\mathrm{matter} = \hbar\omega_{12} \hat{b}^\dagger \hat{b}, \tag{2.5}$$

$$\hat{H}_\mathrm{int} = \hbar\Omega_\mathrm{R} \left(\hat{a} + \hat{a}^\dagger\right)\left(\hat{b} + \hat{b}^\dagger\right), \tag{2.6}$$

and

$$\hat{H}_\mathrm{dia} = \hbar\frac{{\Omega_R}^2}{\omega_0}\left(\hat{a} + \hat{a}^\dagger\right)^2. \tag{2.7}$$

$\hat{H}_{dia}$ describes a purely photonic contribution called the diamagnetic term, which leads to a blueshift of the cavity mode. This effect scales with $\frac{\Omega_\mathrm{R}^2}{\omega_0} = D$. Following [7], the Hamiltonian can be diagonalized by introducing the polariton annihilation $\hat{p}_i$ and creation $\hat{p}_i^\dagger$ operators with i = {LP, UP} and:

$$\hat{p}_\mathrm{i} = w_\mathrm{i}\hat{a} + x_\mathrm{i}\hat{b} + y_\mathrm{i}\hat{a}^\dagger + z_\mathrm{i}\hat{b}^\dagger. \tag{2.8}$$

The Hopfield coefficients w_i, x_i, y_i, z_i satisfy the normalization condition: $|w_\mathrm{i}|^2 + |x_\mathrm{i}|^2 - |y_\mathrm{i}|^2 - |z_\mathrm{i}|^2 = 1$. The Hamiltonian

$$\hat{H}_\mathrm{LMI} = \sum \hbar\omega_\mathrm{i}\hat{p}_\mathrm{i}^\dagger\hat{p}_\mathrm{i}, \tag{2.9}$$

is diagonalized as $\left[\hat{p}_\mathrm{i}, \hat{H}_\mathrm{LMI}\right] = \hbar\omega_\mathrm{i}\hat{p}_\mathrm{i}$. The eigenvalue problem then takes the form:

$$M v_\mathrm{i} = \hbar\omega_\mathrm{i} v_\mathrm{i}, \tag{2.10}$$

with the Hopfield matrix

$$\mathcal{M} = \begin{pmatrix} \omega_0 + 2D & \Omega_\mathrm{R} & 2D & \Omega_\mathrm{R} \\ \Omega_\mathrm{R} & \omega_{12} & \Omega_\mathrm{R} & 0 \\ -2D & -\Omega_\mathrm{R} & -\omega_{12} - 2D & -\Omega_\mathrm{R} \\ -\Omega_\mathrm{R} & 0 & -\Omega_\mathrm{R} & -\omega_{12} \end{pmatrix}, \tag{2.11}$$

the polariton energies $\hbar\omega_\mathrm{i}$ and the eigenvectors

$$v_\mathrm{i} = \begin{pmatrix} w_\mathrm{i} \\ x_\mathrm{i} \\ y_\mathrm{i} \\ z_\mathrm{i} \end{pmatrix}. \tag{2.12}$$

Considering the resonant case ($\omega_0 \rightarrow \omega_{12}$), the polariton energy dispersion can be calculated:

$$\omega_\mathrm{i} = \sqrt{\omega_{12}^2 + \Omega_\mathrm{R}^2} \pm \Omega_\mathrm{R}. \tag{2.13}$$

Fig. 2.3a shows the highly asymmetric polariton dispersion as a function of the normalized coupling rate $\frac{\Omega_\mathrm{R}}{\omega_0}$. This asymmetry stems from the anti-resonant terms of the light-matter interaction and the diamagnetic blueshift of the cavity resonance. To determine the coupling strength of a given polariton dispersion, a fitting procedure that is based on this Hopfield formalism is applied. The best fit of the Hopfield Hamiltonian fitted to the investigated polariton frequencies with $\frac{\Omega_\mathrm{R}}{\omega_0}$ as fit parameter provides the coupling strength. The Hopfield coefficients (Figs. 2.3b and c) determine the mixing fractions of light (w_i, y_i) and matter (x_i, z_i) for each polariton. One distinguishes between the normal (w_i, x_i) and the anomalous (y_i, z_i) coefficients which only become relevant in the ultra- and deep-strong coupling regime. They significantly increase with Ω_R, becoming eventually of the same order as the normal ones. Fig. 2.3b shows the evolution of the mixing fractions for the LP: For small coupling strengths, y_i, z_i are negligible and the normal mixing fractions are almost equal. Therefore the LP is equally light- and matter-like. But for higher coupling strengths, owing to the effects of the anti-resonant terms in the USC limit, the LP becomes more matter like. For the UP on the other hand (Fig. 2.3c), the Hopfield coefficients become increasingly light-like for rising coupling strengths. These signatures of the ultrastrong

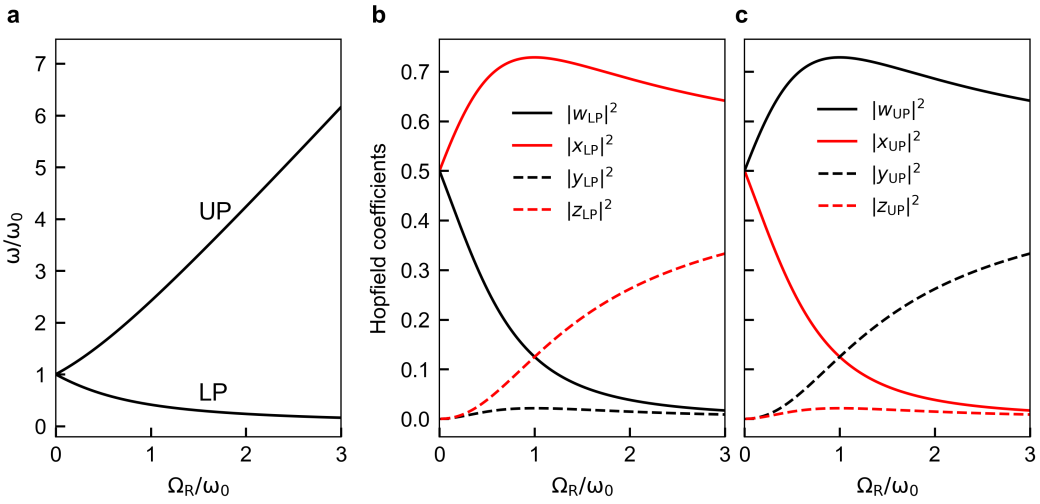

Figure 2.3: Frequency of the cavity polaritons and Hopfield coefficients in dependence of the normalized coupling strength $\frac{\Omega_R}{\omega_0}$. (a) The highly asymmetric polariton dispersion of LP and UP. Hopfield coefficients of LP (b) and UP (c). Evolution of the mixing fractions as a function of the coupling strength $\frac{\Omega_R}{\omega_0}$: The normal coefficients (w_i, x_i, solid lines) are dominant for small coupling strengths, whereas the anomalous coefficients (y_i, z_i, dashed lines) become relevant for increasing coupling strength.

light-matter coupling regime have been observed experimentally [11, 34], which underlines the importance of the anomalous contributions in the USC regime. However, there are numerous effects predicted [32] for especially strong light-matter coupling: squeezed states [7, 35], Dicke superradiant phase transitions [36] and the modified standard quantum phenomena, such as the collapse of the Purcell effect [20], photon blockade [37, 38] or photon transfer [39]. Recently, modified properties of the matter system are studied in cavity-controlled chemistry [40–43], seeking to control chemical reactions, photo-mediated superconductivity [44, 45] and magneto-transport measurements [18, 46, 47]. In the following, effects arising for the strongly modified vacuum ground state of a light-matter coupled systems are discussed.

2.2 Properties of deep-strongly coupled quantum vacua

Light-matter interaction in the USC-regime strongly modifies the vacuum ground state of a coupled system. Here, a brief overview of predicted as well as already demonstrated features of this modified state is given.

As detailed in ref. [7], the ground state in the USC-regime is, in contrast to a system described by the JCM, a squeezed state, containing virtual light and matter excitations. Owing to the anti-resonant terms in $\hat{H}_{\mathrm{LMI}}$, that become relevant in the USC regime, the ground state $|G\rangle$ no longer fulfils $\hat{a}\,|G\rangle = \hat{b}\,|G\rangle = 0$. Thus, there is a finite number of cavity and matter excitations in the ground state. The vacuum ground state, on the other hand, now satisfies $\hat{p}\,|G\rangle = 0$. Because of this, there is a vanishing number of polariton excitations. Since the polariton annihilation operator is a superposition of the cavity and matter mode operators, the ground state $|G\rangle$ is a squeezed state. The cavity and matter modes can on the other hand be expressed in terms of the polariton operators. This allows the calculation of the number of cavity photons and matter excitations contained in the ground state:

$$\langle G|\,\hat{a}^{\dagger}\hat{a}\,|G\rangle = |y_{\mathrm{UP}}|^2 + |y_{\mathrm{LP}}|^2 \tag{2.14}$$

and

$$\langle G|\,\hat{b}^{\dagger}\hat{b}\,|G\rangle = |z_{\mathrm{UP}}|^2 + |z_{\mathrm{LP}}|^2\,. \tag{2.15}$$

As the photonic population, composed of virtual photons, is determined by the anomalous coefficients it is strongly dependent on the coupling strength. Fig. 2.4 shows that the vacuum population of the cavity increases nonlinearly with increasing coupling strength. However, the virtual excitations are not able to leave the cavity, so the ground state photons cannot be directly detected. Possible ways to probe them indirectly are to measure the Lamb shift they produce [48] or to detect the radiation pressure arising for a system with an opto-mechanical cavity [49].

In a static case, these excitation dressing the ground state are purely virtual. To directly detect them, they would need to be converted to real excitations. This can be achieved by a rapid, non-adiabatic modulation of Ω_{R}, the coupling strength [7, 8]. The real photons can then be extracted from the system and be detected. Following this idea in analogy to the

dynamical Casimir effect [5, 50], an abrupt switch-off of Ω_R, deactivating the coupling, results in new eigenstates: the eigenstates of the uncoupled systems. The polaritons are no longer eigenstates, but the cavity is still populated, as the perturbation is non-adiabatic. Therefore, the photon mode remains squeezed. In the uncoupled system, this state is now an excited state which relaxes to the ordinary vacuum ground state. This transition happens by emitting the initially virtual photons as real radiation, called vacuum photons. Owing to the small number of these photons, the experimental detection of them has not yet been achieved. Therefore, the main objective of this work is to pave the way for the detection of vacuum photons by non-adiabatically modulation of ultimately high coupling strengths.
The increased population of the ground state holds also true if many atoms are coupled to the light, a scenario described by the Dicke model [36]. Here, a superradiant phase transition is predicted to occur for a critical coupling strength [21, 22]. The quantum phase transition separates the ground state into phases containing photons and phases without photons. The effects of the modified vacuum of light-matter coupled systems have also been studied in magneto-transport measurements, revealing the influence of the vacuum field even without excitation of the cavity [18].
A promising measurement scheme for the detection of vacuum photons is presented by Benea-Chelmus et al. [10], where vacuum field fluctuations are determined by directly measuring the field correlation of the fluctuations. This scheme can be extended to measure emitted photon pairs, of a non-adiabatically modulated light-matter coupled system. Another way to directly measure vacuum fluctuations is to study the noise amplitude of unperturbed vacuum, as done by Riek et al. [51] or with cutting edge electro-optic sampling of few-cycle field transients [52].
In order to increase the number of virtual excitations, which scales with $\frac{\Omega_R}{\omega_0}$, the normalized coupling strength of the system needs to be maximized. This is, next to a non-adiabatic modulation of $\frac{\Omega_R}{\omega_0}$, the main goal of this work.

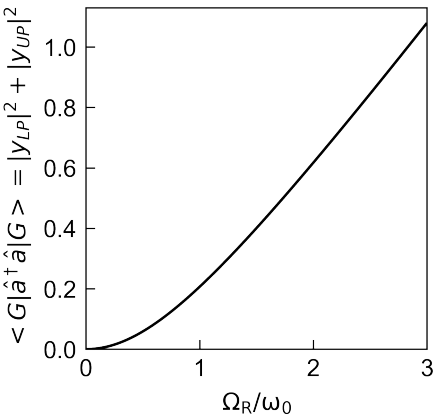

Figure 2.4: Vacuum photon population as a function of the coupling strength $\frac{\Omega_R}{\omega_0}$. The vacuum photon population of the ground state, given by $|y_{LP}|^2 + |y_{UP}|^2$, increases nonlinearly with the coupling strength $\frac{\Omega_R}{\omega_0}$.

2.3 Enhancing the coupling strength

Since many highly anticipated effects, such as the conversion of virtual to real vacuum photons, scale with the normalized coupling strength, a lot of effort has been put into its maximisation. This has been done for a variety of systems [11, 13, 16, 17, 53–60]. In this section, the possibilities to reach extremely strong light-matter coupling are discussed.
For a single two level system in a light field E_{vac}, the vacuum Rabi frequency

$$\Omega_R = \frac{d_{\text{matter}} E_{\text{vac}}}{\hbar} \tag{2.16}$$

depends on the transition dipole of the matter excitation d_{matter}. If the light is not only coupled to a single transition, but to an ensemble of n excitations, Ω_R also depends on the number of excited oscillators. For a collective excitation, Ω_R then reads:

$$\Omega_R = \frac{\sqrt{n} d_{\text{matter}} E_{\text{vac}}}{\hbar}. \tag{2.17}$$

The coupling light field E_{vac} can be expressed by

$$E_{\mathrm{vac}} = \sqrt{\frac{\hbar\omega_0}{2\epsilon V_{\mathrm{vac}}}}, \tag{2.18}$$

the root mean square of the vacuum fluctuations, which dress the matter excitation, with the cavity mode volume V_{vac} and the dielectric function ϵ. The resulting dependence

$$\Omega_{\mathrm{R}} = \sqrt{\frac{n d^2_{\mathrm{matter}}\omega_0}{\hbar 2\epsilon V_{\mathrm{vac}}}}, \tag{2.19}$$

clearly points out possibilities to enhance Ω_{R}. Considering that the coupling strength is normalized to the central frequency ω_0 the following steps can be taken to reach ultimately strong light-matter coupling:

Low frequencies

The Rabi frequency is normalized to the resonance frequency of the system, yielding $\frac{\Omega_{\mathrm{R}}}{\omega_0} \propto \omega_0^{-1/2}$. Therefore low central frequencies are desired to increase the ratio.

High dipole moments

The strength of a radiative transition, which couples to a light field, is determined by the dipole moment. In order to get strong transitions, a matter system with a high dipole moment is needed.

High number of matter excitations

Simultaneous coupling of n matter excitations to the light mode of the cavity enhances Ω_R by a factor of $\sqrt{n}$.

Small mode volume

The vacuum mode volume V, should be as small as possible, as the vacuum field and therefore Ω_{R} scales with $\frac{1}{V}$.

Sample geometry

The matter excitation should be placed in the region of highest field strength of the vacuum field of the resonator.

The experimental realization of ultrastrong coupling in different systems progresses steadily. It has been achieved in systems ranging from microcavities embedding doped quantum wells [11, 13, 17, 58] and superconducting quantum circuits [12, 16] to organic molecules [14, 59] and optomechanics [57]. The system to first demonstrate deep-strong coupling, was a superconducting qubit-oscillator circuit [16], where the photon field is coupled to an artificial atom formed by Josephson junctions. In such a system, the dynamical Casimir effect, where vacuum fluctuations are converted into pairs of real photons, has been observed [50]. All-optical systems which reach the ultrastrong coupling regime are intersubband polaritons [11, 58] and Landau polaritons [13, 17, 18, 55, 61]. The highest coupling strength are almost continuously reported for coupling of Landau-quantized electrons of high quality 2DEGs to subwavelength THz resonators. In this system, Bayer et al. [17] reached the record coupling strength of $\frac{\Omega_R}{\omega_0} = 1.43$. This was realized through an unified treatment of both the matter excitation and the light mode. In the following section, this very promising system to achieve ultimately high coupling strengths is presented.

2.4 Coupling of cyclotron resonances to THz resonators

The experimental realization of deep-strong coupling is quite challenging, but has been demonstrated in superconducting qubit-oscillators [16] and optical systems resulting in plasmon polaritons [60] or Landau polaritons [17]. In this particular system, the cavity field of a strongly sub-wavelength resonator is coupled to a Landau-quantized two-dimensional electron gas [13]. This is a promising way to achieve the highest coupling strengths and observe highly unusual effects of the deep-strong coupling regime. In the following, the light part, the field of a THz-resonator, and matter part, Landau-quantized electrons which offer high dipole moments, as well as possibilities to optimize the coupling strength between them are discussed. The design of the coupled structures is based on numerical simulations which enable the numerical calculation of the electric properties of the deep-strongly coupled system. These simulations are also presented in the following chapter.

2.4.1 Landau-quantized 2DEGs

Heterostructures, compositions of different semiconductors brought together, enable the precise manipulation of the energy dispersion of electrons in condensed matter [62]. At the interface of different materials, the energy bands can shift in a way that the conduction band (CB) of the well material lies below the Fermi energy. This leads to an occupation of the CB with free electrons. Their movement is confined by the potential barrier of a material with a larger band gap energy. A potential well for the electrons in the CB forms. If the extension of this potential well in z-direction is at the order of the De Broglie wavelength of the electrons, the confinement leads to quantization of the energy dispersion, resulting in the formation of a 2DEG. Such 2DEGs constitute the matter part of our coupled systems. In a static magnetic field B, the electron movement perpendicular to B can be described by the Hamiltonian of a harmonic oscillator [63], with equidistant level spacing (schematically depicted in Fig. 2.5a). In the Landau-quantization, for the first time described by L. Landau [64], the density of states (DOS, schematically depicted in Fig. 2.5b) transforms into equidistant Landau levels (LL) separated by

$$E = \hbar\omega_c = \hbar\frac{eB}{m^*}, \tag{2.20}$$

with cyclotron resonance (CR) frequency ω_c and the effective mass m^* of the electrons. The degeneracy, which is the same for each level, causes the occupation up to the νth level, with the filling factor

$$\nu = \frac{2\pi\rho_{2DEG}\hbar}{eB}, \tag{2.21}$$

where ρ_{2DEG} is the electron density in the 2DEG. A LL is therefore filled with $\rho_{LL} = \frac{eB}{h}$. The selection rules for dipole transitions of electrons in a Landau system correspond to the quantum mechanical harmonic oscillator:

$$\Delta n = \pm 1. \tag{2.22}$$

Radiative transitions, only allowed between adjacent Landau levels, assume a dipole moment

$$d_{\text{matter}} = el_0\sqrt{\nu}, \tag{2.23}$$

with the elementary charge e and the magnetic length $l_0 = \sqrt{\frac{\hbar}{eB}}$. The extremely high dipole moment of LL transitions is about three magnitudes larger, than for atomic transitions which scale only with the Bohr radius.
Following ref. [65], describing the coupling of Landau-quantized electrons and cavity resonators, eq. 2.17 assumes the form:

$$\Omega_R \hbar = \sqrt{\frac{\rho_{2DEG}}{\nu}} e l_0 \sqrt{\nu} E_{vac}. \tag{2.24}$$

The coupling strength is enhanced by the number of participating electrons $\frac{\rho_{2DEG}}{\nu}$ in the ν-th LL, since for weak excitation the transition is between the ν-th and the $(\nu+1)$-th level. For multi quantum well stacks, a collective enhancement of Ω_R is caused by coupling of electrons in the n_{QW} quantum wells, effectively increasing the number of coupled excitations. If all QWs are coupled identically the number of participating electrons is $\frac{n_{QW} \times \rho_{2DEG}}{\nu}$. However, for an unequal coupling of the QWs caused by a decreasing vacuum field over the QW stack, Ω_R scales as: $\Omega_R(n_{QW}) = \sqrt{n_{QW,eff}} \times \Omega_R(1)$. Here, the effective number of quantum wells $n_{QW,eff}$ amounts for the unequal cavity mode distribution in the QWs and $\Omega_R(1)$ is the Rabi frequency of the first QW alone. For a cavity mode that decays exponentially away from the metasurface with the decay length L_z, the effective number of QWs spaced at Δz can be calculated according to ref. [55] as follows: $n_{QW,eff} = \frac{1-e^{L_z \Delta z n_{QW}}}{1-e^{L_z \Delta z}}$. However, since the light mode of the coupled system is influenced by dielectric function of the 2DEGs, the decay is non-exponential [17]. Therefore, deviations from this prediction are expected, causing the exact value of $n_{QW,eff}$ to be inaccessible.
Resuming the discussion, the following relations is obtained:

$$\frac{\Omega_R}{\omega_0} \propto \sqrt{\nu \times n_{QW,\,eff}}. \tag{2.25}$$

This clearly shows possibilities to increase the coupling strength by heterostructure design: Firstly, the number of excitations can be increased by the number of QWs and the sheet carrier density of the 2DEG. Secondly, the filling factor and therefore the dipole moment of a 2DEG for a given transition frequency $\omega_c = \omega_0$ is higher for lower effective masses m^*. Therefore in order to enhance the coupling strength, which scales with the transition dipole moment, a 2DEG with low effective electron masses is desired.

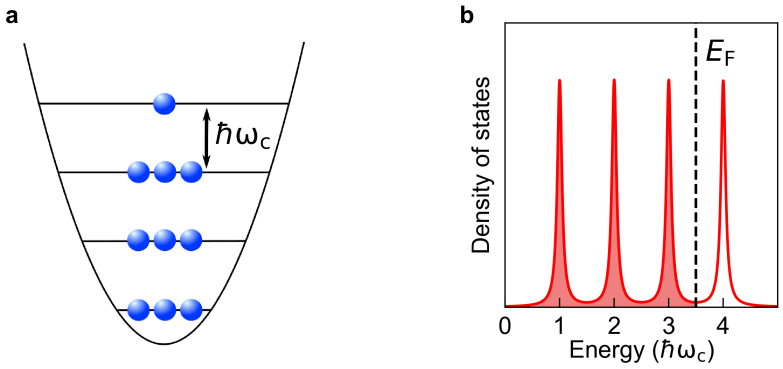

Figure 2.5: Landau-quantization of free electrons. (a) The Landau-quantized electrons are described by a harmonic oscillator, with an equidistant level spacing of $E = \hbar\omega_c$. (b) Density of states of a 2DEG, with applied magnetic field. The discrete Landau level are filled up to the Fermi-energy E_F. The filling factor, here $\nu = 3$, quantifies the population of the levels depending on the magnetic field.

However, Landau-quantization of electrons is only provided if the electron mobility $\mu_e = \frac{e\tau_{\text{scatter}}}{m^*}$ fulfils:

$$\tau_{\text{scatter}} > \frac{1}{\omega_c}, \tag{2.26}$$

with the time τ_{scatter} defining the time between scattering events. Only then can the electrons perform at least one complete cyclotron orbit without scattering. In this thesis, three different material systems comprising multiple QW stacks, which were optimized by high doping densities and low effective masses, are presented.

2.4.2 Subwavelength THz resonators

As the cyclotron transition in 2DEGs constitutes the matter part for our light-matter coupling experiments, a suitable resonator in the low THz regime, corresponding to the CR transition energy, is needed. Metasurfaces, consisting of arrays of split ring resonators, so called metamaterials (MM), offer the possibility to control electro-magnetic waves in this frequency regime [66, 67]. At resonance, metamaterials manipulate the waves on a subwavelength scale by confining the radiation in a small volume. This results in high electro-magnetic fields, which can be used to dress Landau-electrons in the cavity volume. Here, we use more complex forms of metallic split ring resonators [68], featuring

a capacitive gap element and connecting line elements. For an incident THz field, such structures can be described analogous to a RLC-circuits. The inductance (L) results from the currents induced by the incident THz field, conducted along the line elements. Gaps perpendicular to the incident field in the metal form the capacitance (C). The resistor (R) represents the losses of the resonator. The characteristic resonance frequency, called LC resonance, is defined by the geometry and the size of the resonator. The capacitive elements, the gap elements, are designed to confine this light mode into a small volume.
In this thesis, we used four different metamaterial designs, which will be called MM I - MM IV. Fig. 2.6a and b show the geometry of positive structures, the resonator MM I and MM II respectively. These structures comprising line and gap elements consist of gold (Au) on a not-conducting substrate (here GaAs). Inverting the metal structure, leads to complementary resonators, which can be described analogous to Babinet's principle [69] and are suitable for coupling experiments [55]. For complementary resonators, the electric and magnetic fields are exchanged and the polarization is shifted by 90° with respect to the corresponding positive resonator. Fig. 2.6c shows the geometry of the complementary resonator of MM II, in the following called MM III. Here, dashed lines indicate the shape of a compact version of MM III, developed by L. Diebel [70] in this group. The compact design (called MM IV) allows for a strongly increased signal, compared to MM III, as almost four times as many resonators fit into an array of the same size. Another advantage of this resonator geometry is the extremely high agreement between experiment and numerical simulations, which is described in greater detail in ref. [70].
To further study these structures, we perform finite-element frequency domain (FEFD) simulations, to numerically calculate the spatial field distribution and spectral response of the THz resonators. For this reason, gold resonators on GaAs substrate, implemented with ϵ_{Au} and ϵ_{GaAs}, are simulated. We obtain transmission spectra (T) through FEFD calculations of the far-field. Here, also the next higher mode of those resonators a dipolar (DP) mode which originates from dipolar currents conducted along the line elements parallel to the incident electric field is visible. For the positive resonators, MM I and MM II, the calculated spectra show an increased absorption manifesting as transmission minima at their resonances. The transmission spectrum of MM I, shown in Fig. 2.6d, exhibits a decline at $\nu_{\mathrm{LC}} = 0.8\,\mathrm{THz}$, corresponding to the LC mode of the material and a second decline located at $\nu_{\mathrm{DP}} = 1.6\,\mathrm{THz}$ for the DP mode. Correspondingly, for MM II

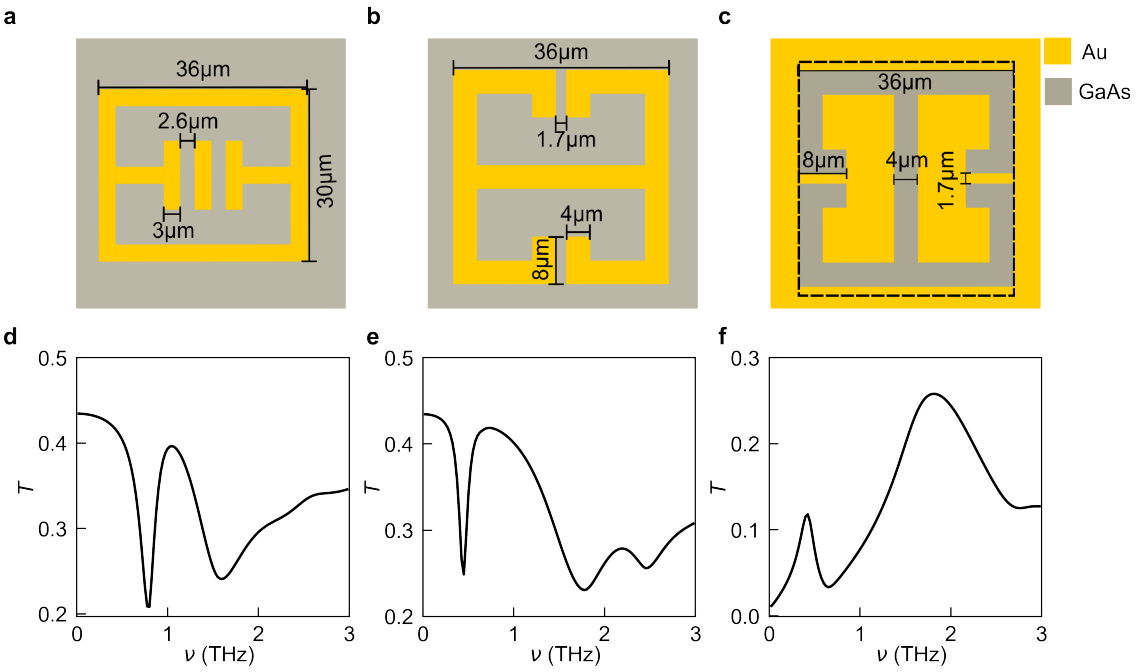

Figure 2.6: Subwavelength THz resonator designs. Geometry of (a) MM I, (b) MM II, (c) MM III and indicated in (c) by dashed lines MM IV. The colour is attributed to the material (yellow = Au, grey = GaAs). (d)-(f) Calculated transmission spectra of (d) MM I, (e) MM II and (f) MM IV.

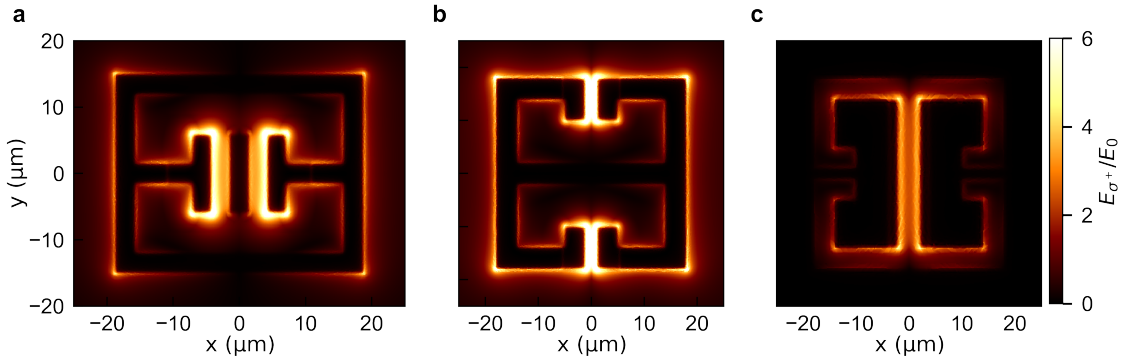

Figure 2.7: Electric field distribution of the LC mode. (a) In-plane field distribution of the LC mode of MM I. The double gap design shows a field enhancement E_{σ^+}/E_0 of up to 8 with respect to the perpendicularly irradiated field in the gap region. The LC modes field distribution of MM II is shown in (b) and of MM III in (c). The strongest field enhancement is again in their individual gap region.

the transmission minima are located at ν_{LC} = 0.5 THz and ν_{DP} = 1.8 THz (Fig. 2.6d). The spectra for complementary metamaterial are inverted: At resonance, there is an increased transmission. The transmission for MM III (Fig. 2.6f) shows a peak at ν_{LC} = 0.5 THz and ν_{DP} = 1.8 THz.

These FEFD calculations of gold resonators on GaAs substrate give also access to the electric near-field distribution of the resonator modes. The right-circularly polarized in-plane field component E_{σ^+}, which couples to the cyclotron transition, is depicted in Fig. 2.7 for the fundamental LC mode of the metamaterials used in this thesis. The field is extracted at z = −200 μm, in the GaAs substrate, where the 2DEGs would be located in the light-matter coupled case. The strongest field enhancement E_{σ^+} with respect to the incident linearly polarized field E_0 is located in the gap region of each metamaterial. The double capacitive gap region of MM I, featuring three bars (Fig. 2.7a), is located in the middle of the resonator, whereas the two gaps of MM II are at the outer perimeter (Fig. 2.7b). The inverse resonator MM III (Fig. 2.7c) is rotated by 90° with respect to its direct resonator geometry. It shows a complementary field distribution compared to its direct counterpart: The gap is now located at the centre of the resonator, concentrating most of the electric field across the 4 μm wide gap.

The field distributions of the second higher order resonances, again extracted 200 μm

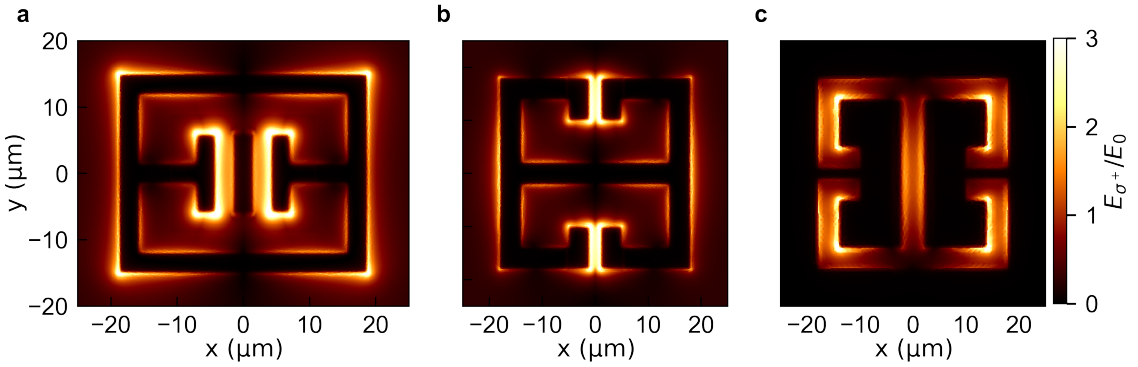

Figure 2.8: Electric field distribution of the DP mode. (a)-(b) In-plane field component E_{σ^+}/E_0 distribution of the DP mode of MM I and MM II respectively. The field is slightly more homogeneously distributed over the whole geometry of the resonator in comparison to the LC mode. (c) The negative MM III exhibits a strong separation of DP mode and LC mode: The field is more strongly concentrated at the outer parts.

beneath the metasurface, is depicted in Fig. 2.8: Generally, the field enhancement of the DP mode is lower compared to the LC mode. For the direct resonators (MM I and MM II), the DP mode is more homogeneously distributed over the whole resonator geometry (Figs. 2.8a and b, respectively), leading to a larger mode volume and therefore potentially weaker coupling. For the complementary structure MM III, the DP mode is largely located at the outer part of the resonator, leading also to a stricter separation of the two modes (Fig. 2.8c).

As discussed above, the spatial shape of the vacuum mode is of importance for the coupling strength of a system. For the complex structures used in our coupling experiments, the mode volume can not be calculated easily. Consequently, numerical calculations have to be taken into account to determine the relevant cavity volume. An estimation is given by the product of the in-plane area of the gap times the out-off-plane extensions of the field, E_z. Revealed by the simulations, the calculated electric field distribution along the z-direction decays on a length scale of a few microns. For the realization of ultimately high coupling, it is thus necessary to place the matter excitation as close to the resonator gaps as possible. However, as Bayer at al. [17] showed: The vacuum mode is not solely defined by the resonator design, but depends on the dielectric function of the matter excitation. It is therefore not possible to optimize the vacuum mode without considering the electronic

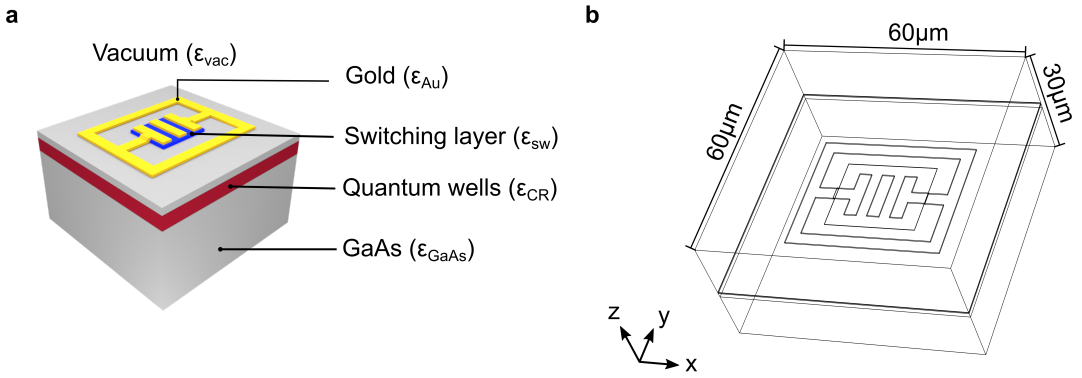

Figure 2.9: Numerical model of a light-matter coupled system. (a) Structure for the numerical simulation corresponding to the coupling between cyclotron resonances of a 2DEG and the light field of an optical micro-cavity in the THz regime. The materials are implemented by their dielectric function: ϵ_{Au} (gold), ϵ_{SW} (blue), ϵ_{CR} (red), ϵ_{GaAs} (grey). (b) Depiction of the simulation volume including indication of the vacuum ϵ_{vac}.

excitation. Instead, there is a need for a unified treatment of matter and light system. The next section describes the numerical analysis of deep- and ultrastrongly coupled system, following this ansatz.

2.4.3 Finite element simulations of light-matter coupling

The challenge to simulate deep-strongly coupled structures is met by solving Maxwell's equations classically. Following ref. [17], we employ a parameter-free theory which describes the interaction between electromagnetic fields of subwavelength THz resonators and the electronic polarization of a matter system. This allows for the prediction of the complex behaviour of systems whose coupling strengths approach $\frac{\Omega_{\mathrm{R}}}{\omega_0} = 1$ and even goes beyond unity. Due to the joint treatment of the light and matter system, taking into account the reshaping of the cavity mode by the matter excitation, the whole system can be optimized regarding its coupling strength. The classical theory implements quantum electrodynamic terms, caused by the anti-resonant terms in the ultrastrong coupling regime through complex dielectric functions $\epsilon_{\mathrm{material}}$ of the materials that are used. These materials are arranged to exactly reproduce the experimental structure. Fig. 2.9a shows schematically the design of such a simulated structure: Placed on top of the GaAs substrate (grey) is

an active layer representing the quantum wells (red). This is followed by another thin GaAs layer (grey), on which the metallic resonator (gold), encapsulated by vacuum, lies. Underneath the gap region of the resonator, a potential switching-patch (blue), which can be activated to switch-off the resonator, is placed. This switching functionality will be discussed in greater detail in Chapter 5.

The exact geometry of the metamaterial was implemented by assuming a dielectric constant of gold $\epsilon_{\mathrm{Au}} = -10^5 + i10^5$ which leads to perfect metallic behaviour. The response of the uncoupled structure can be calculated with the dielectric constants of vacuum ($\epsilon_{\mathrm{vac}} = 1$), the not-activated switching patch ($\epsilon_{\mathrm{sw}} = 13.7$) and GaAs ($\epsilon_{\mathrm{GaAs}} = 12.9$). To achieve light-matter coupling an active layer is introduced. This layer represents the quantum well stack including its doping layers, with a homogenous three-dimensional electron density chosen such that integration along the entire z-extension of this layer results in the combined two-dimensional carrier density of the entire QW stack $\rho_{\mathrm{CR}} = n_{\mathrm{QW}} \times \rho_{\mathrm{2DEG}}$. This layer hosts the cyclotron resonance of electrons with an effective mass m^*, implemented by an anisotropic dielectric tensor ϵ_{CR} resulting from the influence of an external magnetic field, oriented along the z-axis, on a plasma of free carriers [71]:

$$\epsilon_{\mathrm{CR}} = \begin{pmatrix} \epsilon_{\mathrm{xx}} & i\epsilon_{\mathrm{xy}} & 0 \\ -i\epsilon_{\mathrm{xy}} & \epsilon_{\mathrm{xx}} & 0 \\ 0 & 0 & \epsilon_{\mathrm{GaAs}} \end{pmatrix}. \tag{2.27}$$

The components $\epsilon_{\mathrm{xx}}(\omega) = \epsilon_{\mathrm{GaAs}} - \frac{\omega_{\mathrm{P}}^2(\omega+i\kappa)}{\omega\left[(\omega+i\kappa)^2-\omega_{\mathrm{CR}}^2\right]}$ and $\epsilon_{\mathrm{xy}}(\omega) = \frac{\omega_{\mathrm{P}}^2\omega_{\mathrm{CR}}}{\omega\left[(\omega+i\kappa)^2-\omega_{\mathrm{CR}}^2\right]}$, with the plasma frequency $\omega_{\mathrm{p}} = \sqrt{\frac{\rho_{\mathrm{CR}}e^2}{\epsilon_0 m^*_{\mathrm{GaAs}}}}$, describe the two-dimensional chiral polarization response of the Landau-electrons perpendicular to the magnetic field. In z-direction, the response is solely determined by ϵ_{GaAs}. The scattering rate $\kappa = 3 \cdot 10^{11}$ Hz was chosen to reproduce the experimentally determined line width of the cyclotron resonance. The geometry for the calculation via finite element method, which is based on the solutions of Maxwell's equations with periodic boundary conditions, is depicted in Fig. 2.9b indicating the extensions of the simulation volume and the vacuum. Providing the spatial distribution of electric field and current amplitudes, the numerical simulations facilitate the analysis and optimization of deep-strongly coupled structures. Furthermore, they guided the design of switchable resonators, which will be used to realize subcycle electrodynamics.

For a coupled system excited by an in x-direction linearly polarised electromagnetic wave, the spectral response is calculated depending on the cyclotron frequency ν_{CR}. The resulting near-field distribution provides, applying a formula developed by Stratton and Chu [72], the far-field distribution and accordingly, the transmission spectra. Detuning ν_c from $\nu_0 = \nu_{LC}$ in the USC regime, delivers the typical, yet complex anti-crossing transmission spectra, as exemplary shown in Fig. 2.10a. Here, a threefold QW structure, with an electron density of $\rho_{CR} = 3 \times 1.75 \times 10^{12}\text{cm}^{-2}$, is coupled to MM I. The challenges, that arise for high light-matter coupling strengths, are clearly observable: There is a single well-defined lower polariton (LP) resonance, that emerges from CR at low frequencies, yet there are multiple resonances above the CR. Those resonance have a curvature opposite to the LP, corresponding to the expected curvature of the upper polariton (UP). The origin of these modes might be off-resonant coupling to higher order modes of the resonator, inter-resonator coupling stemming from the array character of the metasurface or magneto-plasmon effects. This problem is currently investigated in our group, since these additional resonances inhibit an unambiguous identification of the UP, therefore complicating the determination of the coupling strength. However, numerical calculations make way for two possibilities to identify the polariton branches:

Identification through the mode profiles

As the LC mode has a specific spatial mode profile (Fig. 2.7), the polaritons resulting from the coupling of this mode to the matter excitation have the same spatial distribution of the electric field. In order to identify the polaritons, the spatial distribution of each mode, appearing in the transmission spectra, has to be compared to the fundamental LC mode. This method to identify the polaritons brings some difficulties, as the higher order modes of direct resonators (see Figs. 2.8a and b) strongly resemble the fundamental mode (see Figs. 2.7a and b). It is therefore primarily applicable for complimentary metamaterials, where the LC and DP mode are more strongly separated.

Identification through charge carrier density sweeps

Since the numerical calculations offer the possibility to tune the electron density continuously, a simultaneous tuning of Ω_R is feasible. According to eq. 2.17 the coupling strength depends on the number of matter excitations. Therefore, increasing ρ_{CR} from zero to the experimental electron density ρ_0 leads to the evolution from the

uncoupled to the ultrastrongly coupled system. The transmission spectra $T(\nu, \rho_{CR})$ at the anti-crossing point (vertical dashed line in Fig. 2.10a) trace this evolution (Fig. 2.10b). For increasing electron densities, the uncoupled resonator mode at ν_{LC} for $\rho_{CR} = 0$ splits into the polariton branches. This allows for the identification of the LP and UP which evolve from the uncoupled LC mode. For even higher densities the DP mode anti-crosses with the UP of the LC mode. These experimentally unattainable data, enable the unambiguous identification of the polaritons (marked by dashed white lines in Fig. 2.10a), that arise from coupling to the fundamental resonator mode.

Applying these methods, the UP can be identified and a Hopfield fit then yields the corresponding coupling strength. The exemplary case, shown in Fig. 2.10a, is then characterized by a coupling strength of $\frac{\Omega_R}{\omega_0} = 0.55$.
In conclusion, the extremely strong coupling of Landau-quantized electrons and THz metamaterials, optimized by an unified treatment of light and matter, can be numerically simulated without any fitting parameters.

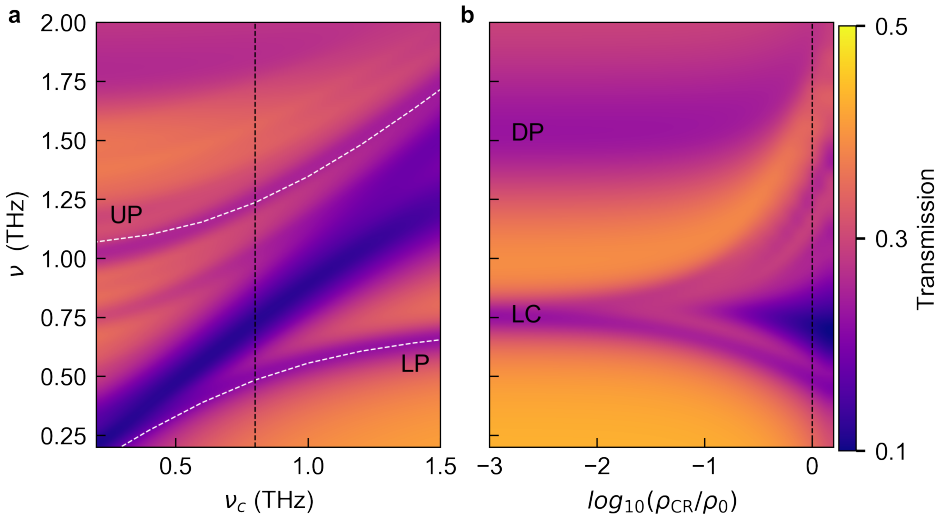

Figure 2.10: FEFD calculations of the transmission spectra of an ultra-strongly coupled structure. (a) Transmission spectra as a function of the cyclotron resonance frequency ν_c. Above the bare CR, that stems from uncoupled parts of the structure, there are multiple polariton branches. At the anti-crossing point (vertical dashed line) the charge carrier density (ρ_{CR}) sweep (b) enables the identification of the polaritons of the LC mode, as they evolve from the bare resonator frequency, ν_{LC}. Correspondingly, the dashed white lines in (a) mark the lower (LP) and upper (UP) polariton branches with a splitting corresponding to a coupling strength of $\frac{\Omega_R}{\omega_0} = 0.55$.

3 Methods

To fully understand the interaction between light and matter in a strongly coupled system, one needs to control both the matter part, the heterostructure, and the light mode. Starting with molecular beam epitaxy (MBE) growth of the heterostructures, which consist of 2DEGs hosting free electrons, we are able to custom tailor heterostructures of different material systems. The MBE grown structures are pre-characterized by transport measurements, where one is given access to the electrical properties including the 2DEGEs charge carrier density and its mobility. The electrically characterised matter system then needs to be coupled to the light mode of subwavelength THz resonators. This is done by deposition of the metallic resonators on top of the heterostructures. Finally, the prepared sample is thoroughly studied in a THz time domain magneto-spectroscopy setup setup. In the following chapter, the methods which are necessary to fabricate and study our light-matter coupled structures are described.

3.1 MBE growth

The matter system, III-V heterostructures, hosting high quality 2DEGs, is grown by molecular beam epitaxy in an ultra high vacuum of less than 10^{-11} bar. This method enables the fabrication of atomically precise monocrystalline structures of various semiconductor materials [73]. All samples presented in this work were grown in a MBE system, using high purity source materials indium (In), aluminium (Al), gallium (Ga), arsenide (As) and antimony (Sb). For the fabrication of n-doped systems, silicon (Si) is used as doping material. The materials are deposited on GaAs substrate wafers, which are heated to temperatures ranging from 360°C to 620°C, depending on material system. By constant rotation of the substrate, homogenous growth over the whole sample surface is provided through uni-formal material deposition. The growth rate is determined by the As or Sb

flux respectively. The growth rate can be measured with a high energy electron diffraction (RHEED) gun, where beam of accelerated electrons is reflected at the sample surface. This gives access to its roughness, which oscillates during growth, as the crystal is built up layer-wise. An analysis of the diffraction patterns also allows for the estimation of the crystal quality, varying from mono- to poly-crystalline growth.
For the AlGaAs/GaAs heterostructures [74] growth rates of $r_{\mathrm{Ga}} = 2.7$ and $r_{\mathrm{Al}} = 1.3$ with constant As supply were chosen. This leads to $Al_{0.33}Ga_{0.67}As$, which is lattice matched with GaAs and can therefore be epitaxially stacked on GaAs. Furthermore, for light-matter coupling experiments, indium bases structures, which are lattice mismatched on GaAs substrate, were grown. Consequently, a sophisticated buffer system to enable defect-free growth and the formation of high quality 2DEGs is required. The growth rates for the InAlAs/InGaAs/InAs heterostructures [75] were $r_{\mathrm{Ga}} = 0.6$, $r_{\mathrm{Al}} = 0.6$ and $r_{\mathrm{Al}} = 2.65$, leading to an indium ratio of 81.5%.

3.2 Electrical characterization

To analyse the electric characteristics of MBE grown samples, their magneto-transport behaviour is studied. To this end, they are mounted in chip carriers, electrically contacting the quantum wells. Measurements in the van der Pauw (VdP) geometry [76] are conducted to determine the charge carrier density and mobility of the 2DEGs. This method requires four contacts (A,B,C,D; schematically depicted Fig. 3.1) to apply a current I and measure the voltage parallel or perpendicular to the current individually. The longitudinal or transversal voltage U_{xx} and U_{xy} with respect to the applied current I are recorded with and without a perpendicularly applied magnetic field B. This small, typically $B = 0.5\,\mathrm{T}$, magnetic field should not induce quantization, but lead to transport described by the Drude model [77, 78]. The transversal resistivity is then characterized by the Hall effect, whereas the longitudinal resistivity is only determined by scattering events of the electrons, which can therefore be described as classical particles in an external electrical field $\mathbf{E}$. The electrical field leads to a movement of the electrons in its direction with the so-called drift velocity v_{D}. This movement is perturbed after an average scattering time τ_{scatter}, as the electrons collide inside the crystal. Consequently, the current density depends on the applied field $\mathbf{E}$

and the conductivity

$$\sigma = |e|\rho_{\mathrm{2DEG}}\mu_{\mathrm{e}}, \tag{3.1}$$

with the elementary charge e, the mobility $\mu_{\mathrm{e}} = \frac{e\tau_{\mathrm{scatter}}}{m^*}$ and the electron density ρ_{2DEG}. For an additional magnetic field, σ becomes a tensor, leading to the resistivity tensor $\rho = \sigma^{-1}$. The VdP method allows for the determination of the resistivity by measuring the resistance $R_{nm,jk} = \frac{U_{nm}}{I_{jk}}$, with $n, m, j, k \in$ (A,B,C,D), of permutatively switched contacts of the 4-point measurement configuration. By applying this, the sheet resistivity for zero magnetic field can be expressed as:

$$\rho_{xx}(B = 0) = \frac{\pi}{\ln(2)} \frac{R_{\mathrm{AB,CD}}(0) + R_{\mathrm{BC,DA}}(0)}{2} f\left(\frac{R_{\mathrm{AB,CD}}(0)}{R_{\mathrm{BC,DA}}(0)}\right) \tag{3.2}$$

with the geometry factor f, a function of the ratio $\frac{R_{\mathrm{AB,CD}}(0)}{R_{\mathrm{BC,DA}}(0)}$, owing to the imprecise contact relations. Correspondingly, the Hall resistivity in the regime of non-quantizing magnetic fields reads:

$$\rho_{xy}(B) = \frac{R_{\mathrm{AC,BD}}(B) - R_{\mathrm{AC,BD}}(0) + R_{\mathrm{BD,AC}}(B) - R_{\mathrm{BD,AC}}(0)}{2}. \tag{3.3}$$

The transport properties

$$\rho_{\mathrm{2DEG}} = \left(e\frac{\partial \rho_{xy}}{\partial B}\Big|_{B=0}\right)^{-1} \tag{3.4}$$

and

$$\mu_{\mathrm{e}} = (e\rho_{\mathrm{2DEG}}\rho_{xx}(B = 0))^{-1} \tag{3.5}$$

then follow. For a multiple quantum well stack, the factor n_{QW} which is the number of parallelly connected QWs needs to be considered in the determination of the carrier density. Leaving the regime of non-quantizing magnetic fields described by the Drude model, quantum mechanical effects have to be considered in the transport measurements. This is in detail outlined in ref. [78]. For an external magnetic field of $\frac{eB}{m}\tau = \omega_{\mathrm{c}}\tau > 1$, the B-field quantizes the cyclotron motion leading to the formation of equidistant Landau levels whose energy linearly depends on B (see Chapter 2.4.1). In transport, the Landau-quantization manifests in an oscillatory behaviour of the resistivity tensor elements ρ_{xx} and ρ_{xy}. The longitudinal resistivity ρ_{xx} forms so called Shubnikov de Haas (SdH) oscillations as a

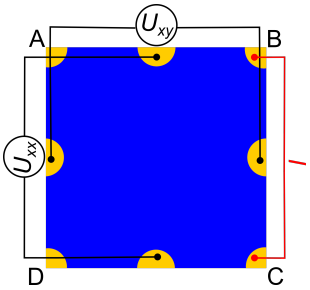

Figure 3.1: Magneto-transport measurement sample geometry. The van der Pauw method, using the contacts A,B,C and D enables the determination of transport properties of a sample. Simultaneously measuring U_{xx} and U_{xy} for an current I in a perpendicular magnetic field B, reveals 2D-properties of the studied system.

function of B. They have a periodicity of $1/B$, with minimal values attributed to localized states at the Fermi energy, occurring at $B = 2\frac{i+1/2}{eh\rho_{2\mathrm{DEG}}}$, with integer i. The SdH oscillations can be used to determine the sheet carrier density of the 2DEG. ρ_{xy} on the other hand, forms so called Hall plateaus, originating in the integer quantum Hall effect (QHE). The plateaus appear at $\rho_{xy} = \frac{h}{e^2\nu}$, with the filling factor ν. They coincide with plateaus of zero resistivity of ρ_{xx} for high magnetic fields. An eight-point measurement allows to simultaneously measure U_{xx} and U_{xy} for a current I as a function of an external magnetic field, applied perpendicular to the sample surface. Fig. 3.1 shows a possible configuration for the measurement. An analysis of the resulting ρ_{xx} and ρ_{xy} gives access to both mobility and density of the electrons in the 2DEG. The described measurements are performed in a helium dewar, cooling the samples to liquid helium temperature (4 K). This corresponds to the temperature given in our optical coupling experiments.

3.3 Sample preparation

After characterizing the transport properties, the 2DEGs can be coupled to the light mode of THz resonators. Our light-matter coupled structures employ metallic subwavelength THz resonator arrays, called metamaterials (see Chapter 2.4.2). They need to be placed in the vicinity of the 2DEGs to enable the dressing of electrons with their light mode. Therefore, they are deposited on top of our heterostructure, following the procedure

described hereinafter. 5×5 mm pieces of the MBE grown wafers, containing high quality 2DEGs, are prepared by removing residual Ga, which is used to mount the wafers in the MBE system. Then a positive electron beam resist (CSAR) is applied on the sample's surface. The desired metamaterial geometry is structured via electron beam lithography (EBL) with an area dose of $60\,\mu\mathrm{Ccm}^{-2}$ in 2×2 mm arrays. Afterwards the resist is developed for 80 s in AR600 546. Subsequently, 10 nm titan (Ti) and 100 nm gold (Au) are deposited onto the sample. The Ti serves as bonding agent for the Au. The remaining resist and surplus Au are removed with Remover PG, leaving only the (2×2 mm) metasurface. To fabricate subcycle switchable resonators presented in Chapter 5, a switching layer is grown on top of the semiconductor heterostructure. This layer is etched with citric acid to patches sized a few micrometers. In an additional EBL step, these patches are aligned with the metallic resonators which are deposited subsequently. For those samples, the GaAs substrate is removed by manually polishing it. The substrate of selective samples is also etched with citric acid, to completely remove the GaAs substrate. For more details on this preparation scheme see Chapter 5.2.

3.4 Femtosecond setup

Optical characterization and examination of deep-strongly light-matter coupled samples is achieved by THz time domain magneto-spectroscopy. The experimental setup including cutting edge scientific equipment, was provided by the AG Huber. Using this spectroscopy setup, one is given access to the polarization response depending on an external magnetic field. Furthermore, to gain insight in the non-adiabatic dynamics of the system on a subcycle timescale, near-infrared (NIR) switching pulses are used to modify the system. Through the sample transmitted THz waveforms are detected in amplitude and phase by electro-optic sampling (EOS), directly in the time domain. A titanium-sapphire (Ti:Sa) amplifier laser provides femtosecond near-infrared pulses, with a pulse duration of 33 fs, centred around 807 nm. The pulses are used for the employed NIR-pump THz-probe spectroscopy by driving an optical parametric amplifier (OPA) which supplies the switching pulses and by generating phase locked THz-probe pulses which are detected in phase and amplitude by EOS [79, 80].

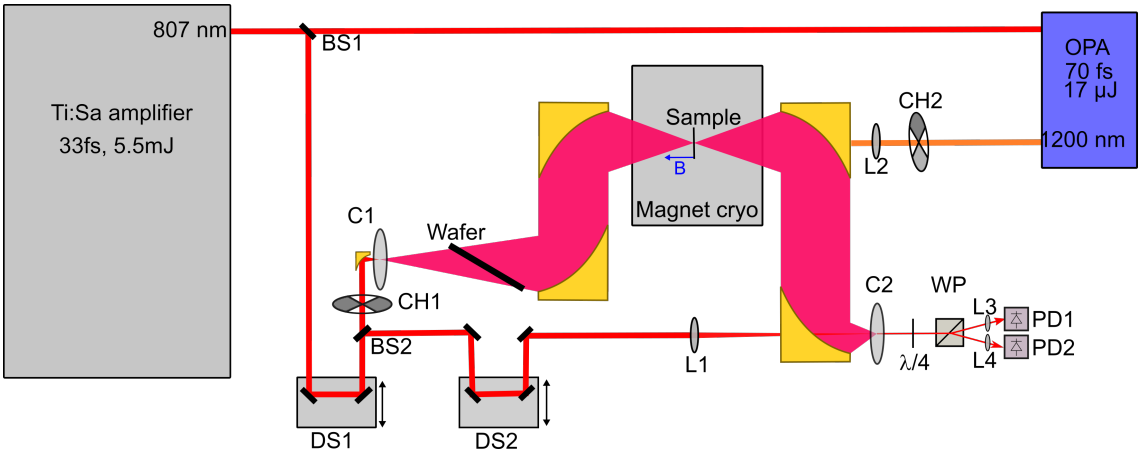

Figure 3.2: THz time domain magneto-spectroscopy setup. The near-infrared (NIR) pulse (centre wavelength, 807 nm; pulse energy, 5.5 mJ; pulse duration, 33 fs) generated in a titanium-sapphire amplifier (repetition rate, 3 kHz) is split by a beam splitter (BS1). The first branch drives an optical parametric amplifier (OPA), which generates the NIR switching pulses, and the second branch is used for THz generation and detection. For the second branch, the delay stage (DS1) controls the delay time t_D of THz and gate pulse for the electro-optic sampling. A second beam splitter (BS2) separates the gate pulse which is delayed by a second stage (DS2) for the electro-optic sampling delay t. The gate is focused through the detection crystal (C2) by a lens (L1), after which its polarization state is analysed by corresponding optics (quarter wave plate, $\lambda/4$; Wollaston prism, WP; focussing lenses, L3 and L4; photodiodes, PD). The NIR power transmitted through BS2 is focused onto the THz generation crystal (C1) by an off-axis parabolic mirror. Only the generated THz is transmitted through the Si-wafer. Off-axis parabolic mirrors recollimate and focus the pulses through the sample, which is located in the magnet cryostat at a temperature of 4 K. A magnetic bias (B) of up to 5.5 T can be applied perpendicular to the sample surface. The transmitted THz waveform is recollimated and focused onto the detector crystal (C2), collinearly with the gate pulse. The NIR signal output from the OPA (centre wavelength, 1200 nm; pulse energy, 17 µJ, pulse duration, 70 fs) is focused by a lens (L2) on the sample, allowing to switch the sample. Mechanical choppers (CH) are placed in the beam paths of THz generation and switching pulses to enable differential detection.

THz time domain magneto-spectroscopy setup

In the following section, the THz time domain setup used to study our samples is described (Fig. 3.2). The femtosecond near-infrared pulses from a titanium-sapphire laser amplifier are split by a beam splitter into two branches. One drives an optical parametric amplifier (OPA) and the other is used for THz generation and detection, respectively. The THz generation beam is sent across a delay line (DS1) introducing the delay time t_D, and is subsequently focused into a $\langle 110 \rangle$-cut zinc telluride (ZnTe) crystal (C1) with a thickness of 1 mm to generate single-cycle THz pulses by optical rectification. The near-infrared (NIR) pump light is separated form the generated THz pulses by a Si-wafer which is transparent for the THz radiation. After collimation by parabolic mirrors, the THz pulses are focused through the sample before the transmitted waveforms are recollimated and focused onto a ZnTe or GaP detector crystal (C2). BS2 splits off a fraction of the NIR power, the gate pulse used for electro-optic sampling. This is sent across a second delay line (DS2) introducing the delay time t. The gate pulse is used for electro-optic detection of the THz pulses in the detector crystal (C2) using polarization optics and a balanced pair of photodiodes. This allows for the reconstruction of the THz pulse. The OPA generates NIR switching pulses with a duration of 70 fs (FWHM) and a wavelength of 1200 nm. They are focused onto the sample with a spot diameter of 4 mm (FWHM) for homogeneous excitation. Two mechanical choppers (CH1 and CH2) modulate the THz and switching pulses at 1/4 and 1/2 of the repetition rate of the laser system, allowing for differential detection of the pump-induced change of the transmitted THz electric field, $\Delta E(t, t_D)$. The linear conversion between $\Delta E(t, t_D)$ and $\Delta E(t, \tau = t - t_D)$, which will be discussed later on, is performed numerically. The sample's temperature of about 4 K is realized in a magneto-cryostat which allows the application of magnetic fields of up to 5.5 T.

Generation of phase locked THz pulses by optical rectification

For the generation of broadband THz pulses, which are required for time-resolved spectroscopic applications, we use nonlinear crystals. In the next section, optical rectification, a nonlinear optical technique for the generation of THz pulses, is described following ref. [81]. The polarization P response in a high electric field E, where nonlinear interaction

becomes relevant can be expressed via a Taylor series [82]:

$$P(E) = \epsilon_0(\chi^{(1)}E + \chi^{(2)}E \cdot E + \chi^{(3)}E \cdot E \cdot E + ...), \tag{3.6}$$

where ϵ_0 is the permittivity of vacuum and $\chi^{(i)}$ describes the i-th-order susceptibility of the medium. The susceptibility tensor is determined by the crystal properties. The higher order terms in P enable processes that allow the generation of polarization components oscillating at different frequencies, such as second harmonic generation, sum- or difference-frequency generation (DFG) [79]. They are caused by a non-vanishing second-order nonlinear susceptibility $\chi^{(2)}$, which occurs only for non-centrosymmetric crystals. If a near-infrared pulse of a duration of 30 fs is radiated onto the nonlinear crystal, there is a broad variety of frequencies ω_k within the broad spectrum of the NIR pulse that can interact with each other, resulting in a broad sequence of possible difference frequencies in the THz regime $\omega_1 - \omega_2 = \omega_{\mathrm{THz}}$. Whereby the bandwidth of the irradiated NIR pulse determines the possible difference frequencies. DFG within a broadband NIR laser pulse is often referred to as optical rectification [83]. THz pulses, generated by optical rectification, are phase-stable, as the mixing components originate in the same NIR-pulse, cancelling out fluctuations of the carrier-envelope phase [84].
Besides the conservation of energy, also the wave vector $k = \frac{n\omega}{c}$, with the medium's refractive index n and the speed of light c, needs to be conserved: $k_{\mathrm{THz}} = k_1 - k_2$. This gives rise to the so called phase matching condition: For efficient generation of THz pulses through optical rectification, the group velocity of the NIR pulse and the phase velocity of the THz radiation have to be equivalent. Only then, the generated THz waves are in phase with the nonlinear polarization throughout the whole crystal, allowing for constructive interference between them and thus, efficient THz-generation.
This is not fulfilled for any arbitrary crystal, as the refractive index is frequency dependent. However in this work, ZnTe nonlinear crystals were used for THz generation, as the phase matching condition, meaning group velocity of the pump pulse and phase velocity of the THz radiation are equal, is fulfilled for pump wavelengths around 800 nm and THz frequencies around 1 THz [85]. This essential property of ZnTe crystals is combined with a high linear electro-optic coefficient, which is related to susceptibility tensor elements describing optical rectification [86], resulting in efficient nonlinear optical THz generation. Yet, the THz generation is limited by the coherence length of the process. For this reason,

ZnTe crystals of a thickness of 0.5 mm were used for THz generation.

Electro-optic sampling

Electro-optic sampling [87] is a convenient way to record the amplitude and phase of phase stable pulses very sensitively, even in the THz regime. This detection procedure is based on the electro-optical effect, also known as the Pockels-effect [88], of the transient THz field which induces a change of the refractive index of the crystal. For the detection of THz transients, ultra-short NIR gate pulses co-propagate with the THz pulses through a thin electro-optical crystal. The femtosecond gate pulses are delayed by t, with respect to the THz pulse. As the duration of the NIR pulse is very small compared to the THz field, the gate pulse experiences only a quasi-static electric field of the THz field in the crystal. Depending on the crystal orientation, the electric field of the THz pulse induces birefringence in the crystal, resulting in different refractive indices for ordinary (o) and extra ordinary (eo) axis. The difference Δn for ordinary and extra ordinary polarization is proportional to the electric field of the THz pulse E_{THz}. Caused by this birefringence, the NIR experiences a phase retardation and the polarization of the transmitted NIR pulse is rotated by $\Delta\phi$. Since the duration of the NIR pulse is short compared to the oscillation period of the THz field, $\Delta\phi$ is proportional to the instantaneous electric field. Therefore, measuring $\Delta\phi$ allows for the precise determination of the electric field of a THz pulse, depending on the delay time t between THz and gate pulse. Varying the delay time t allows for the stroboscopic reconstruction of the full THz waveform. The ellipticity of the NIR gate pulse can be recorded using polarization optics in the following way: Without THz field present, a linearly polarized NIR gate pulse passing the crystal does not change its polarization. The linearly polarized pulse then passes a $\lambda/4$ plate oriented at 45°, where it becomes circularly polarized. A Wollaston prism then splits the pulse into spatially separated beam lines with orthogonal polarization. Two identical photodiodes detect the intensity of the two beams by measuring the currents through the diodes I_{PD1} and I_{PD2}. As the NIR pulse is perfectly circularly polarized, the difference signal of the two resulting beams cancel out, $\Delta I = I_{\mathrm{PD1}} - I_{\mathrm{PD2}} = 0$. However, if a THz field is present, the nonlinear crystal becomes birefringent so the NIR pulse experiences a phase modulation and polarization rotation by $\Delta\phi$, which is approximately proportional to the instantaneous

THz amplitude [89, 90]. Passing the $\lambda/4$ plate, the pulse becomes elliptically polarized, leading to a different intensities of the split beams after passing the Wollaston prism. The phase modulation of the probe pulse has therefore become an intensity modulation of the two orthogonal polarizations. The difference signal of the photo diodes ΔI then becomes finite, proportional to E_{THz}. Therefore the electric field distribution of the THz pulse as a function of the delay time t can be sampled.
To detect, the optical probe and THz beam are polarized parallelly to the <110> direction of a ZnTe crystal of 1 mm thickness or a GaP (gallium phosphide) crystal of 200 μm thickness. Owing to the phase matching of the different crystals, the ZnTe crystal allows for the observation of frequencies of up to 2.8 THz, whereas the used GaP crystal detects frequencies of up to 7.5 THz [86].

NIR-switching pulse

To induce free carriers in the switching layer in the samples, a short NIR pulse is used. The switching pulse's photon energy needs to excite electrons from the valence band to the conduction band of the semiconductor layer, but not of the GaAs substrate and buffer layer (band gap 815 nm). Since the pulses from the Ti:Sa amplifier energy (807 nm) does not fit this criterium, NIR pulses from an optical parametric amplifier (OPA) fed by pulses from the Ti:Sa laser are used. Optical parametric amplification is based on DFG between a strong pump pulse and a weak seed-pulse. The OPA used here features two amplification stages. The incoming pulse from the Ti:Sa amplifier is split into three branches, one generating a broad supercontinuum and the remaining two used as pump pulses. The supercontinuum serves as seed pulse and is temporally stretched. Temporal overlap with the first pump pulse determines the wavelength for amplification. After this first amplification stage, the signal pulses are spatially overlapped with the second pump pulse. This method facilitates pulses, with tunable center-wavelengths between 1100 and 1600 nm, and an energy of up to 0.5 mJ [79].
To pump the switching layer, the pulses are tuned to 1200 nm, enabling photo doping of only the switching layer. Frequency-resolved optical gating (FROG) measurements were conducted to characterize the pulse [91]. This measurement revealed the temporal shape of the switching pulse (Fig. 3.3). We determine a full width half maximum (FWHM) of 70 fs,

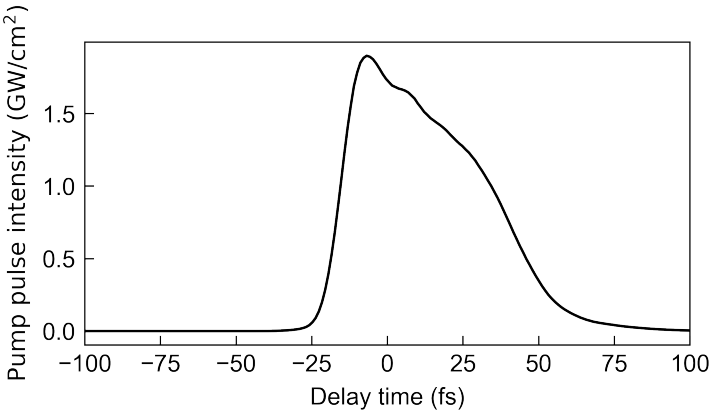

Figure 3.3: Characterization of the switching pulse. FROG measurement yields a FWHM of 70 fs

providing the possibility to switch-off light-matter coupling on non-adiabatic time scales.

NIR-pump THz-probe spectroscopy

In order to determine the subcycle dynamics of light-matter coupling the dynamical THz response is measured. To this end, the THz and the switching pulse are shifted with respect to each other by a delay time t_D. This delay, introduced by DS1 (Fig. 3.2), is the time interval between the switching pulse and the THz field crest, as shown in Fig. 3.4. If the switching pulse arrives before the probe pulse ($t_D > 0$ ps), the sample is pumped, yielding the quasi-steady state spectrum of the switched state. For delay times far after the probe, one gets the spectrum of the unswitched sample. Between these two extremal states, when the sample is either fully switched or unswitched, the THz probe pulse, oscillating at the system's resonance frequencies, is perturbed in various phases. However the interpretation of the dynamics of an optical resonance whose properties vary on a subcycle scale is challenging, as the duration of the probing THz pulse is on much longer timescales than the switching time itself. The response function therefore changes faster than one cycle duration of the light. To get the spectrally resolved response a numerical transformation from the t_D to the τ-frame has to be performed. The transmission data are transformed into a different time frame in which $\tau = t + t_D$ represents a constant delay between the switching and the electro-optic detection pulses. Following this formalism of

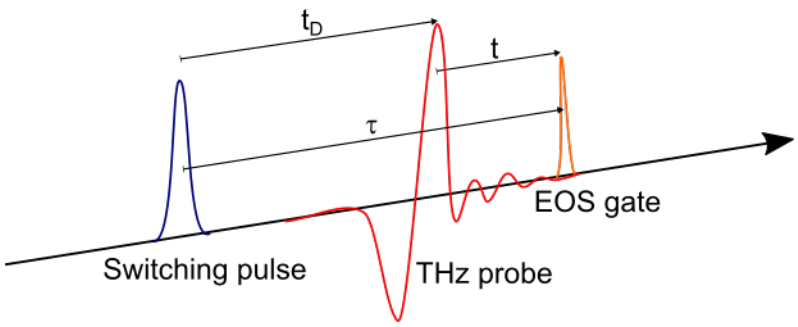

Figure 3.4: Time delay schema. The THz probe pulse (red), transmitted through the sample, is probed by the EOS gate pulse (orange) with the time delay t. The delay time t_D is the constant delay between the switching pulse (blue) and the THz probe. $\tau = t - t_D$ is the delay between switching pulse and EOS gate.

Kindt and Schuttenmaer [92], allows for the extraction of a linear response function for our structures during switching. Fourier transform of the obtained data ($E(t, \tau)$) along t yield the transmission spectra $T(\nu, \tau)$ which then trace the evolution from the initial to the fully switched state depending on the delay time τ.

4 Experimental realisation of deep-strong light-matter coupling

High coupling strengths in light-matter coupled structures are crucial for fundamental studies of cavity quantum electrodynamics and for the observation of experimentally unexplored quantum phenomena, such as the release of the vacuum photon population. In optical systems, employing THz resonators to dress Landau-quantized electrons [13, 55], coupling strengths of up to $\frac{\Omega_R}{\omega_0} = 1.43$ [17] have been reported, yet it is still desired to further increase the coupling strength. Simultaneously tailoring the vacuum mode of the structure through the resonator as well as through the electronic excitation is the key ingredient to achieve ultimately high coupling. We follow up on the work of Bayer of our group [93] and continue to exploit the potential of AlGaAs/GaAs heterostructures for deep-strong coupling. In this chapter, we study the effects of a strongly increased number of quantum wells. Furthermore, we go beyond this material system and explore InAs-based heterostructures, which promise drastically reduced effective electron masses. The high quality 2DEGs, formed in these material systems, are optimized for ultimately strong coupling to subwavelength THz resonators.

4.1 Light-matter coupling of cyclotron resonances in GaAs quantum wells

Our study on extremely strong light-matter coupling starts with AlGaAs/GaAs quantum wells, a model system for ultrastrong [13, 18, 19, 55, 61] and deep-strong coupling [17, 26].

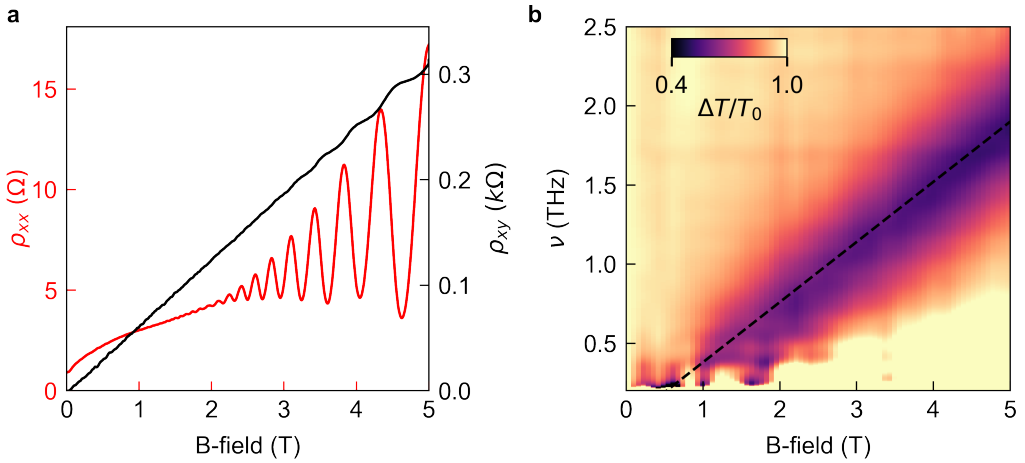

Figure 4.1: Characterization of a sixfold GaAs-QW stack. (a) The magneto-transport measurement of the longitudinal (ρ_{xx}, red curve) and the Hall resistance (ρ_{xy}, black curve) show characteristic SdH oscillations and Hall-plateaus, indicating very similar 2D systems with a combined sheet carrier density of $6 \times 1.75 \times 10^{12}\,\mathrm{cm}^{-2}$ and an electron mobility of $\mu_\mathrm{e} = 3.2 \times 10^5\,\mathrm{cm}^2/\mathrm{Vs}$. (b) THz transmission measurements with perpendicularly applied magnetic field B are normalized to the transmission spectrum at $B = 0\,\mathrm{T}$. The slope of the CR corresponds to an effective electron mass of $m^* = 0.073\,m_\mathrm{e}$.

As the number of matter excitation is an essential tuning knob to maximize the coupling strength between Landau-quantized electrons and subwavelength THz resonators, high quality 2DEGs are desired. The following chapter presents AlGaAs/GaAs heterostructures, optimized for light-matter interactions, as well as their coupling to various metamaterial geometries.

4.1.1 Characterization of the 2DEGs

We present MBE grown $Al_{0.33}Ga_{0.67}As$/GaAs heterostructures. This material composition with a band off-set of $E_\mathrm{barrier} = 0.31\,\mathrm{eV}$ enables the formation of electronic barriers and consequently the formation of quantum wells which host high quality 2DEGs. In our structures the electrons are provided by n-doping using Si in the AlGaAs barriers. If an external magnetic field is applied, the free electrons of the 2DEGs are Landau-quantized, building an effective two-level system, which enables the coupling to the THz resonator's light modes, as discussed in Chapter 2.4.

The criteria, imposed on the two-dimensional system to reach high strengths of light-matter coupling, is an extremely high electron density, while sufficient electron mobility is provided. To get high quality AlGaAs/GaAs 2DEGs meeting these requirements, an optimization, working out parameters to enable light-matter coupling of extremely dense Landau-quantized electrons, was developed by A. Bayer [93]. He found that the light and the matter part of a coupled system should not be considered separately, but need to be treated in an unified way. The mutual influence of light and matter becomes clear, as the dipole moment of the cyclotron transition shapes the vacuum mode. The light mode is squeezed out of the QW region, which was unveiled by numerical calculations [17] that take the dielectric function of the 2DEGs into account. This mechanism is proof of the predicted light-matter decoupling [20] occurring for extremely high coupling strengths. Furthermore, a sheet carrier density limit for the studied QWs was identified, as the mobility was found to be strongly reduced for high electron densities, contradicting the Coulomb shielding effect [94], which would lead to increased mobilities. Taking into account these effects, Bayer developed a heterostructure design, that allowed for the realization of deep-strong coupling in Landau-quantized systems. This design comprises tightly stacked, narrow rectangular QWs placed near the sample surface.
The calculations showed a strong decrease of the light mode over the QW stack with distance to the resonator gap region. Therefore, stacking a high number of QW has been considered unattractive. Yet in this work, we want to explore the limits of increasing the number of QWs in the stack and test its influence on the light-matter coupling strength. To this end, we grow AlGaAs/GaAs QWs stacks with a strongly increased number of QWs. Moreover, we test different resonator designs and employ a compact resonator design [70] to enable unprecedentedly high coupling strengths. All of our samples consist of a variable number of 10 nm thick GaAs QWs separated by 30 nm thick AlGaAs barriers. The δ-doping layers are located in the middle of the AlGaAs barriers ensuring an equal distance to each QW and therefore a symmetric band bending.

Electrical characterization of the 2DEG

To evaluate the electron transport properties and get access to both the electron mobility μ_e and density ρ_{2DEG}, magneto-transport measurements were conducted (see Chapter 3.2).

In Fig. 4.1a the magneto-transport measurement of a sixfold heterostructure (*GaAs1*) is exemplary shown. ρ_{xy} the transversal resistivity (black curve) transitions from the Hall effect to the quantum Hall effect, which is apparent in the step like shape for higher magnetic fields. This shape is caused by the Landau level degeneracy. The longitudinal resistivity ρ_{xx} (red curve) on the other hand shows distinct oscillations, the so called Shubnikov de Haas (SdH) oscillations, which originate in the magnetic field dependence of the DOS of a Landau system. The clear QHE and SdH oscillations prove that we indeed have a well-defined two-dimensional system. Assuming that all QWs have very similar densities and mobilities, which is indicated by the clear plateaus and SdH oscillations without beating, we determine $\mu_e = 3.2 \times 10^5\,\mathrm{cm}^2/\mathrm{Vs}$, fulfilling eq. 2.26, and a total sheet carrier density of $\rho_{2\mathrm{DEG,total}} = 6 \times 1.75 \times 10^{12}\,\mathrm{cm}^{-2}$ by following eq. 3.5 and eq. 3.4. However, there are also signs of parallel conduction apparent [95]: the parabolic background of ρ_{xx} and the flattened steps of ρ_{xy}. These features indicate a conduction channel with significantly lower mobility compared to the 2DEGs. Not fully ionized doping layers, caused by the high doping density in this structure, can form such a conduction path. To further characterize this sample, its optical response is studied in the magneto-spectroscopy setup.

Optical characterization of the 2DEG

For the optical characterization, linearly polarized THz pulses weakly excite the 2DEGs which are located in a variable, perpendicular magnetic field B. For $B > 0$, the 2DEG condenses to the degenerate ground state. The weak THz pulses induce a polarization between the highest occupied LL and the first excited LL in the 2DEG. This polarization radiates into the far field via long lived coherent oscillations at the cyclotron frequency $\nu_c = \frac{eB}{m^*}$. The reemitted polarization is shifted by 90° with respect to the incident field, therefore cancelling out the THz field at this frequency. Consequently, the CR is visible as an increased absorption in the spectrum of the transmitted field, detected with the EOS method (see Chapter 3). Systematically varying B allows for the determination of the effective mass m^* by linearly fitting the resulting cyclotron frequency. Fig. 4.1 b shows the normalized transmission spectra of the sixfold QW structure. The linear B dependence

of

$$\nu_c = \frac{eB}{m^*} \tag{4.1}$$

provides an electron cyclotron mass of $m^* = 0.073\, m_e$, where $m_e = 9.1 \times 10^{-31}$ kg is the electron mass. m^* is in accordance with the expected value for the effective mass of GaAs QWs of a thickness of 10 nm [96]. The decay time τ_{CR} of the CR is given by $\Delta B = \frac{m^* \Delta \nu_c}{e} = \frac{m^*}{e\tau_{CR}}$. We obtain from Fig. 4.1b a decay time of $\tau_{CR,exp} = 0.5$ ps, which is far less than we would expect from the DC transport measurements, which reveal a scattering time $\tau_{DC} = \frac{m^* \mu_e}{e} = 13.4$ ps. The strongly increased decay rate $\Gamma_{CR} = \tau_{CR}^{-1}$ is attributed to superradiant (SR) damping [97] of the CR. The polarization, generated by the coherent incident THz field, decays in a superradiant (SR) manner. Since this collective decay mechanism depends roughly linearly on the number of oscillating dipoles ρ_{2DEG}, it is much faster than the non-radiant dephasing of a single oscillator. To strengthen this assumption, we consider a quantum mechanical model, developed by Zhang et al. [98]. This model for THz excitation and coherent CR emission of a 2DEG in a perpendicular magnetic field, allows to quantify the CR decay rate as the sum of SR decay, linearly dependent on ρ_{2DEG}, and other phase-breaking scattering mechanisms: $\Gamma_{CR} = \Gamma_{SR} + \Gamma_{scattering}$. With $\Gamma_{SR} = \frac{e^2 \rho_{2DEG}}{\epsilon_0 m^* (1+n_{GaAs})c}$, the vacuum permittivity ϵ_0, the refractive index of GaAs n_{GaAs} and the speed of light c, they provide a formula for the estimation of the CR decay. Considering, that $\Gamma_{scattering} \approx \Gamma_{DC}$ one gets the following expression for the CR decay time

$$\tau_{CR} = \frac{m^*}{e}\left[\frac{e n_{QW} \rho_{2DEG}}{\epsilon_0 (1 + n_{InAs}) c} + \frac{1}{\mu_e}\right]. \tag{4.2}$$

Calculating τ_{CR} in this manner results in a decay time of $\tau_{CR} = 0.35$ ps, which is in good agreement with the experimentally obtained value of 0.5 ps. We therefore confirm, that superradiance dramatically speeds up the radiative decay in our highly doped structures. Having the 2DEG stack fully characterized, we next couple its electrons to the fundamental light mode of subwavelength THz resonators, which are expected to suppress superradiance [55].

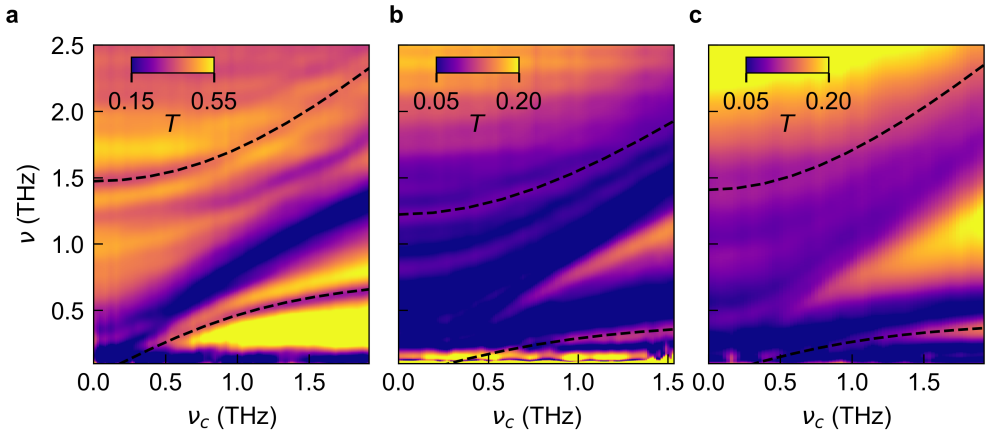

Figure 4.2: Light-matter coupling of sixfold GaAs QW stacks. Transmission spectra as a function of ν_c for a sixfold QW with an electron density of $\rho_{\mathrm{2DEG,total}} = 6 \times 1.75 \times 10^{12}\mathrm{cm}^{-2}$ coupling to (a) MM I and (b) MM III. Black dashed lines indicate the polaritons, yielding a coupling strength of $\frac{\Omega_R}{\omega_0} = 0.83$ and 1.25 respectively. (c) For an enhanced doping density ($\rho_{\mathrm{2DEG,total}} = 6 \times 2.8 \times 10^{12}\mathrm{cm}^{-2}$) the coupling strength of a sixfold QW coupled to MM III increases further, reaching $\frac{\Omega_R}{\omega_0} = 1.48$.

4.1.2 Deep-strong light-matter coupling

Our studies aimed to enhance the coupling strength in Landau-quantized systems and even exceed the current record value of $\frac{\Omega_R}{\omega_0} = 1.43$ [17]. In the following, the enhancement of the coupling strength according to the unified treatment of both, the light and the matter mode, is demonstrated. We study the coupled systems by THz time domain magneto-spectroscopy, which gives access to the amplitude and the phase of the transmitted THz radiation. The transmitted THz waveforms ($E(t, B)$), are Fourier transformed to best visualize the polariton dispersion.

Sixfold quantum well stack

First, the sixfold QW (*GaAs1*), which was characterized in the previous section, is coupled to the LC resonance of MM I. The resulting transmission spectra as a function of ν_c are shown in Fig. 4.1.2a. The resonances are characterized by sharp transmission minima. As MM I, a positive resonator, does not cover the whole sample, the bare CR,

stemming from the uncoupled areas of the sample, is visible. The lower polariton (LP), emerging from the CR, and the upper polariton (UP) are marked by dashed lines. The polariton branches evolve with different curvatures. Numerical calculations allow for their identification according to the procedure discussed in Chapter 2.4.3. The additional resonances below the UP are attributed to off-resonant coupling of the CR to higher order modes of the metamaterial, magneto-plasmon contributions or inter-resonator coupling between adjacent resonators. At the anti-crossing point, the polaritons at $\nu_{\mathrm{LP}} = 0.4\,\mathrm{THz}$ and $\nu_{\mathrm{UP}} = 1.6\,\mathrm{THz}$ are separated by 1.2 THz. Applying the Hopfield fitting procedure for single mode coupling, a coupling strength of $\frac{\Omega_R}{\omega_0} = 0.83$ is determined. With such a high coupling strength, the structure is clearly in the ultrastrong coupling regime. To further enhance the coupling strength we reduce the vacuum mode volume and lower the resonator frequency, exploiting $\frac{\Omega_R}{\omega_0} \propto \omega_0^{-1/2}$. Therefore in a next step, the negative resonator MM III, with the reduced resonance frequency of $\nu_{\mathrm{LC}} = 0.5\,\mathrm{THz}$, is coupled to the sixfold quantum well stack. Owing to Babinet's principle, the system's resonances manifest themselves as local transmission maxima. Fitting the polaritons, marked by dashed lines in Fig. 4.1.2b, yields a coupling ratio of $\frac{\Omega_R}{\omega_0} = 1.25$. For this structure, we thus reach the deep-strong coupling regime, characterized by a normalized coupling strength exceeding unity.
We try to enhance it even further by increasing the doping density of another sixfold quantum well up to $\rho_{\mathrm{2DEG,total}} = 6 \times 2.8 \times 10^{12}\mathrm{cm}^{-2}$ (*GaAs2*). The light mode of MM III is again used to dress the Landau-quantized electrons. Fig. 4.1.2c shows the resulting transmission spectra. Unfortunately, the stronger the coupling gets, the harder the analysis of the spectra becomes. The UP is pushed to frequencies, which lie in the vicinity of higher order modes, whose origin is currently under investigation. Here, the upper polariton is almost indistinguishable. Consequently, the Hopfield fit is done using only the clearly discernible lower polariton. We find, that increasing the number of oscillators n by a factor of 0.64, compared to *GaAsI*, leads to $\frac{\Omega_R}{\omega_0} = 1.48$. Considering $\frac{\Omega_R}{\omega_0} \propto \sqrt{n}$, we would expect a slightly higher coupling strength of $1.25 \times \sqrt{0.64} = 1.6$. This discrepancy is caused by the strong dipole moment of the cyclotron transition, squeezing the light mode out of the QWs. We therefore observe light-matter decoupling, caused by the high coupling strength, predicted for coupling beyond unity.

Increased number of quantum wells

Given the findings of the previous section, an even higher doping of the QWs may be counterproductive as it possibly leads to lower coupling strengths. However, in order to still increase the number of dressed electrons, it seems interesting to rediscuss advantages and limiting parameters of an increase of the number of QWs in the stack: On the one hand, the vacuum mode decays over the quantum well stack [17], possibly leading to weaker coupling of the electrons in the deeper QWs. Therefore, increasing the number of stacked QWs seems unattractive at first. Yet, even if the remote QWs do not couple as strongly as the ones near to the sample surface, a fraction of the electrons might still couple, leading to an enhanced coupling strength. We thus started by increasing the QW stack from sixfold to 12-fold, while keeping the doping density constant. The coupling experiments (Fig. 4.1.2a), employing MM IV, demonstrate the success of this ansatz, as a relative coupling strength of $\frac{\Omega_R}{\omega_0} = 2$ has been achieved. For more details on the assessment of this sample see ref. [70].
We identify the stacking of QWs as a promising way to further boost the coupling strength. As an outlook, we strongly increased the number of QWs, while keeping their individual doping density and growth parameters constant. To this end, we fabricated samples, containing 24 and 48 QWs, and coupled them to MM IV, which promises high accordance with numerical calculations. Figs. 4.1.2b and c show the experimental data, obtained by EOS using a GaP nonlinear crystal, which allows for the detection of up to 7 THz, as well as the numerical calculations of the 24-fold QW and of 48-fold QW structure respectively. For the 24-fold QW (Fig. 4.1.2b), the LP is visible in both experimentally and theoretically obtained transmission spectra. Yet in the experiment, the allocation of the UP is not possible. The spectra lack the strongly structured transmission, which is observed in the theory. A similar behaviour of experiment and theory is given for the 48-fold QW (Fig. 4.1.2c): the LP can be identified, but the UP is not distinguishable. To unambiguously determine the coupling strength of these structures, they need to be further examined.
We conclude, increasing the number of QWs in a stack is indeed an encouraging approach to achieve ultimately high coupling strengths. As these high coupling strengths come with the challenge of multiple resonance in the vicinity of the UP, identifying the polaritons becomes hard and an exact determination of the coupling strength very challenging, but these obstacles may be tacked if the origin of the additional resonance becomes clear.

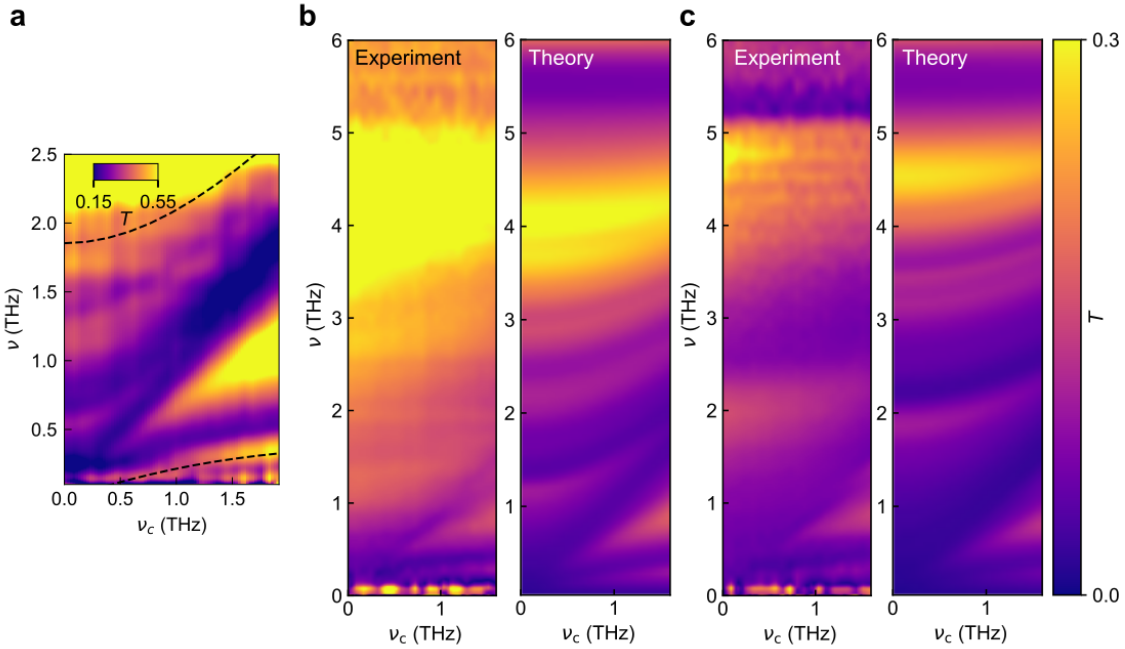

Figure 4.3: Strongly increased number of QWs. (a) Experimental transmission spectra of a 12-fold QW stack coupled to MM IV. The dashed lines indicate the polariton dispersion. (b)-(c) Experimental transmission (Experiment) and numerically calculated transmission (Theory) of (b) a 24-fold QW and (c) a 48-fold QW stack as a function of ν_c. The calculations were performed by Christoph Lange.

4.2 Light-matter coupling of cyclotron resonances in InAs quantum wells

In addition to an optimization of the heterostructure stack, to further increase $\frac{\Omega_R}{\omega_0}$, we try to strengthen the matter transition. Decreasing the effective mass of the electrons represents an efficient way to significantly increase the dipole moment. The decreased effective mass will lead to higher filling factors, at a given magnetic field, which leads to an enhancement of the coupling strength according to eq. 2.23. Possible candidates, with effective electron masses of $m_{\text{eff}} = 0.023\, m_{\text{e}}$ and $m_{\text{eff}} = 0.014\, m_{\text{e}}$ respectively, are indium arsenide (InAs) and indium antimonide (InSb) [62].
In the III-V-chamber of the MBE system used for this work, we are limited to the use of GaAs substrates, to avoid possible contamination of the chamber. Unfortunately, GaAs and the crystal structure of InAs and InSb have a large lattice mismatch. For InSb the mismatch amounts to $\Delta a = 14.6\%$, whereas for InAs it is $\Delta a = 6.7\%$. Growing these materials on GaAs substrates requires strain engineering, as the different lattice constants forbid direct epitaxial growth on GaAs. In this work, we use buffer systems for strain release management between the active quantum well region and the GaAs substrate. However, owing to the high mismatch of InSb, such a buffer system is substantially more complex for InSb-based heterostructures. Much effort has been put into optimizing the growth parameters of InAs-based structures to allow high mobility electron gases on GaAs substrates [75, 99–101]. Therefore we chose InAs-based material systems, to grow heterostructures hosting high quality 2DEGs.

4.2.1 InAlAs/InGaAs/InAs heterostructures

A $In_{81.5}Al_{18.5}As/In_{81.5}Ga_{18.5}As$ heterostructure with stepped InGaAs/InAs quantum wells, hosting 2DEGs, was chosen to serve as matter part for our light-matter coupling experiments. The heterostructure design is based on the work of M. Prager, but customized for the purpose of ultimately strong light-matter coupling. The active region, whose band structure is schematically depicted in Fig. 4.4, comprises an InAs inset of a thickness of 6 nm surrounded by 6 nm InGaAs. The InAs-channel-insertion is beneficial for the two-dimensional electron mobility [102, 103]. The QW is symmetrically n-doped through a

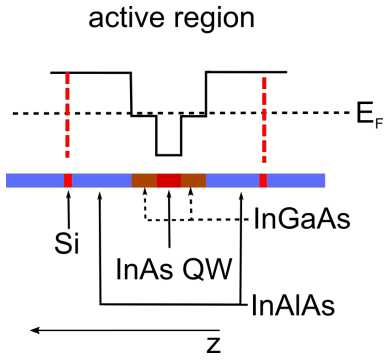

Figure 4.4: Schematic band structure of the InAlAs/InGaAs/InAs heterostructure. The active region, consisting of an InGaAs/InAs QW is surrounded by InAlAs barriers. This material composition leads to a stepped QW, which is populated by electrons from the Si-δ doping layer.

δ-doping layer at 20 nm distance in the InAlAs barrier of a width of 50 nm. A 2 nm InGaAs capping prevents oxidation of InAlAs. To enable strain relaxation and defect-free growth of a two-dimensional system on semi-insulating GaAs (001) substrate material, we employed a sophisticated buffer system to serve as so-called "virtual substrate" [104, 105]. Based on the epitaxial growth study of Capotondi et al. [106], a step-graded buffer, where the In concentration of $In_xAl_{1-x}As$ is increased stepwise, is used. A more detailed description of this heterostructure design and the employed buffer system is given in Appendix A.2.1.

Single quantum well

As a first test to optimize Landau-quantized electrons of stepped InGaAs/InAs 2DEGs for the coupling to subwavelength THz resonators, we grow a symmetrically doped single QW (*InAs1*). We perform magneto-transport measurements to characterize the two-dimensional system electronically by analysing the longitudinal ρ_{xx} and transversal resistivity ρ_{xy}. Fig. 4.5a depicts ρ_{xy} (red curve) and ρ_{xx} (black curve) as a function of the applied B-field. ρ_{xx} shows pronounced Shubnikov-de Haas (SdH) oscillations while ρ_{xy} contains horizontal plateaus at higher magnetic fields, indicating the quantum Hall effect. These are signatures for electron transport in a two-dimensional system in the QW. Note, that a small dip at zero magnetic field in the longitudinal resistivity indicates weak anti-localization, while for higher magnetic fields the SdH peaks are spin-split [78]. These features are characteristic for

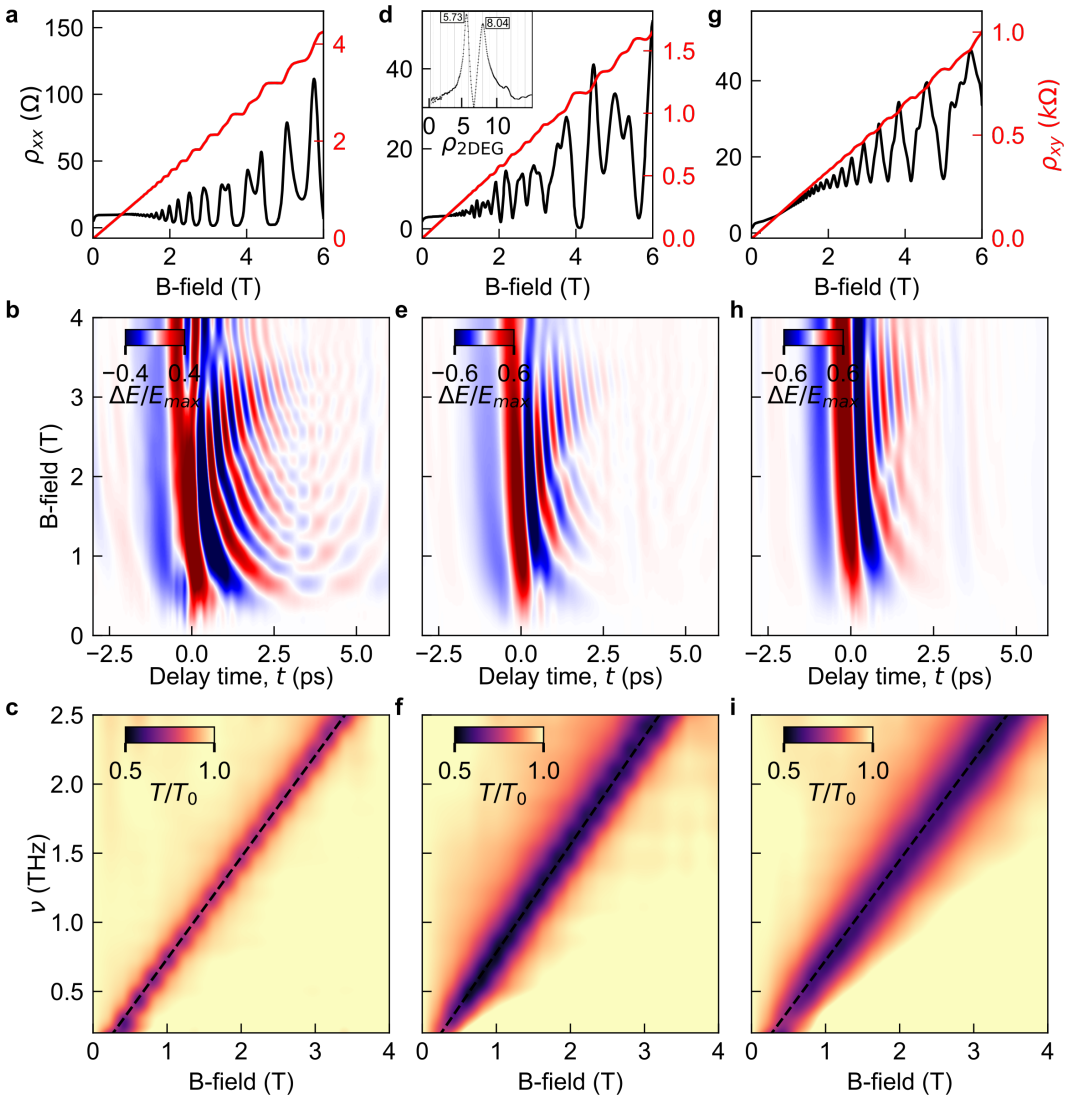

Figure 4.5: Electrical and optical characterization of a single and two threefold InAlAs/InGaAs/InAs QWs. (a) Magneto-transport measurement of the single QW heterostructure *InAs1*. Longitudinal (ρ_{xx}, red curves) and Hall resistivity (ρ_{xy}, black curves) reveal a total charge carrier density of $\rho_{2\mathrm{DEG}} = 9.2\times10^{11}$ cm^{-2} and a mobility of $\mu_e = 5.1\times10^5$ cm^2/Vs. (b) Time domain data of the transmitted normalized differential electric field $\Delta E/E_{\max}$ show pronounced CR oscillations. (c) Fourier transformation of the time domain data yields the transmission spectra which reveal an effective mass of $m^* = 0.038\,m_e$. (d)-(f) Corresponding measurements for the threefold QW *InAs2*, yield $\rho_{2\mathrm{DEG,total}} = 2.4\times10^{12}$ cm^{-2}, $\mu_e = 6.0\times10^5$ cm^2/Vs and $m^* = 0.036\,m_e$ obtained from the broadened CR. The inset in (d) shows FT of the SdH oscillations as a function of $1/B$. (g)-(i) Corresponding measurements for the threefold QW *InAs3*, yield $\rho_{2\mathrm{DEG,total}} = 3.6\times10^{12}$ cm^{-2}, $\mu_e = 6.5\times10^5$ cm^2/Vs and $m^* = 0.039\,m_e$.

an increased spin-orbit interaction and lower electron masses, compared to AlGaAs/GaAs systems. We determine a mobility $\mu_e = 5.1 \times 10^5\,\mathrm{cm}^2/\mathrm{Vs}$ and a sheet carrier density of $\rho_{2DEG} = 9.2 \times 10^{11}\,\mathrm{cm}^{-2}$.
To fully characterize the system, we perform THz time domain magneto-spectroscopy experiments, tracing the transmitted electric field E in dependence of external the B-field and the delay time t. Fig. 4.5b shows $\Delta E = E(B,t) - E(0,t)$. Here, the initial field at $B = 0\,\mathrm{T}$ is subtracted to better identify the polarization response of the 2DEG to the external magnetic field. The reemitted radiation oscillates at the CR frequency $\nu_c = \frac{eB}{2\pi m^*}$ as a function of B after illumination. The transmitted THz waveforms therefore contain the long-lived oscillations with circular polarization. The inter-Landau level spacing, increases with B, leading to higher frequency oscillations of the emitted THz field, visible in the B dependence of ΔE. Fourier transforming the time domain data into the frequency domain leads to the transmission spectra shown in Fig. 4.5c. The linear B dependence of the CR provides the effective mass $m^* = 0.038\,m_e$. From the linewidth of the CR it is clear, that its decay rate is relatively low, which can also be observed in the long-lived oscillations in the time domain data shown in b. Our InAs-based 2DEG therefore provides a low electron mass (about 50% of the mass of our GaAs system), a high carrier density as well as a high mobility. This is a good starting point for the development of InAlAs/InGaAs/InAs heterostructures for extremely strong light-matter coupling.

Threefold quantum well stack

We continued our study by growing a threefold QW stack with a slightly increased doping density (*InAs2*). The QWs are separated by 40 nm InAlAs barriers, containing a Si δ-doping layer in the middle (see Appendix A.2.1). The magneto-transport measurements reveal pronounced SdH oscillations of the longitudinal resistivity (Fig. 4.5d, black curve) and the typical Hall plateaus in the transversal resistivity (red curve). Under the assumption that the three QWs have very similar transport properties, we determine the electron mobility $\mu_e = 6.0 \times 10^5\,\mathrm{cm}^2/\mathrm{Vs}$ and the total sheet density $\rho_{2DEG,total} = 2.4 \times 10^{12}\,\mathrm{cm}^{-2}$. This corresponds to a slightly smaller density of each QW compared to *InAs1*. The observed features in the transport measurements indicate, that we still achieved a clearly defined two-dimensional electronic system. Yet, there is a pronounced beating in ρ_{xx}, which we

attribute to different electron densities in the three QWs. As the Landau level DOS exhibits a $1/B$-periodicity, we Fourier-transform (FT) ρ_{xx} as a function of $1/B$ to identify different carrier densities in the QWs. The resulting frequency spectra contain the electron densities, which can be extracted as following:

$$f^{-1} = \Delta(1/B) = \frac{2e}{\rho_{\mathrm{2DEG}} h}, \tag{4.3}$$

with Planck's constant h. The FT of ρ_{xx} over $1/B$ (Fig. 4.5d, inset) of the threefold QW, reveals two closely-spaced frequencies in the spectrum. They correspond to densities of $\rho_{\mathrm{2DEG}} = 5.7 \times 10^{11}\,\mathrm{cm}^{-2}$ and $\rho_{\mathrm{2DEG}} = 8.1 \times 10^{11}\,\mathrm{cm}^{-2}$. This suggest that the QWs are indeed differently populated, which may impact the determined mobility. In order to investigate perturbation effects of this difference in QW population in the optical experiments, we next study the threefold QW in the magneto-spectroscopy setup.
The time domain data (Fig. 4.5e) show, varying with the magnetic field, cyclotron resonance oscillation. They are more strongly damped compared to the CR oscillations of the single QW in Fig. 4.5b. Considering that the mobility of the electrons is not significantly reduced compared to the single QW, this additional damping indicates superradiant decay of the electrons interacting with the incident THz light or an influence of the different population of the QWs. The Fourier transform of the measurement, yielding the transmission spectra, is depicted in Fig. 4.5f. The increased sheet carrier density interacting with the THz light causes a strengthened absorption at resonance. It is evident, that the CR resonance is indeed broadened. The experimentally obtained CR lifetime $\tau_{\mathrm{CR,exp}} = 0.87\,\mathrm{ps}$ is slightly higher compared with $\tau_{\mathrm{CR}} = 0.85\,\mathrm{ps}$ which is calculated according to eq. 4.2. While the slight discrepancy between $\tau_{\mathrm{CR,exp}}$ and τ_{CR} may result from the inhomogeneous population of the QWs, the lifetime is clearly limited by superradiance. As a consequence, we conclude that the difference in the population of the QW does not strongly influence the optical properties of the structure.
Nevertheless, we try to equalize the occupation of the QWs by slightly changing the doping ratio. At the same time, we increase the doping density of all QWs. The magneto-transport measurement of this sample (*InAs3*), shown in Fig. 4.5g, evidences the success of the effort: ρ_{xx} demonstrates, that the electron density of the three QWs is more homogeneous, as no beating is apparent. This is accompanied by an increased total electron sheet density of

$\rho_{2DEG,total} = 3.6 \times 10^{12}\,cm^{-2}$, while the electron mobility $\mu_e = 6.5 \times 10^5\,cm^2/Vs$ remains at a similar level. Note, that there is a parabolic background on the SdH oscillations apparent, which is a sign of bulk conduction, contributing in parallelly to the 2DEGs. The transversal resistivity also exhibits features of this parallel channel, namely flattening of the Hall curve at higher magnetic fields. From experiences in our group, we attribute this parallel bulk conduction to conduction inside the remote doping layer, resulting from incompletely ionized donors. To reach full ionization, the doping density would have to be slightly reduced or the distance of the remote doping layer to the QW further optimized. To test the influence of this parallel conduction in optical experiments, where THz radiation excites the CR, we study the structure in the THz time domain setup. The transmitted THz waveforms as a function of the external magnetic field show that the CR oscillations are a little more damped, but still very well discernable (Fig. 4.5h). The slight reduction of the CR decay time is best seen in the transmission spectra (Fig.4.5i) and again attributed to increased superradiant damping.

Sixfold quantum well stack

Instead of further optimizing the doping scheme, we decide to increase the amount of QWs analogously to Chapter 4.1. Thus, we next grow a structure consisting of six QWs (*InAs4*), each doped in the same way as *InAs3*. The magneto-transport measurements (Fig. 4.6a), identify a total electron sheet carrier density of $\rho_{2DEG,total} = 7.8 \times 10^{12}\,cm^{-2}$. We assume that all QWs are very similar, since there is no pronounced beating visible in the SdH oscillations (Fig. 4.6a, black curve). As expected, there are still signs of parallel bulk conduction, since the doping scheme is identical to *InAs3*. However, the mobility of the electrons remains on a quite high level ($\mu_e = 6.4 \times 10^5\,cm^2/Vs$). The CR, obtained through THz time domain magneto-spectroscopy (Fig. 4.6b), of this structure is strongly broadened through superradiant damping of the collective excitation. Considering that the scattering decay time $\tau_{scatter}$, which is obtained in the transport measurements, is 13 ps, we find indeed, that superradiance is the dominant decay mechanism. The decay rate $\tau_{CR} = 0.22\,ps$ obtained through eq. 4.2 corresponds to the experimental CR decay time $\tau_{CR,exp} = 0.23\,ps$. This accordance confirms our argumentation, that the broadening of the linewidth is caused by superradiance.

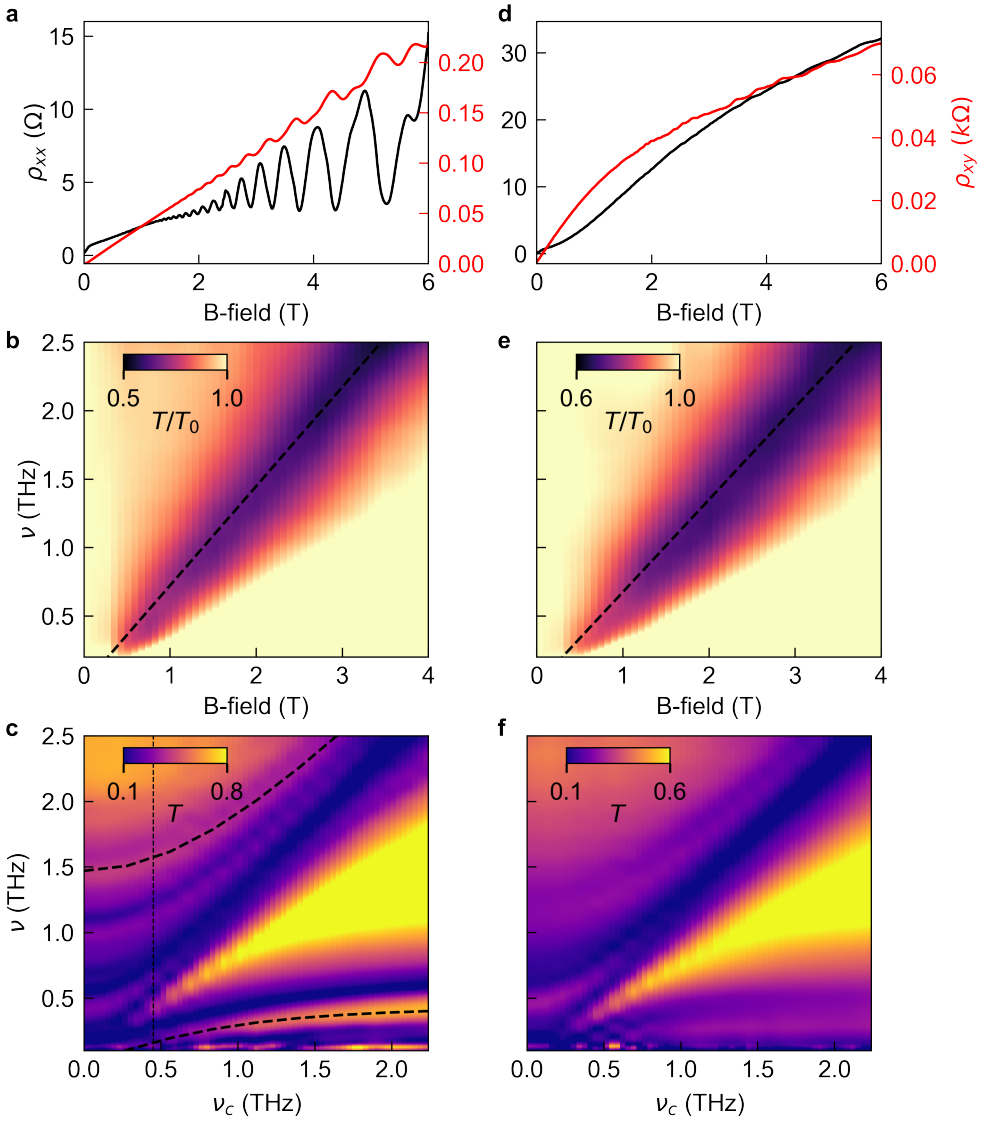

Figure 4.6: Six-fold InAlAs/InGaAs/InAs QWs *InAs4* and *InAs5*. (a) The magneto-transport measurement of the longitudinal (ρ_{xx}, red curve) and Hall resistivity (ρ_{xy}, black curve) of *InAs4* yield a total charge carrier density of $\rho_{\mathrm{2DEG,total}} = 7.8 \times 10^{12}\,\mathrm{cm}^{-2}$ and a mobility of $\mu_\mathrm{e} = 6.4 \times 10^5\,\mathrm{cm}^2/\mathrm{Vs}$. (b) Magneto THz absorption measurement reveal an effective mass of $m^* = 0.039\,m_e$. (c) Optical response of the QW stack coupled to MM IV shows a distinct polariton dispersion. The Hopfield fit yields a coupling strength of $\frac{\Omega_R}{\omega_0} = 1.67$. (d)-(f) Corresponding measurements for the more highly doped sixfold QW (*InAs5*) with a total charge carrier density of $\rho_{\mathrm{2DEG,total}} = 1.1 \times 10^{13}\,\mathrm{cm}^{-2}$ and a mobility of $\mu_\mathrm{e} = 5 \times 10^5\,\mathrm{cm}^2/\mathrm{Vs}$, yielding an effective mass of $m^* = 0.041\,m_\mathrm{e}$. The coupling strength can not be determined as the polaritons are not identifiable.

Having achieved a sheet carrier density of roughly the same magnitude as for GaAs, while reducing the effective mass significantly by 50%, we decide to couple the sixfold QW to the compact metamaterial MM IV ($\nu_{\mathrm{LC}} = 0.5\,\mathrm{THz}$) (Fig. 4.6c). The polaritons, marked by dashed lines, manifest as transmission maxima. The LP and UP resonances are identified by their distinct features, separated by 1.42 THz at the anti-crossing point (vertical line). Beneath the upper polariton branch, coupled modes originating from off-resonant coupling of higher-order modes, appear. These modes are pushed into the spectral range of interest, due to the high coupling strength [55]. The UP is strongly blue-shifted, the shift being particularly prominent at $\nu_{\mathrm{c}} = 0$. This shift is caused by the diamagnetic interaction, which becomes increasingly relevant for increasing coupling strengths. Fitting the polariton dispersions with the Hopfield formula yields a relative coupling strength of $\frac{\Omega_R}{\omega_0} = 1.67$. This interaction strength even exceeds the highest published coupling strength in Landau systems [17], achieved for a sixfold AlGaAs/GaAs QW stack, by 16%.

As an outlook, we increase the doping density once more (*InAs5*). This leads to a strong parallel channel, leaving almost no sign of a 2D system in the magneto-transport measurements (Fig. 4.6d). We determine a total electron density of $\rho_{\mathrm{2DEG,total}} = 1.1 \times 10^{13}\,\mathrm{cm}^{-2}$ and a mobility of $\mu_{\mathrm{e}} = 5 \times 10^5\,\mathrm{cm}^2/\mathrm{Vs}$. The CR on the other side is, compared to *InAs4*, not significantly broadened (Fig. 4.6e), raising the hope, for successful coupling experiments. Unfortunately, testing this in a coupling experiment by applying MM IV, revealed that there are no distinct polaritons visible. The transmission spectra (Fig. 4.6f) appear washed-out, so we can not determine a coupling strength. This is probably the effect of over doping the QWs.

In conclusion, we achieved deep-strong coupling in InAlAs/InGaAs/InAs heterostructures, with a record high coupling strength of $\frac{\Omega_R}{\omega_0} = 1.67$, compared to the highest published coupling strength of $\frac{\Omega_R}{\omega_0} = 1.43$ [17] at the time of this thesis. Though this is quite a success, stacking a greater number of QWs is a fitting ansatz to raise the number of coupled oscillators and thereby increase the coupling strength. However, in our InAs-based structures we achieved electron densities of only up to $\rho_{\mathrm{2DEG,InAs}} = 1.3 \times 10^{12}\,\mathrm{cm}^{-2}$ per QW, which is still lower than for our GaAs-based heterostructures ($\rho_{\mathrm{2DEG,GaAs}} = 2.8 \times 10^{12}\,\mathrm{cm}^{-2}$ per QW). This shows an additional possibility to enhance the coupling strength by further optimizing the heterostructure growth. Developing a better doping scheme may allow for a higher sheet carrier density in a QW, without resulting in parallel bulk conduction.

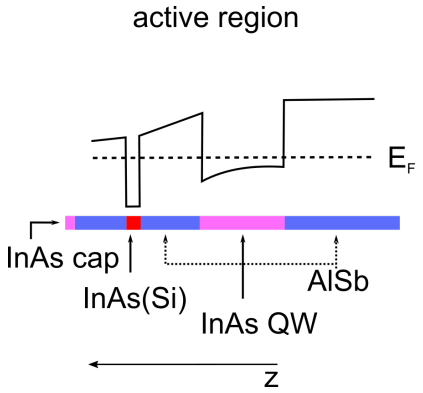

Figure 4.7: Schematic band structure of the AlSb/InAs heterostructure. The active region consists of an InAs QW surrounded by AlSb barriers. A δ-type Si-doped InAs layer serves as remote modulation doping for the QW.

In fact, there is a InAs-based material system, that is known for it's high carrier densities even without intentional doping [99]: AlSb/InAs QWs.

4.2.2 AlSb/InAs heterostructures

To solve the problem of relatively low charge carrier densities imposed by the epitaxial limitations for the growth of InAlAs/InGaAs/InAs, we study pure InAs QWs buried in AlSb barriers. A thin InAs layer in AlSb barriers leads to the formation of deep quantum wells, with a potential barrier of 1.35 eV. These deep QWs provide especially good confinement and, quite importantly for our purposes, allow carrier densities of up to 10^{13}cm^{-2} [99] through modulation doping. Combined with the low effective mass of InAs ($m^* = 0.023\, m_e$), heavily doped InAs quantum wells appear to be perfect candidates for ultimately strong light-matter coupling. Combining AlSb barriers and InAs layers leads to a band line-up that differs from the widely studied AlGaAs/GaAs structures: A type II heterostructure is formed. The valence band (VB) of InAs drops below the VB of AlSb. The conduction band on the other side has an exceptionally large band offset between AlSb and InAs of 1.35 eV [107].

Sample layout

The MBE growth of this heterostructure is performed on lattice mismatched GaAs substrate, which necessitates proper buffer layers. The employed buffer structure is based

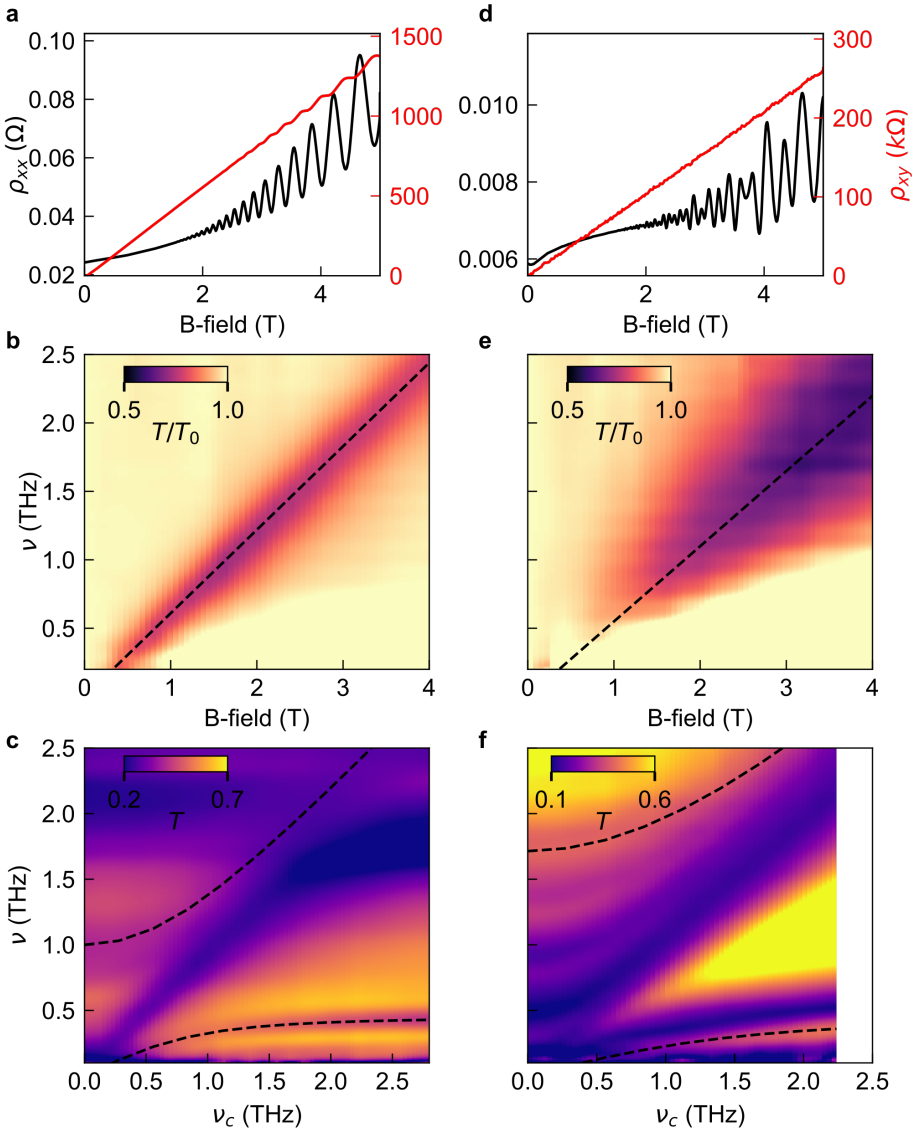

Figure 4.8: Single and three-fold AlSb/InAs QWs *InAs6* and *InAs7*. (a) Magneto-transport measurements of the longitudinal (ρ_{xx}, black curve) and the Hall resistivity (ρ_{xy}, red curve) show characteristic SdH oscillations and Hall plateaus. They allow for the determination of the charge carrier density of $\rho_{2\mathrm{DEG}} = 2.1 \times 10^{12}\mathrm{cm}^{-2}$ and an electron mobility of $7.5 \times 10^4\,\mathrm{cm/Vs}$. (b) THz absorption measurement with perpendicularly applied magnetic field (B) shows a narrow CR with a slope revealing an effective mass of $m^* = 0.046\,m_e$ of the Landau-quantized electrons. (c) Coupling to MM II leads to formation of polaritons visible in the transmission spectra as a function of ν_c and marked by dashed lines. A Hopfield fit yields a coupling strength of $\frac{\Omega_R}{\omega_0} = 0.99$. (d)-(f) Corresponding measurements of the three-fold QW *InAs7*. We estimate the total density $\rho_{2\mathrm{DEG,total}} = 8.1 \times 10^{12}\,cm^{-2}$ and an effective mass of $m^* = 0.050\,m_e$. Coupling the QW stack to MM IV leads to a normalized coupling strength of $\frac{\Omega_R}{\omega_0} = 1.8$.

on studies of Charpentier [108] and presented in detail in Appendix A.2.2. The active region of the heterostructure, schematically depicted in Fig. 4.7, consists of 200 nm AlSb, 15 nm InAs, 12.5 nm AlSb, 1.2 nm InAs(Si), 10 nm AlSb and 2 nm InAs capping. Owing to the fact that AlSb/InAs heterostructures form extremely deep potential wells, even energetically deep donors in the barrier stemming from unavoidable crystal defects will give electrons to the well. It has been shown, that not-intentionally doped QWs show relatively high electron densities [109]. But, in order to maximize the coupling strength, we increase the sheet carrier density by modulation doping with Si. In contrast to the remote δ-doping in AlGaAs/GaAs heterostructures, a δ-doping layer with Si in the AlSb barrier would have a p-doping effect [110]. To overcome this problem, Bennet et al. [111] introduced a thin and highly n-doped δ-type InAs(Si) donor layer. This layer acts as modulation-doping in combination with AlSb spacer layers for the InAs QWs.

Single quantum well

To test our new heterostructure, we grow a single QW sample (*InAs6*), as described above, and determine the transport behaviour through magneto-transport measurements. ρ_{xy}, the Hall resistivity (Fig. 4.8a, red curve), allows for the determination of the electron sheet carrier density of $\rho_{\mathrm{2DEG}} = 2.1 \times 10^{12}\mathrm{cm}^{-2}$. This value represents the highest sheet carrier density achieved in our InAs-based heterostructures so far. For the calculation of the electron mobility, the SdH oscillations of ρ_{xx} (Fig. 4.8a, black curve) are studied. They yield a mobility of $\mu_{\mathrm{e}} = 75000\,\mathrm{cm}^2/\mathrm{Vs}$, which is according to eq. 2.26 sufficiently high for a CR to build-up. Note that there are signs of a parallel bulk conduction channel apparent: the slight parabolic background of ρ_{xx} and a weak nonlinearity at zero magnetic field of ρ_{xy}.

To investigate the optical response of this structure, we study the single QW in our THz time domain magneto-spectroscopy setup. The Fourier transformation of the obtained time domain data yields the transmission spectra as a function of ν_{c} (Fig. 4.8b). There is a distinct CR visible. This direct measurement of the CR allows for the determination of the effective mass. Following eq. 4.1, we determine $m^* = 0.046\,m_{\mathrm{e}}$. This value strongly exceeds the mass of bulk InAs ($m^* = 0.023\,m_{\mathrm{e}}$). We will thus discuss the possible influence of non-parabolicity effects in these narrow QWs.

Influence of non-parabolicity

A two band model, taking non-parabolicity into account, offers the possibility to describe the electron dispersion in AlSb/InAs QWs. Its non-parabolicity and at the same time high confinement potential strongly affect the effective cyclotron mass m_c^* according to Gauert et al. [112].
In general the effective mass follows the relation

$$\frac{1}{m^*} = \frac{1}{\hbar}\frac{\partial^2 E(\vec{k})}{\partial k^2} \tag{4.4}$$

with the energy dispersion $E(\vec{k})$. For a parabolic dispersion the effective mass is isotropic. In InAs this holds true for small k-vectors, but with increasing k the parabolicity decreases. In two-dimensional systems, where the motion perpendicular to the plane is discretizised, only discrete momentum vectors $k_\perp$ are allowed. The in-plane energy dispersion $E(k_\parallel)$, the subband dispersion, is then a projection of the three-dimensional energy dispersion on the $k_\perp$-plane. For their non-parabolicity, the energy of quantum wells deviates from its bulk material dispersion. In fact, the narrower the well, the higher is the subband energy and consequently the non-parabolicity. In a two band model, the energy of extremely narrow InAs QWs can be written as

$$E(E - E_g) = E_g \frac{\hbar(k_\parallel^2 + k_\perp^2)}{2m_0^*}, \tag{4.5}$$

with the bandgap energy $E_g = 0.42\,\mathrm{eV}$ and the bulk effective mass m_0^*. In the effective mass approximation, quantization in $k_\perp$ leads to the subband energy E_0^{EMA}. The energy then reads

$$E = \frac{E_g}{2} + \sqrt{\frac{E_g^2}{4} + E_g E_0^{EMA} + E_g \frac{\hbar^2 k_\parallel^2}{2m_0^*}}. \tag{4.6}$$

It is now clear that the electron energy is not simply the sum of the subband energy E^{EMA} and the kinetic energy $E_\parallel$. This complexity originates in the coupling of the motion parallel and perpendicular to the plane, arising from the interaction between conduction and valence

band for small E_g, which is the case for InAs. Semi-classical calculations yield the Fermi velocity

$$v_F = \frac{1}{\hbar}\frac{\partial E}{\partial k_\parallel} = \frac{E_g}{E_g + 2E}\frac{\hbar k_{\parallel F}}{m_0^*}. \tag{4.7}$$

This leads via the Lorentz force, $\hbar\dot{k} = ev_F B$, to the following relation for the CR frequency

$$\omega_c = \frac{\dot{k}}{k_{\parallel F}} = \frac{E_g}{E_g + 2E}\frac{eB}{m_0^*}, \tag{4.8}$$

with the effective cyclotron mass

$$m_c^* = \frac{E_g 2E}{E_g} m_0^*. \tag{4.9}$$

Taking the density of states of a two-dimensional system into account, we obtain an analytical expression for the dependence of the cyclotron mass on the carrier density ρ_{2DEG}:

$$m_c^* = \frac{2m_0^*}{E_g}\sqrt{\frac{E_g^2}{4} + E_g E_0^{EMA} + E_g\frac{\pi\hbar^2\rho_{2DEG}^2}{2m_0^*}}. \tag{4.10}$$

Eq. 4.10 shows that with rising charge carrier density, the cyclotron mass increases whereby the slope of this increase is determined by the subband energy, related to the QW width. For a single AlSb/InAs QW with a sheet density of $2.1 \times 10^{12}\mathrm{cm}^{-2}$, we calculate the effective mass $m_c^* = 0.048\, m_e$. This result is in good agreement with the experimentally obtained value of $0.046\, m_e$. Therefore non-parabolicity, which is pronounced in narrow QWs, needs to be taken into consideration for the design of AlSb/InAs heterostructures.

Light-matter coupling of the single quantum well

The effective mass, that is reached in this system is 15% higher than in the InAlAs/InGaAs/InAs structures, but still considerably lower than in GaAs. The extremely high electron sheet density, on the other side should enhance the coupling strength even further. To test the single QW structure, we couple the Landau-quantized electrons to the LC resonance of MM II. Fig. 4.8c shows the resulting transmission spectra. There is a sharp LP and a broader UP visible. Fitting the polariton dispersions (marked by dashed lines) by applying

the Hopfield formula yields a coupling strength of $\frac{\Omega_R}{\omega_0} = 0.99$. This is a good starting point for the realization of deep-strong coupling of AlSb/InAs heterostructures.

Threefold quantum well

In order to further increase the number of oscillators, we fabricate a threefold QW structure (*InAs7*). Its design was guided by band structure calculations conducted with a self-consistent Schrödinger-Poisson-solver in our group by V. Zeller [113]. A detailed description of the multi-QW stack is presented in Appendix A.2.1. The transport properties of the QW stack are characterized by magneto-transport measurements depicted in Fig. 4.8d. ρ_{xy} (red curve) does not show Hall plateaus, which signalizes high filling factors due to a high carrier density. The SdH oscillations of ρ_{xx} (black curve) show a pronounced beating, indicating different electron densities in the wells and possible occupation of a second QW subband [114]. This inhibits the determination of the electron mobility. A Fourier transformation according to eq. 4.3 at weak magnetic fields, confirms both considerations: There are multiple distinct electron densities recognisable. The average electron density in the first subband is $\rho_{2DEG} = 2.7 \times 10^{12}\text{cm}^{-2}$, resulting in a total density of $\rho_{2DEG,total} = 8.1 \times 10^{12}\text{cm}^{-2}$.
The optical response of this structure (Fig. 4.8e) shows a considerably broadened CR. We attribute this to coherent superradiant decay of the CR. Applying eq. 4.2 [98], we get a decay time of $\tau_{CR} = 0.21$ ps, which is in good agreement with the experimentally obtained value of 0.29 ps. Superradiance is therefore identified as the mechanism causing the strongly increased decay rate of the coherent cyclotron oscillations (for reference: $\tau_{scatter} = 1.8$ ps of the single QW obtained through magneto-transport measurements). Caused by the increased charge carrier density, the effective mass is $m^* = 0.050\, m_e$.
Coupling to metamaterial MM IV leads to the transmission spectra shown in Fig. 4.8f. The LP and UP, visible as transmission maxima, are marked by dashed lines. A Hopfield fit yields a coupling strength of $\frac{\Omega_R}{\omega_0} = 1.8$, which corresponds to the expected coupling strength of $\frac{\Omega_R}{\omega_0} = \sqrt{\frac{8.1}{2.3}} \times 0.99 = 1.86$ according to eq. 2.17 . This result considerably exceeds the highest published coupling strength of Landau polaritons [17]. Achieving such a high coupling strength for a threefold QW is already quite promising for further coupling experiments, with heterostructures comprising a higher number of QWs. However, there is

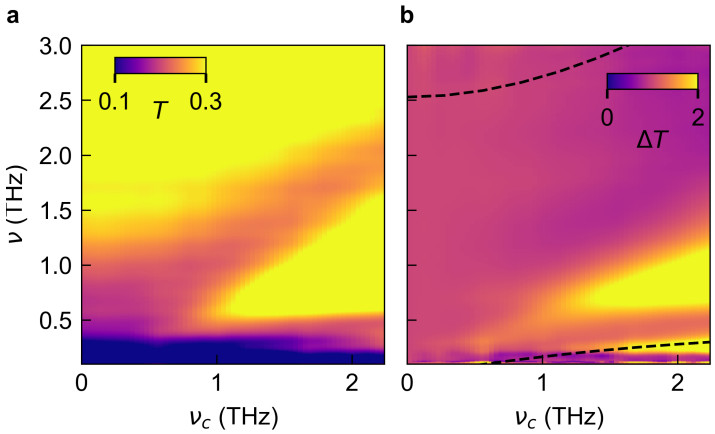

Figure 4.9: Deep-strong coupling of the sixfold AlSb/InAs QW stack. (a) Transmission spectra as a function of ν_c of *InAs8* coupled to MM IV. The polaritons are not clearly identifiable. (b) Differential transmission of the same measurements, allows for the identification of the LP. A Hopfield Fit yields the coupling strength $\frac{\Omega_R}{\omega_0} = 2.76$.

still potential to improve the doping scheme of these structures, as there is a strong parallel bulk conduction channel.

4.2.3 Deep-strong light-matter coupling exceeding $\frac{\Omega_R}{\omega_0} = 2$

As an outlook, we further increase the number of QWs and grow a sixfold QW stack. For such a sample we expect a coupling strength strongly exceeding $\frac{\Omega_R}{\omega_0} = 2$, since $\frac{\Omega_R}{\omega_0} = \sqrt{2} \times 1.8 = 2.54$. Superradiance in this sample does not allow for the identification of a CR in the uncoupled transmission measurements. For our coupling experiments, we use again the compact resonator MM IV. Fig. 4.9a shows the transmission spectra for the coupled system. There is only a very faint signal of the LP, so we referenced $T(B, \nu)$ to $T(0, \nu)$, the transmission spectrum at zero magnetic field. Fig. 4.9b shows the referenced spectra $\Delta T(B, \nu)$: Now, the LP branch is recognisable in the spectra, while they are still lacking the UP resonance. A possible explanation for its absence is the limited bandwidth of the detector crystal, allowing detection only up to $\approx$ 2.5 THz. In order to extract a coupling strength, we fit only the LP. However, this procedure is somewhat problematic, as Keller et al. [115] very recently discussed a red shift of the polariton states for a highly

non-parabolic dispersion. As we did not observe such a behaviour in our samples, with a visible UP, we assume that non-parabolicity in our QWs is not sufficiently high to have an effect on the polariton dispersion. Fitting only the LP with the Hopfield fit procedure explains the absence of the UP, as the calculated UP resonance at $B = 0\,\mathrm{T}$ already exceeds 2.5 THz and thus shifts even further out of our spectral limit at higher magnetic fields. The coupling strength for this system is $\frac{\Omega_\mathrm{R}}{\omega_0} = 2.76$, the highest coupling strength measured up to date.

Resuming the different material systems investigated in this work, we conclude that it is possible to increase the coupling strength by strengthening the dipole moment of the matter transition. AlGaAs/GaAs heterostructures, the most thoroughly studied material system for Landau polaritons [32], offer the possibility to tightly stack a high number of highly doped QWs, while a sufficient mobility of the electrons is provided. The electron sheet density of a single QW can reach $\rho_\mathrm{2DEG} > 2.8 \times 10^{12}\mathrm{cm}^{-2}$, but the effective mass of the electrons $m^* = 0.073\,m_\mathrm{e}$ is rather high compared to InAs-based 2DEGs (0.038 - $0.046\,m_\mathrm{e}$). InAlAs/InGaAs/InAs heterostructures on the other hand are characterized by an electron mass of about $m^* = 0.038\,m_\mathrm{e}$, but do not reach adequately high electron densities yet. AlSb/InAs QWs in contrast unite low effective masses ($m^* = 0.046\,m_\mathrm{e}$), high electron sheet carrier densities ($\rho_\mathrm{2DEG} = 2.7 \times 10^{12}\mathrm{cm}^{-2}$) and the capability to stack multiple QWs, making this the most promising material system for ultimately high light-matter coupling. With a sixfold AlSb/InAs QW structure, we achieved a coupling strength of $\frac{\Omega_R}{\omega_0} = 2.76$ corresponding to a population of the ground state of 0.9 virtual photons. This is 2.4 times the virtual photon population achieved in Landau polariton systems by Bayer et al. [17] and 1.73 times the number of virtual photons achieved in light-matter coupled systems in general [60]. Converting these virtual photons to real photons would lead to a signal, which is additionally enhanced by the resonator design. The compact design of resonator MM IV allows on the same area four times as many resonators on the same area as MM II, which is used in ref. [17]. However, for those photons to be emitted, there is still the need for a non-adiabatic switching functionality compatible with InAs QWs. A possibility are superconducting metamaterials [116, 117]. In the following Chapter a subcycle switchable resonator design, which is compatible with AlGaAs/GaAs QWs is presented.

5 Subcycle switchable resonators

Non-adiabatic modulation of the coupling strength in the ultra- or deep-strong coupling regime is predicted to release the virtual photon population of the ground state of this coupled system [7, 8]. This modulation can be achieved by either switching of the matter mode or the light mode. A subcycle switch-on of the matter part of an ultrastrongly coupled system has been shown by optical activation of the electronic occupation of a intersubband transition [118]. However, switching-on the matter excitation is not applicable for our Landau-quantized electron system, a model system for extremely strong coupling established by our group [17] and others [13, 55, 61, 119]. To still be able to manipulate the coupling strength of a Landau polariton system, an active THz metamaterial represents a convenient way.
There are various structures for active control [120] of the THz wave intensity by electrical [121, 122], mechanical [123, 124] and thermal [125] means. But in order to tune light-matter interaction non-adiabatically, on time scales shorter than one oscillation of light, optical control [126–130] of the switching is necessary. We therefore developed an active resonator, that can be deactivated on a subcycle timescale. This resonator, incorporating a photo-excitable semiconductor compatible with AlGaAs/GaAs quantum wells, allows for the selective switch-off of the fundamental resonator mode, while leaving a heterostructure unaffected.

5.1 Switching concept

The subwavelength switchable THz resonator MM I features a loop-current-based resonance, denoted LC resonance with a resonance frequency of $\nu_{\mathrm{LC}} = 0.8\,\mathrm{THz}$ and a higher order, dipolar (DP) resonance with a resonance frequency of $\nu_{\mathrm{DP}} = 1.6\,\mathrm{THz}$. The design of our switchable structures is based on finite-element frequency domain calculations (see

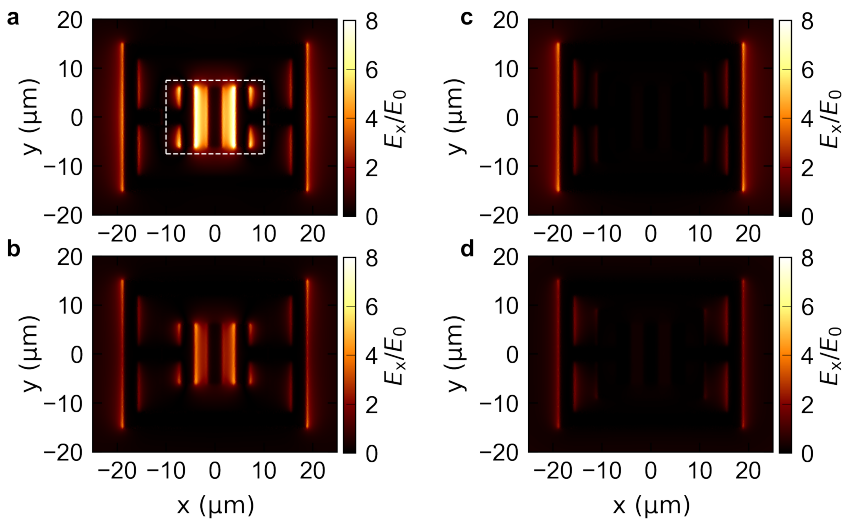

Figure 5.1: Calculated spatial characteristics of the photo-switchable resonator MM I. (a) Enhancement of the near-field amplitude, E_x, of the fundamental LC mode relative to the far-field amplitude, E_0, at a depth of z = -200 nm, for an undoped switching layer. (b) Corresponding near-field enhancement of the dipolar mode. (c) Near-field enhancement with doped switching layer, for the LC mode, and (d), for the dipolar mode.

Chapter 2.4.3), giving access to the spectrally resolved near- and far-field distribution of the resonator. The THz resonators, arranged in quadratic unit cells of a length of 60 μm, feature a capacitive gap element in which the electric field of the fundamental LC mode is enhanced by up to a factor of 8 with respect to the far field (Fig. 5.1a). In contrast, the near field of the higher-energy, dipolar mode (DP) is much weaker and more homogeneously distributed over the outer perimeter of the resonator (Fig. 5.1b). The differences discussed in Chapter 2.4.2 arise from the different origins of the modes. The DP mode stems from the dipolar currents along the resonator's components, whereas the LC mode is defined by the gap elements perpendicular to the electric field of an incident THz wave. Given the strong concentration of the near-field resonance within the capacitive gap of the split ring resonator (SRR), shortening this gap with a conductive material represents an efficient strategy to switch-off the fundamental resonant mode. In order to reach ultimately short timescales for this switch-off process, the shortening of the capacitive gap element will be triggered by ultrashort optical pulses. In our FEFD model, we include such a photo-conductive material between the substrate and the metallic metamaterial to test this hypothesis. The material addition is reduced to a patch-size (marked by dashed lines in Fig. 5.1a) only covering the capacitive gap region in order to selectively switch-off only the LC mode. Since we do not want the matter system to be perturbed by the optical switching pulse, it is important to appropriately choose the photo-conductive material. The switching concept will be demonstrated for our GaAs-based model system. We use $In_{0.55}Ga_{0.45}As$ as the photo-dopable switching patch material, since it has a smaller band gap than GaAs. We can thus excite charge carriers in the switching patch without affecting the quantum wells. In our numerical model, we apply the Drude model for a charge carrier plasma to calculate the contribution that the photo-excitation adds to the dielectric response of the switching patch, in order to test its potential to switch-off the LC resonance. The plasma frequency is given by

$$\omega_\mathrm{p} = \sqrt{\frac{\rho_\mathrm{switch} e^2}{\epsilon_0 m_\mathrm{InGaAs}}}. \tag{5.1}$$

Here, ρ_switch is the photo-excited electron charge carrier density, m_e the free electron mass, ϵ_0 is the vacuum permittivity, $m_\mathrm{InGaAs} = 0.04\, m_\mathrm{e}$ denotes the effective mass of conduction band electrons in bulk InGaAs, and e is the elementary charge. We assume a density of photo-excited carriers of $\rho_\mathrm{switch} = 3.5 \times 10^{18}\,\mathrm{cm}^{-3}$, corresponding to the total density of

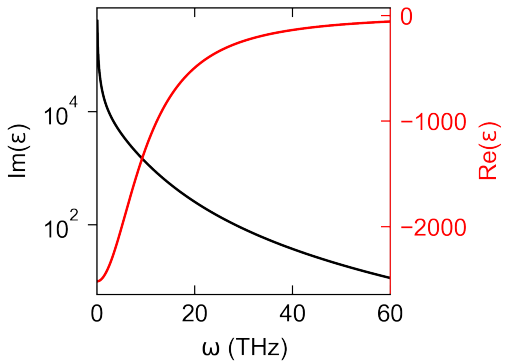

Figure 5.2: Implementation of the switching patch. Implemented Drude model for the InGaAs doped ($\rho_{\mathrm{switch}} = 3.5 \times 10^{18}\,\mathrm{cm}^{-3}$) switching patch. The imaginary part (black curve) of the additional dielectric function is in the order of 10^{4-5} and the real part (red curve) is strongly negative, rendering the patch quasi-metallic.

states of InGaAs within the bandwidth of our switching pulse. As a result, we obtain a plasma frequency of $\nu_{\mathrm{p}} = \frac{\omega_{\mathrm{p}}}{2\pi} = 80\,\mathrm{THz}$. The dielectric function of the plasma (Fig.5.2) is then given by

$$\epsilon_{\mathrm{InGaAs}}(\omega) = \epsilon_{\mathrm{InGaAs}}(\infty) - \frac{\omega_{\mathrm{p}}^2 \tau_{\mathrm{s}}^2}{\omega^2 \tau_{\mathrm{s}}^2 + i\omega\tau_{\mathrm{s}}}, \tag{5.2}$$

where we chose a scattering time of $\tau_{\mathrm{s}} = 1 \times 10^{-13}\,\mathrm{s}$, and a static dielectric constant of $\epsilon_{\mathrm{InGaAs}}(\infty) = 13.7$. We verify our switching concept by calculating the equilibrium response of the switched resonator based on this dielectric function. While the strong screening of the electric field generally reshapes both modes (Figs. 5.1c and d), the impact on the LC mode (Fig. 5.1c) is much stronger as compared to the DP mode (Fig. 5.1d). The shape and amplitude of the near-field distribution E_{x} of the fundamental LC mode at 0.8 THz is drastically changed, since the field enhancement in the gap region disappeared. A line cut across the gap element, displaying the normalized field enhancement of the LC mode (Fig. 5.3a), enables a quantitative view on the reduction of the field enhancement: it is reduced by 95% (black curve compared to red curve). This evidences that the photo-excited plasma in the InGaAs patch strongly screens the electric near field in the gap region, therefore proving the switch-off of the LC mode. Correspondingly, the transmission spectra (Fig. 5.3b) show that the LC mode is completely quenched. For an undoped switching patch ($\rho_{\mathrm{switch}} = 0$, black curve), the LC resonance induces a pronounced transmission

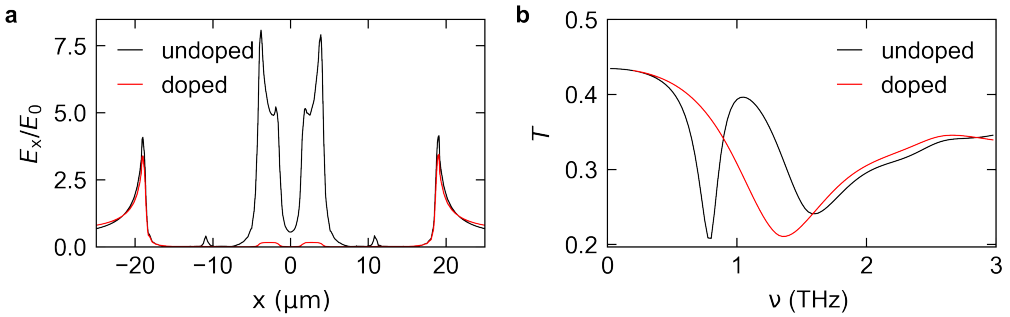

Figure 5.3: Switch-off analysis of photo-switchable resonator MM I. (a) Calculated normalized field enhancement of the LC mode $\frac{E_x}{E_0}$ along y = 0 without (black curve) and with doping of the switching patch (red curve). (b) Calculated transmission spectra for an undoped (black curve) and doped (red curve) switching patch, respectively.

minimum at 0.8 THz. This minimum completely disappears when the switching patch is doped with $\rho_{\text{switch}} = 3.5 \times 10^{18}\,\text{cm}^{-3}$ (red curve). On the other side the DP mode, due to the dipolar character of this mode, is not switched-off: The photo-doped patch induces a slight red-shift of 0.25 THz. This shift is caused by the altered dielectric surrounding and new current paths. To sum up, the presented switching approach allows for selective switching of the LC mode by photo-doping of the switching patch underneath the central gap.

Our switching concept brings the advantage that it can be transferred to any LC-based metamaterial. In the following, this is demonstrated by showing corresponding calculations for metamaterial MM II, with a fundamental resonance frequency of $\nu_{\text{LC}} = 0.5$ THz and a higher order mode at $\nu_{\text{DP}} = 1.8$ THz. Fig. 5.4a and b show the calculated near-field distribution of the LC and the DP mode for an undoped ($\rho_{switch} = 0$) switching patch (marked by dashed lines in Fig. 5.4a). The strongest enhancement is again observed for the LC mode and is thus found in the gap region. Doping the switching patch with a charge carrier density of $\rho_{\text{switch}} = 3.5 \times 10^{18}\,\text{cm}^{-3}$ results in a drastic change of the field enhancement E_x of the LC mode: The field in the gap region disappeared (Fig. 5.4c). The field enhancement of the DP (Fig. 5.4d) mode is also weakened. Fig. 5.4e shows a line cut across the upper gap element to display the normalized field enhancement of the LC mode. The photo-excited plasma in the InGaAs patch strongly screens the electric near field in

the gap region, which results in a reduction of the E-field enhancement by 95% (black curve compared to red curve). This evidences the proof-of-principle of the LC mode's deactivation. This is further illustrated in the comparison of the far-field transmission spectra, shown in Fig. 5.4f. For an undoped switching patch (black curve), the LC resonance induces a pronounced transmission minimum at $\nu_{\mathrm{LC}} = 0.5\,\mathrm{THz}$. Another broader minimum at $\nu_{\mathrm{DP}} = 1.8\,\mathrm{THz}$ is induced by the DP mode. Doping the patch results in the complete disappearance of the LC mode's transmission minimum and a redshift of the DP mode. We therefore developed a second functional switchable resonator. The applied concept of a semiconductor switching patch underneath the gap region can be employed for any LC-based resonator design.

As the switching concept seems promising in the numerical model, we will discuss its experimental realization in the following section.

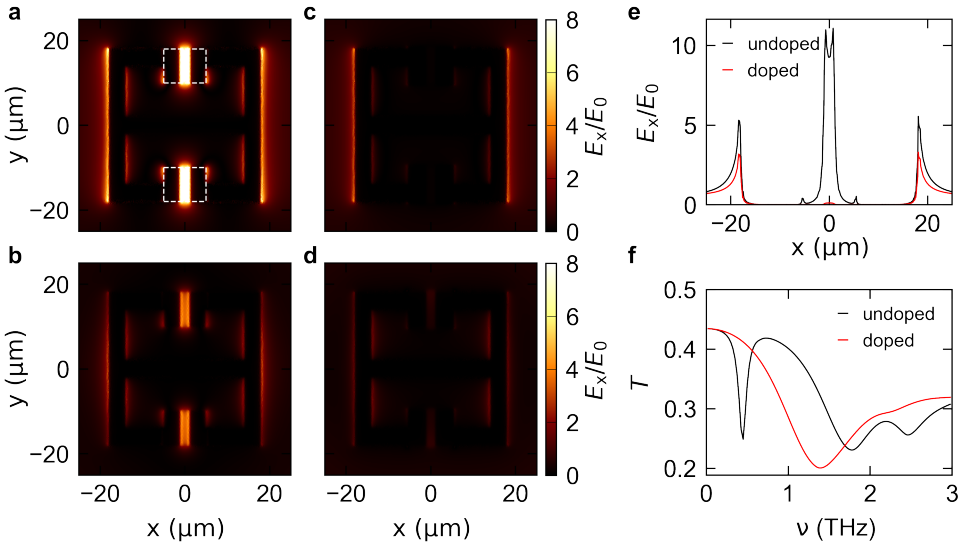

Figure 5.4: Calculated spatial and spectral characteristic of the photo-switchable resonator MM II. (a) Enhancement of the near-field amplitude, E_x, of the fundamental LC mode relative to the far-field amplitude, E_0, at a depth of z = -200 nm, for an undoped switching layer. (b) Corresponding near-field enhancement of the dipolar mode. (c) Near-field enhancement with doped switching layer, for the LC mode, and (d), for the dipolar mode. (e) Normalized field enhancement of the LC mode $\frac{E_x}{E_0}$ along y = 0 without (black curve) and with doping of the switching patch (red curve). (f) Transmission spectra for an undoped (black curve) and doped (red curve) switching patch, respectively.

5.2 Fabrication

We deposit a photo-conduction layer of $In_{0.55}Ga_{0.45}As$, yielding a gap energy of $E_{gap} = 0.73$ eV, by molecular beam epitaxy on a GaAs-substrate or GaAs-heterostructure. For the switching layer of a thickness of 100 nm, a defect-rich growth is desirable, as defects prevent the formation of a highly conductive two-dimensional carrier system and limit the charge carrier lifetime. The short lifetime thus inhibits the build-up of a cyclotron resonance in an external magnetic field, required for the coupling of Landau-quantized electrons. If a CR was to built-up in the photo-excited InGaAs, it would strongly disturb the analysis of our coupled structures. A MBE substrate temperature below 400 K induces such defect-rich growth conditions, while an epitaxial relationship to the underlying GaAs is maintained. To lessen the broadband transmission reduction, caused by the photo-excited charge carriers, and to minimally perturb an underlying matter system the InGaAs layer is chemically wet etched. The patches sized 18 $\times$ 22 μm (4 $\times$ 12 μm for MM II) remain only in the gap-region of the resonator, where the photo-conductivity is crucial for the switch-off of the LC resonance. The alignment of the patches (Fig. 5.5a) with the gap elements and the subsequent structuring of the antennas is done with electron beam lithography. Prior to the deposition of 100 nm Au, 10 nm Ti are deposited for an improved adhesion. Microscopy pictures (Figs. 5.5b and c) show the finished array of photo-switchable resonators MM I and MM II, respectively. In Fig. 5.5d a scanning electron microscope (SEM) of the photo switchable resonator MM I is shown. It is clearly visible, that the gold on top of the InGaAs patches overlaps with the remaining structure, therefore enabling conduction in the

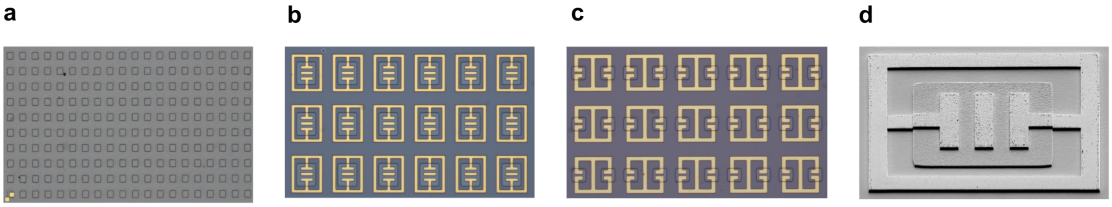

Figure 5.5: Fabrication of photo-switchable resonators. (a) Etched switching patches. Careful alignment of the switching patch and the metal resonators gap element via EBL leads to an array of photo-switchable resonators MM I (b) and MM II (c). (d) SEM picture of photo-switchable resonator MM I. Pictures taken by V. Zeller.

metal part of the resonator. As a last step, the GaAs substrate has been polished down to a thickness of approximately 40 µm in order to prevent spurious signals from two-photon absorption. To test the switching functionally, we fabricate arrays consisting of 40×40 resonators (MM I) onto a bulk GaAs substrate.

5.3 Switching dynamics of the photo-switchable resonator

The relevant dynamics concerning the photo-switchable resonator are studied in a femtosecond setup (see Chapter 3.4), which is provided by the AG Huber. We first examine the switching dynamics of an InGaAs-layer and investigate the effects of strong, femtosecond excitation of the semiconductor layer. We photo-excite the MBE-grown InGaAs by the NIR switching pulse with an intensity of $2\,\mathrm{GW/cm^2}$, resulting in a photo-excited electron density of $\rho_{\mathrm{switch}} = 3.5 \times 10^{18}\mathrm{cm}^{-3}$ in the layer. The resulting plasma frequency of this Drude plasma is $\nu_{\mathrm{p}} > 80\,\mathrm{THz}$. Therefore, the plasma is expected to screen the THz-pulse, comprising only frequency components below 3 THz. Coulomb screening is expected to emerge on a timescale comparable to the inverse plasma frequency [131].
We determine the response of the InGaAs layer during excitation by detecting the transmitted THz signal in dependence of the pump-THz delay t_{D} (Fig. 5.6a). Pumping the layer at $t_{\mathrm{D}} = 0\,\mathrm{ps}$ clearly leads to an instant response of the transmitted signal, which we attribute to the successful photo-injection of charge carriers. The pump-probe THz field reveals the diagonal structure along $t = -t_{\mathrm{D}}$ resulting from the abrupt increase of the conductivity of the InGaAs layer. Yet, it only appears in a narrowly confined temporal window around the switching time. Correspondingly, the transmission spectra, obtained by Fourier transformation of the time domain data in the τ-frame (for details see Chapter 3), show a uniform decrease (Fig. 5.6b). The charge carrier plasma screens the THz-pulse, reducing its transmission as ν_{p} is much larger than the frequency components of the THz pulses. Fig. 5.6c shows the differential transmission at the resonance frequency of the photo-switchable resonator MM I. The transmission strongly decreases for $\tau > 0\,\mathrm{ps}$.
Having demonstrated the injection of photo-carriers into the InGaAs switching structure, we now experimentally test our numerical FEFD predictions by photo-exciting an array

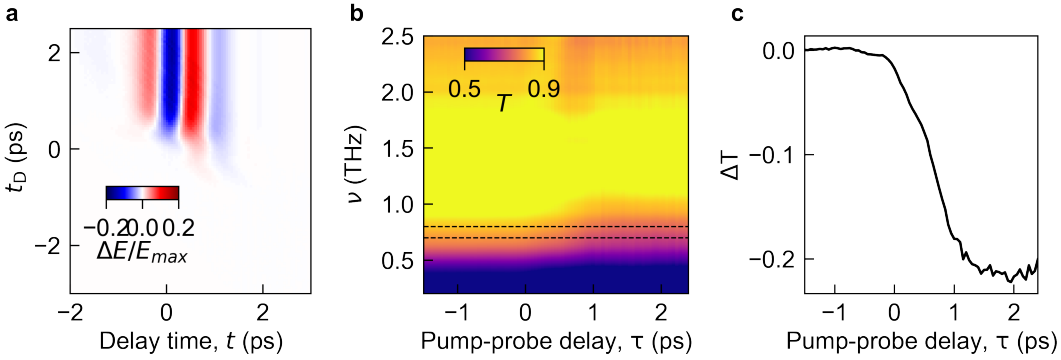

Figure 5.6: Switching dynamics of the InGaAs layer. The structure consists of a quantum well stack with an $In_{0.55}Ga_{0.45}As$ (E_{gap} = 0.73 eV) switching layer of a thickness of 100 nm. The GaAs substrate is polished down to a thickness of 40 μm in order to prevent spurious signals from two-photon absorption. (a) Systematic scan of the electric field of the transmitted THz transient varying the pump-THz delay, t_D. The charge carrier density resulting from femtosecond photo-excitation is 3.5×10^{18} cm^{-3}. (b) Corresponding transmission spectra, in the τ-frame. (c) Differential transmission extracted within the spectral window highlighted in panel (b) by dashed lines.

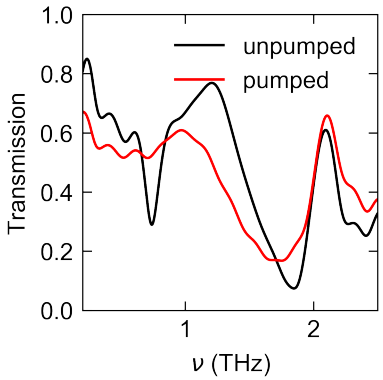

Figure 5.7: Quasi-steady state measurement of photo-switchable resonator MM I. Transmission spectrum of an unpumped structure (black curve) shows a distinct, narrow LC mode at 0.75 THz and a DP mode at 1.8 THz. 2 ps after pumping the structure the LC mode is extinct and the DP mode redshifted and slightly broadened.

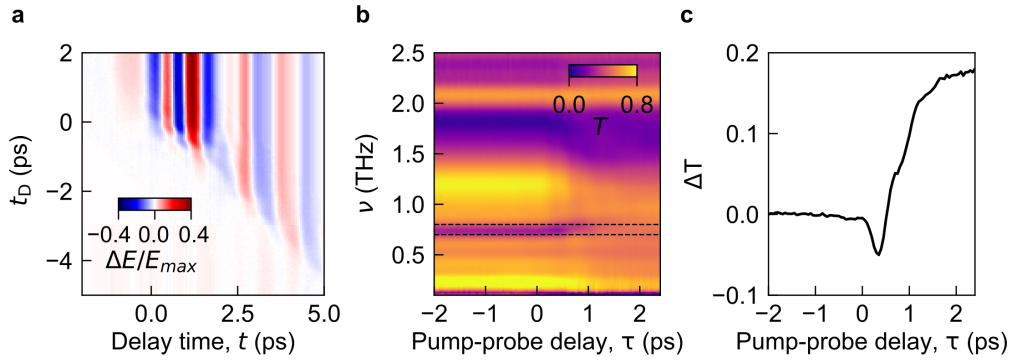

Figure 5.8: Switching dynamics of the uncoupled resonator MM I. (a) Pump-probe THz signal during femtosecond photo-excitation. The resulting charge carrier concentration is $3.5 \times 10^{18}\text{cm}^{-3}$. (b) Corresponding transmission spectra in the τ-frame reveal the switch-off of the LC resonance (at 0.75 THz) after photo-doping the InGaAs patch at $\tau = 0$ ps. The redshift and broadening of the DP mode (at 1.8 THz) is also clearly visible. (c) Differential transmission of the LC mode extracted within the frequency window outlined in panel (b) by dashed black lines. After a first dip in the transmission, there is a steep increase resulting in steady state value of the extinct LC mode.

of photo-switchable resonators of type I. We compare the transmission spectra before the switching, where the LC mode is clearly visible at 0.75 THz (Fig. 5.7, black curve), and after the switching ($t_D = 2$ ps; Fig. 5.7, red curve). Indeed, 2 ps after switching, the strongly altered dielectric function of the InGaAs patch leads to a total quench of the LC mode (red curve at $\nu = 0.75$ THz) and to a redshift with slight broadening of the DP mode (red curve $\nu > 1.5$ THz). The rest of the transmission spectrum is only weakly affected, showing that, as intended, the InGaAs patches only induce a weak broadband reduction of the transmitted THz field. These spectra thus demonstrate a successful experimental switch-off of the LC resonance by photo-excitation of the InGaAs patch located in the capacitive region of a metamaterial resonator.

To go beyond the steady-state setting and to get insight into the dynamics, we now perform a systematic scan of the transmitted signal as a function of t_D (Fig. 5.8a). Here, the pump-probe THz field shows a slightly more complex structure near the diagonal as compared to the unstructured InGaAs layer. This is caused by the deactivation of the narrow band LC-resonance. Fig. 5.8b shows the spectrally resolved transmission, $T(\nu, \tau)$.

For $\tau < 0$ ps, the LC mode is clearly visible as a transmission minimum at $\nu = 0.75$ THz. The DP mode at $\nu = 1.8$ THz lies far above the LC resonance. Exciting the InGaAs patch at $\tau = 0$ ps leads to a strong variation of the transmitted THz-field at the resonance frequency of the fundamental LC mode: The LC mode slightly blue shifts and then fades away on a sub-picosecond time scale. After $\tau = 2$ ps, the quasi-steady state setting, where the LC mode is deactivated, has been reached. The higher order DP mode, on the other hand, shifts to lower frequencies, confirming our calculations (see Fig. 5.3b). Besides the broadening of the DP mode, its oscillator strength also becomes slightly weaker. The transmission spectra demonstrate the spectral selectivity of the switching, which affects mostly the narrowband range of the fundamental mode of the resonator at 0.75 THz and the more broadband mode at $\nu = 1.8$ THz. To quantify the ultrafast switch-off time, we examine the change of the transmission (ΔT) at the frequency of the LC resonance (Fig. 5.8c). After an initial reduction of the transmission, attributed to the redshift of the DP mode, the switching dynamics progresses monotonically, leading to an overall increase of the transmission after switching.

To sum up, we have demonstrated subcycle manipulation of the fundamental resonator mode: The switch-off of the LC mode is much faster than one cycle of the LC resonance, $T_{LC} = 1/\nu_{LC} = 1.33$ ps. This demonstrates the functionality of our ultrafast optically switchable THz metamaterials, suitable for the non-adiabatic modulation of light-matter coupling in GaAs-based heterostructures.

6 Extremely non-adiabatic switching of deep-strong light-matter coupling

Our samples are designed to lead to deep-strong coupling, while also allowing switching. The central gap region of the metamaterial defines the essential region for the envisaged physical interaction: Here, the overlap of the fundamental cavity LC mode with polarization field of the CR in the QW plane is largest, due to the high field confinement provided by the resonator. At the same time, integrating a switching patch here, as presented in Chapter 5 should allow to switch-off the fundamental LC mode, drastically changing the near-field within this region of maximal overlap. This promises a strong impact on the coupling strength characterized by Ω_R. We expect to quench Ω_R within the switch-off time of our subcycle switchable resonator. In the following, we combine our AlGaAs/GaAs QWs (see Chapter 4.1) with photo-switchable metamaterials by growing a defect-rich $In_{0.55}Ga_{0.45}As$-alloy on top of the heterostructures and further process the metamaterial as described in Chapter 5.2. These structures are studied in the cutting edge femtosecond THz-spectroscopy setup provided by the AG Huber.

6.1 Quasi-steady state transmission

To test our switching concept, we start with a threefold QW structure (*Sample A*) with $\rho_{2DEG,total} = 3 \times 1.75 \times 10^{12} cm^{-2}$ electrons and covered with a 2×2 mm array of switchable resonator MM I, with $\nu_{LC} = \nu_0 = 0.8$ THz. Fig. 6.1a shows the corresponding transmission spectra of as a function of ν_c of this coupled system. The polariton dispersion can be

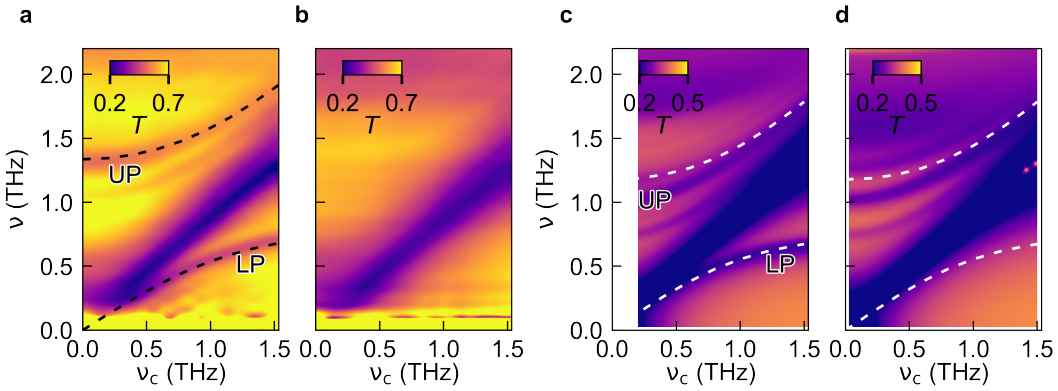

Figure 6.1: Quasi-steady state transmission of *Sample A*. (a) Spectra of the 3-QW structure as a function of the CR. The black dashed lines mark the polaritons. A Hopfield fit yields a coupling strength of $\frac{\Omega_R}{\omega_0} = 0.57$. (b) 2 ps after photo-excitation ($t_D = 2$ ps), the polariton resonances are absent and only the CR remains. (c)-(d) Corresponding numerical calculations with undoped and doped switching patch (white dashed lines indicate the polaritons). The LP polariton vanishes, but there are still resonances coupled to higher order modes, that remain nearly unchanged.

traced following their individual transmission minima: The lower polariton (LP) starts to deviate from the cyclotron transition and merges into the metamaterial resonance at $\nu_0 = 0.8$ THz, for large ν_c. The upper polariton (UP) on the other hand starts at 1.35 THz for $\nu_c = 0$ THz and has an opposite curvature bending upwards. At resonance, at $\nu_c = \nu_0$, the typical anti-crossing signature is observed, displaying the minimal spectral separation of LP and UP of 1.01 THz at the frequencies $\nu_{LP} = 0.48$ THz and $\nu_{UP} = 1.49$ THz. The bare CR at ν_c, which originates from uncoupled areas of the sample, is visible as a prominent transmission minimum. The Hopfield fit (black dashed lines) of the new eigenstates yields a coupling strength of $\frac{\Omega_R}{\omega_0} = 0.57$, placing the structure in the ultrastrong coupling regime. We now excite the structure by a near-infrared switching pulse (Fig. 3.4, red pulse) of a duration of 70 fs (Fig. 3.3) and probe the transmitted THz field to characterize the impact of the switching pulse on the coupling strength. The switching pulse, chosen to arrive before the THz probe pulse at $t_D = 2$ ps, prepares a photo-carrier concentration of 3.5×10^{18} cm^{-3}, which renders the switching patch quasi-metallic, effectively extinguishing the LC mode. The transmission spectra (Fig. 6.1b) of the switched structure are fundamentally altered:

both polariton resonances have clearly disappeared. This absence of the polaritons evidences a successful deactivation of the ultrastrong coupling, consequently setting Ω_R to zero after switching. Moreover, the transmission spectra show that the switching dominantly affects the narrow spectral range in which the polariton resonances are located: the bare CR is left nearly unaffected. We thus demonstrated a high selectivity of our switching process, as a consequence of only affecting the region of maximal near-field enhancement. Note that, above $\nu = 1.6\,\mathrm{THz}$, there is a decrease in transmission, which we attribute to the red-shift of the dipolar mode (DP), which is only off-resonantly coupled to the CR. This red-shift has already been observed for the uncoupled resonator (see Chapter 5.3), and is originating in the changed dielectric environment caused by the photo-excited carriers.

We compare our experimental observations to numerical calculations, combining the switchable resonator (see Chapter 5.1) and ultrastrongly coupled structures, based on the used heterostructure (see Chapter 2.4.3). The numerically calculated complex field distribution and transmission spectra, for a coupled undoped resonator array (Fig. 6.1c), shows distinct polariton resonances. The LP is clearly distinguishable below the CR at ν_c. There are multiple resonances in the vicinity of the UP. The system forms these multiple coupled resonances in a setting where Ω_R becomes close to ω_0. In this regime the concept of a single resonator mode interacting with a single electronic excitation begins to falter and a corresponding treatment beyond the usually employed two-mode model is required. A framework to describe the appearance of these modes is currently developed in our group. For the present study, which focusses on the switch-off of the coupling strength between the fundamental LC mode and the electronic excitation, the formation of these higher order modes is of limited importance. We therefore apply the usual two-mode Hopfield model, but take only the LP into account. The resulting dispersion of LP and UP are marked with white dashed lines in Fig. 6.1c. An additional analysis of the mode profiles (see Chapter 2.4.3) confirms the fitted UP dispersion, starting at $\nu_{UP}(\nu_c = 0) = 1.2\,\mathrm{THz}$.

Then doping the switching patch underneath the gap region of the resonator with a density of $\rho_{switch} = 3.5 \times 10^{18}\,\mathrm{cm}^{-3}$ to simulate the effect of a switching pulse, results in the transmission spectra shown in Fig. 6.1d. Screening of the LC mode quenches Ω_R, therefore ultrastrongly coupled polaritons of the LC mode do not form. This is clearly seen in the absence of the LP, in contrast to Fig. 6.1c. The mode which we have identified as the UP in Fig. 6.1c has also vanished. However, the change is less obvious in the false colour

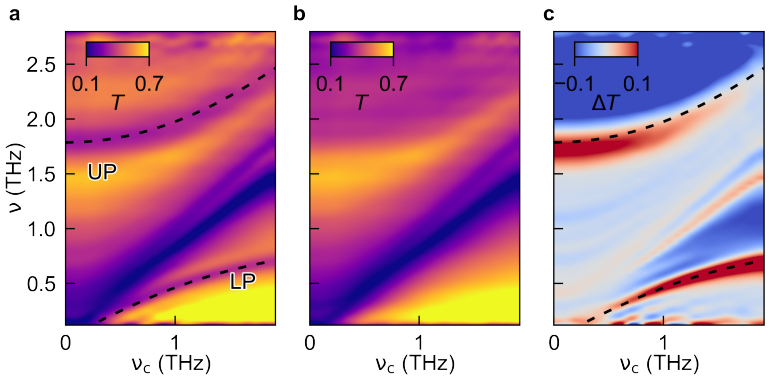

Figure 6.2: Quasi-equilibrium transmission of *Sample B*. Transmission spectra of the 6-QW structure coupled to the photo-switchable resonator MM I as a function of ν_c. (a) The polariton dispersions are clearly visible for the unswitched structure ($T_{t_D \ll 0\,\mathrm{ps}}(\nu, \nu_c)$). A Hopfield-Fit yields a coupling strength of $\frac{\Omega_R}{\omega_0} = 0.8$, the corresponding polaritons are marked by dashed lines. (b) 2 ps after photo-excitation ($T_{t_D=2\,\mathrm{ps}}(\nu, \nu_c)$), the polariton resonances are absent and only the CR remains. (c) The differential transmission ΔT shows the selectivity of the switching, almost exclusively affecting the polariton resonances (dashed lines).

presentation. As the higher-order modes do not originate in the LC mode, according to our analysis of the mode profiles, they are less strongly affected by the switching pulse and therefore remain nearly unaltered in Fig. 6.1d. This observation, also strengthens the single resonator mode coupling ansatz, which we use in the Hopfield model. As the origin of these multiple resonances is not fully understood yet, the interpretation of ultrastrongly coupled structures is more complicated. However, the presented calculations indicate that the higher order resonances do not originate in the coupling of the CR to the DP mode. We conclude that, since the DP mode is expected to red-shift, for an activated switching patch and these modes do not shift spectrally. Based on the observation of the disappearance of polariton resonances in quasi-steady state transmission spectra, and confirmed by numerical calculations, we thus have evidenced the successful deactivation of ultrastrong coupling.
In a next step, we increase the coupling strength, by using a sixfold QW stack with again $\rho_{2\mathrm{DEG}} = 1.75 \times 10^{12}\mathrm{cm}^{-2}$ per QW. The total carrier density of this structure (*Sample B*) therefore doubled with respect to *Sample A*. The near-field of photo-switchable resonator MM I was used again, to dress the electrons in the QWs. In Fig. 6.2a the transmission spectra of *Sample B* are shown. Before photo-excitation, the transmission spectra $T_0(\nu, \nu_c)$

show a well-defined, narrow-band lower polariton resonance with a frequency of ν_{LP} = 0.42 THz at the anti-crossing point ν_c = 0.8 THz. The frequency of the UP at the ACP is ν_{UP} = 1.8 THz. We quantify the coupling strength by diagonalizing the light-matter coupling Hamiltonian: the best fit to these polariton features yields $\frac{\Omega_R}{\omega_0} = 0.8$ (dashed black curves). Thus doubling the coupling number of coupled oscillators compared to *Sample A* and therefore increasing the normalized coupling strength by a factor $\sqrt{2}$, puts us in the vicinity of the deep-strong coupling regime marked by $\frac{\Omega_R}{\omega_0} > 1$.

To study the switch-off, we again pump the structure, and record the distinctly altered quasi-steady state transmission spectra, $T_{t_D=2\,ps}(\nu, \nu_c)$ (Fig. 6.2), 2 ps after photo-excitation of switch element. It can be seen, that the strong reshaping of the LC mode completely removes the transmission minima of the LP across the entire range of ν_c, evidencing a full collapse of the coupling strength. The interpretation of the spectra regarding the UP is even harder then for *Sample A*, as a new broadband resonance with a similar curvature as the UP appears above 1.8 THz. We attribute this new mode to the red-shifted DP mode, which couples off-resonantly to the CR. In order to interpret the effects of the switching on the UP, we analyse the differential transmission $\Delta T = T_{t_D=2\,ps}(\nu, \nu_c) - T_{t_D\ll 0\,ps}(\nu, \nu_c)$ (Fig. 6.2c), with the transmission of the unpumped sample $T_{t_D\ll 0\,ps}(\nu, \nu_c)$. As expected, at the polariton frequencies (marked by dashed lines) there is an increased differential transmission (red area in Fig. 6.2c). This evidences the disappearance of the polaritons, which manifest in absorption peaks in $T_{t_D\ll 0}(\nu, \nu_c)$. Visualizing the changes in this manner does not only show the extinction of the LC, but also of the UP. It also underlines the selectivity of our switching concept, as effects are visible almost exclusively at the polariton resonance frequencies. We were able to successfully couple the switchable resonator MM I to different quantum well stacks and demonstrated the deactivation of the coupling strength of up to $\frac{\Omega_R}{\omega_0} = 0.8$.

To further increase the normalized coupling strength, we decided to use the second switchable resonator MM II (see Chapter 5.1). This resonator comprises a lower resonance frequency (ν_{LC} = 0.5) and a higher vacuum mode confinement, and therefore allows for higher coupling strengths compared to MM I. However, due to limitations of detection in our THz-spectroscopy setup for frequency below $\nu \approx 0.25$ THz, the transmission spectra of samples with this resonator are more difficult to analyse. Despite this limitation, we couple the sixfold QW stack to the photo-switchable resonator MM II and record

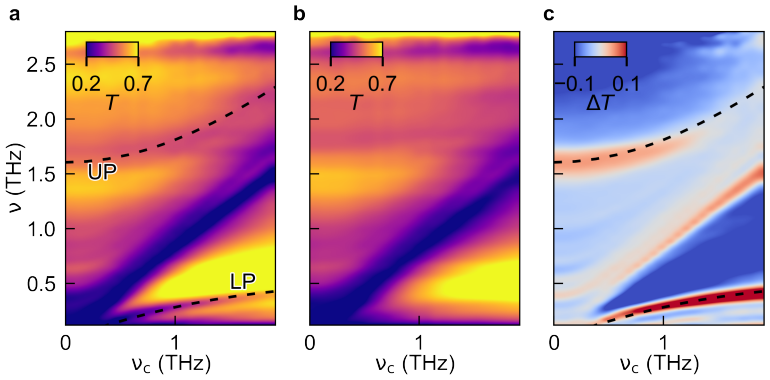

Figure 6.3: Quasi-steady state transmission of *Sample C*. Transmission spectra of the 6-QW structure coupled to the photo-switchable resonator MM II as a function of ν_c. (a) $T_{t_D \ll 0}(\nu, \nu_c)$: The dispersion of the LP is clearly visible for the unswitched structure. The UP is only weakly recognisable. A Hopfield fit yields, taking only the LP into account, a coupling strength of $\frac{\Omega_R}{\omega_0} = 1.3$. (b) $T_{t_D=2\,ps}(\nu, \nu_c)$ Switching the structure 2 ps before the THz probe pulse arrives, leads to the disappearance of the LP. In order to visualize the effect of the switching better ΔT is shown in (c). The LP and UP are now clearly discernable as increased differential transmission. The polariton dispersions are indicated by dashed lines.

the transmission as a function of ν_c before switching (Fig. 6.3a). The LP dispersion is clearly visible, indicated by dashed lines. We attribute the broadband local transmission minimum at $\nu = 1.5$ - $2.0\,THz$ for $\nu_c = 0\,THz$ to the UP, superposed with an uncoupled higher order resonance. Using the Hopfield fitting procedure, but only taking the LP into account, leads to a coupling strength of $\frac{\Omega_R}{\omega_0} = 1.3$. The corresponding UP dispersion is marked by a dashed line in Fig. 6.3a. With a relative coupling strength of $\frac{\Omega_R}{\omega_0} = 1.3$, we enter the deep-strong coupling regime, where the virtual photon population of the ground state is strongly enhanced. We now deactivate the coupling by femtosecond excitation of the switchable resonator. The quasi-equilibrium transmission after $t_D = 2\,ps$ shows again the collapse of light-matter coupling: The LP and the UP have completely vanished (Fig. 6.3b). This becomes particularly apparent in the differential transmission data $\Delta T = T_{t_D=2\,ps}(\nu, \nu_c) - T_{t_D \ll 0\,ps}(\nu, \nu_c)$ shown in Fig. 6.3c. The increase in transmission unambiguously corresponds to the cavity polariton frequencies (dashed lines mark the dispersions yielded by the Hopfield fit), thus confirming the coupling strength and the first-ever optically induced collapse of deep-strong light-matter coupling. Non-adiabatically

deactivating the coupling strength of a structure characterized by $\frac{\Omega_R}{\omega_0} = 1.3$ is expected to release 0.32 virtual photons per resonator (see Chapter 2.2). We therefore next investigate the switch-off time and dynamics of our light-matter coupled systems.

6.2 Time dependent measurements

Having demonstrated deep-strong coupling to our photo-switchable metamaterials and their switch-off in a quasi-steady state setting, we now go beyond and analyse the subcycle dynamics of the coupled structures. To build a foundation for understanding the dynamics of light-matter decoupling, we start with *Sample A* characterized by a coupling strength of $\frac{\Omega_R}{\omega_0} = 0.57$. At the anti-crossing point, where the coupling is strongest, both polaritons of this sample are located in our detectable frequency range. Therefore *Sample A* is a good candidate to investigate light-matter decoupling, by measuring the instantaneous THz response during the switch-off. The following experimental data are obtained at the anti-crossing point ($\nu_c = \nu_0$). As already discussed in Chapter 3.4, the THz-pump and NIR switching pulses are shifted with respect to each other by the delay time t_D. Electro-optic detection is performed at a delay time t relative to the transmitted THz pulse (Fig. 6.4a, black curve). Photo-excitation at $t_D = 0$ ps leads quasi-instantly to a strong pump-induced change $\Delta E(t)$. The red curve in Fig. 6.4a displays this change fivefold increased for better visibility. Initially, the amplitude of $\Delta E(t)$ remains small, but for larger delay times t it becomes comparable to the oscillations of the transient through the unswitched sample. This indicates that the switching has no broadband effect, but is selectively suppressing only the narrow-band polaritons.

A systematic scan of the transmitted THz probe pulse as a function of t_D allows for the determination of the dynamics of light-matter deactivation: In Fig. 6.4b, showing $\Delta E(t, t_D)$, the abrupt disruption of the polariton oscillations through the switching pulse is depicted. The transition from the coupled to the uncoupled state does not proceed smoothly, but with visible wiggles ($t_D < 0$ ps and $t > 2$ ps). To better understand this transition we perform a numerical transformation from the t_D to the τ-frame, with $\tau = t_D + t$ (see Chapter 3). Fourier transforming in this time frame allows for the exploration of the response function of the system with spectral resolution. The evolution of the transmission ($T(\nu, \tau)$) of *Sample A* (Fig. 6.5a) tracks the transition from the light-matter coupled state

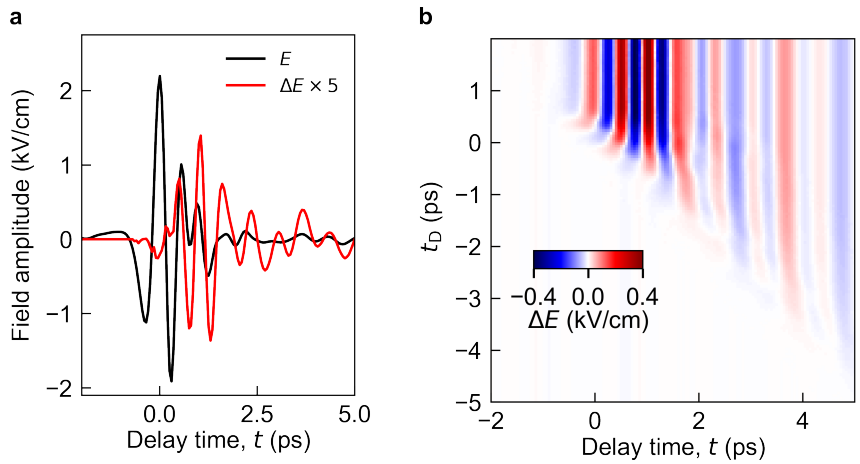

Figure 6.4: t_D-dependent measurements of *Sample A*. (a) Transmitted THz transient before excitation (black curve), and pump-probe signal ΔE for $t_D = 0\,ps$ (red curve). (b) ΔE as a function of the EOS delay time, t, and the pump-probe delay time, t_D.

($\tau < 0$ ps) to the decoupled state. For $\tau < 0$ both polaritons at $\nu_{LP} = 0.47$ THz and $\nu_{UP} = 1.49$ THz respectively, can be clearly identified (marked by dashed lines in Fig. 6.5a). They both disappear for $\tau > 0$ ps, while other spectral components remain unaffected. For a more detailed view, the curves in Figs. 6.5b and c line out the transmission change $\Delta T = T(\nu, \tau) - T(\nu, -1\,\text{ps})$ at the UP and LP frequencies individually. The differential transmission at the UP frequency increases at delay times $\tau < 0$ ps, shorty before decreasing below T_0. This is followed by a steep increase which levels when reaching its final value (Fig. 6.5b). At the LP frequency, ΔT displays a short-lived increase for $\tau < 0$ ps, reaches its minimum value near 0 ps and then steeply increases until reaching its final value (Fig.6.5c). The transmission increase is accompanied by oscillatory features, which we will discuss in detail in Chapter 6.4.

Having studied the decoupling of an ultrastrongly coupled system, we built the bases for the investigation of deactivation dynamics in deep-strong coupling regime. Therefore, we study the switch-off dynamics of *Sample C*, with a coupling strength of $\frac{\Omega_R}{\omega_0} = 1.3$. The measurement of the transmission as a function of τ is displayed in Fig. 6.6. The LP is visible for $\tau < 0$ ps lying at $\nu_{LP} = 0.2$ THz. The UP, on the other hand, is owing to the

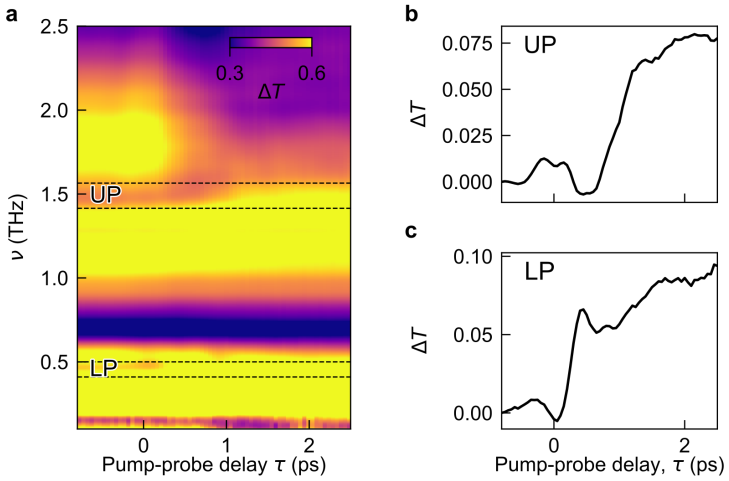

Figure 6.5: τ-dependent transmission of *Sample A*. (a) Transmission spectra obtained by Fourier transformation of the t_D-dependent data along lines of constant τ. The dashed lines indicate the polariton resonances centred at a frequency of 0.48 THz and 1.49 THz, respectively. Change of the transmission ΔT at (b) the UP and (c) the LP resonance frequency indicated in (a).

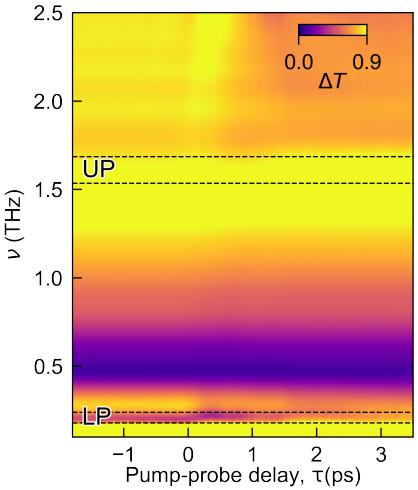

Figure 6.6: τ-dependent transmission of *Sample C*. Transmission of spectra obtained by Fourier transformation of the τ-dependent transmitted waveforms. The dashed lines indicate the polariton resonances centred at a frequency of 0.2 THz and 1.6 THz, respectively.

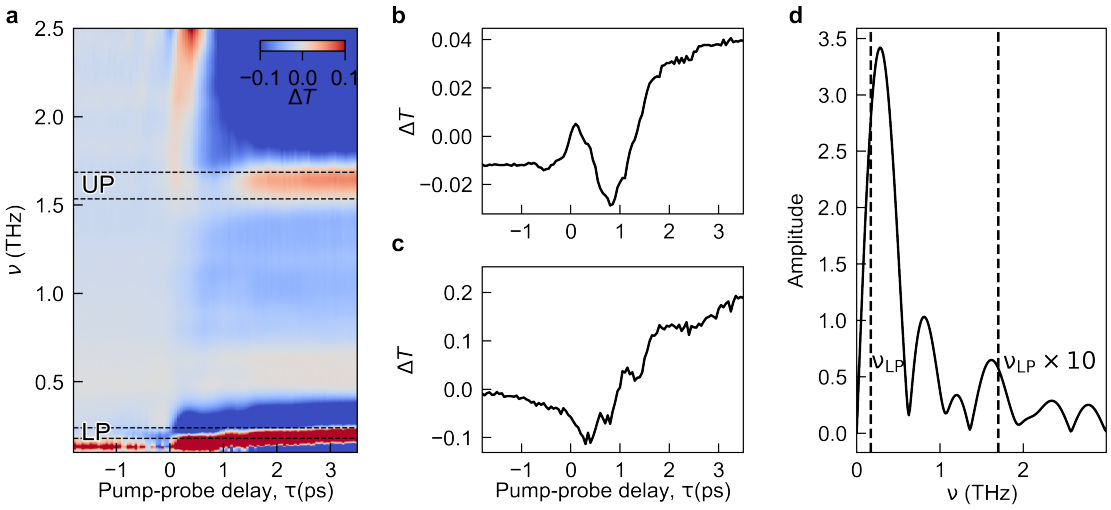

Figure 6.7: τ-dependent transmission of *Sample C*. (a) Differential transmission $\Delta T(\nu, \tau) = T(\nu, \tau) - T(\nu, -1.8\,\text{ps})$. The dashed lines indicate the polariton resonances centred at a frequency of 0.2 THz and 1.6 THz, respectively. (b)-(c) change of the transmission ΔT at the UP and LP frequency indicated in (a). (d) Spectrum of the switching dynamics of the LP. Vertical dashed lines indicate the resonance frequency of the LP, ν_{LP}, and $10 \times \nu_{\text{LP}}$, for reference.

false colour plot, not discernable. Dashed lines mark the frequency range of the UP at $\nu_{\mathrm{UP}} = 1.6\,\mathrm{THz}$. To better identify the changes caused by the NIR switching pump pulse, the differential transmission $\Delta T(\nu, \tau) = T(\nu, \tau) - T(\nu, -1.8\,\mathrm{ps})$ is show in Fig. 6.7a. Here, the increased transmission after switching is clearly attributed to the LP and UP. The differential transmission at ν_{UP} (Fig. 6.7b) displays a short-lived increase, which reverses to a decrease, until reaching its lowest value at about $\tau = 0\,\mathrm{ps}$. Then, a subsequent steep increase is followed by a flattening of ΔT as it reaches its final value. This progression is similar to the one observed in *Sample A*. The change in transmission at ν_{LP} (Fig. 6.7c), on the other hand, differs from the one observed in *Sample A*. Even tough there is an initial decrease, followed by an increase of ΔT, the increase is more strongly structured by oscillatory features. A Fourier analysis of these oscillations, after applying a low-pass filter with a cut-off frequency of 2.5 THz to reduce artefacts from noise, is shown in Fig. 6.7d. The dominating low frequency component is attributed to the increasing transmission. But, there are components at 0.85 THz and 1.7 THz, which correspond to the observed oscillations. The frequencies of these sub-polariton-cycle oscillations are almost ten times higher than the LP resonance frequency $\nu_{\mathrm{LP}} = 0.2\,\mathrm{THz}$. These rapid oscillations seem to be a fingerprint of the ultrafast deactivation of deep-strong coupling and need to be further investigated. We therefore developed a theory to generally understand the oscillatory signatures of deep-strong coupling during switch-off and provide quantitative results. This model should also get us new insight into the physics happening during switch-off. The model and arising predictions are presented in the following.

6.3 Time dependent quantum model

To theoretically investigate the decoupling dynamics of our structures, we develop a theory which implements light-matter coupling and subcycle control of the system. Our mean-field model amounts for the extremely high coupling in our systems, by including anti-resonant interaction terms and the diamagnetic term of the light-matter interaction Hamiltonian. The mean-field approach enables the determination of the polarization dynamics by solving Heisenberg's equation of motion for the expectation values of the operators. The switching process is implemented by a time dependent vacuum Rabi frequency. Moreover, to describe specifically our system, we not only included the coupling of Landau-quantized

electrons and the LC mode, but also the DP mode and its switching dynamics. Hence, our theory models the coherent spectroscopy we perform in our experiments, allowing us to directly compare experimental and calculated data and thus understand the physics of decoupling.

6.3.1 Equation of motion

To describe light-matter interaction of our system, we start with eq. 2.3 the interaction Hamiltonian (see Chapter 2.1) and expand it by $\hat{H}_{\text{ext}}$ to account for the coupling to the external field. We then get:

$$\hat{H} = \hat{H}_{\text{cavity}} + \hat{H}_{\text{Landau}} + \hat{H}_{\text{int}} + \hat{H}_{\text{dia}} + \hat{H}_{\text{ext}}. \tag{6.1}$$

$\hat{H}_{\text{cavity}}$ also assumes a different form than in eq. 2.4, as is now implements mulitmode coupling:

$$\hat{H}_{\text{cavity}} = \sum \hbar\omega_{\text{j}} \hat{a}_{\text{j}}^{\dagger} \hat{a}_{\text{j}}, \tag{6.2}$$

with the cavity bosonic operators $\hat{a}_{\text{j}}^{\dagger}$ and $\hat{a}_{\text{j}}$ with j = {LC, DP} of the LC and DP mode. Our study showed, that in our structure the coupling of the Landau electrons to the DP mode is negligibly small ($\Omega_{\text{R,DP}} \rightarrow 0$), so in the following we dispense from including its coupling terms in the Hamiltonian. With $\hat{H}_{\text{Landau}} = \hbar\omega_{\text{c}} \hat{b}^{\dagger}\hat{b}$, $\hat{H}_{\text{int}} = \hbar\Omega_{\text{R}} \left(\hat{a}_{\text{LC}} + \hat{a}_{\text{LC}}^{\dagger}\right)\left(\hat{b} + \hat{b}^{\dagger}\right)$ and $\hat{H}_{\text{dia}} = \hbar D \left(\hat{a}_{\text{LC}} + \hat{a}_{\text{LC}}^{\dagger}\right)^2$, the Heisenberg relation to determine the equations of motion for the cavity operators $\hat{a}_{\text{LC}}$ and $\hat{a}_{\text{DP}}$ and for the matter operator $\hat{b}$ can be applied. For each operator $\hat{A}$ the relation

$$\frac{d\hat{A}}{dt} = -\frac{i}{\hbar}\left[\hat{A}(t), \hat{H}\right]$$

delivers the equation of motion, solving the commutator:

$$\frac{d\hat{a}_{\text{LC}}}{dt} = -i\omega_{\text{LC}}\hat{a}_{\text{LC}} - i\Omega_{\text{R}}\left(\hat{b}(t) + \hat{b}^{\dagger}(t)\right) - i2D\left(\hat{a}_{\text{LC}} + \hat{a}_{\text{LC}}^{\dagger}\right) - \frac{i}{\hbar}\left[\hat{a}_{\text{LC}}(t), \hat{H}_{\text{ext}}\right], \tag{6.3}$$

$$\frac{d\hat{a}_{\text{DP}}}{dt} = -i\omega_{\text{DP}}\hat{a}_{\text{DP}} - \frac{i}{\hbar}\left[\hat{a}_{\text{DP}}(t), \hat{H}_{\text{ext}}\right], \tag{6.4}$$

and

$$\frac{d\hat{b}}{dt} = -i\omega_c\hat{b} - i\Omega_R\left(\hat{a}_{LC}(t) + \hat{a}^{\dagger}_{LC}(t)\right) - \frac{i}{\hbar}\left[\hat{b}(t), \hat{H}_{ext}\right]. \tag{6.5}$$

The coupling to the external field through $\hat{H}_{ext}$ is responsible for a driving term as well as fluctuations and dissipation. Therefore $\left[\hat{a}_j(t), \hat{H}_{ext}\right]$ is written as $-\gamma_j\hat{a}_j(t) + \hat{F}(t)$, with the cavity mode's damping γ_j and the force operator $\hat{F}(t)$. The same considerations apply for the matter operator.

An expectation value mean-field treatment, where we set $\left\langle\hat{a}_j\right\rangle = \alpha_j$ and $\left\langle\hat{b}\right\rangle = \beta$, facilitates the further procedure. As the external field only drives the cavity mode, the mean-field value of the driving force operator $\left\langle\hat{F}(t)\right\rangle$ is the external THz-field $E_{ext}(t)$ for the cavity modes and $\left\langle\hat{F}(t)\right\rangle = 0$ for the matter. We now derive the subcycle dynamics of the cavity and matter fields by the resulting equations of motion in the mean-field approach:

$$\frac{d\alpha_{LC}}{dt} = (-i\omega_{LC} - \gamma_{LC})\,\alpha_{LC} - i\Omega_R\left[\beta(t) + \beta^*(t)\right] - 2iD\left[\alpha_{LC}(t) + \alpha^*_{LC}(t)\right] + \kappa_{LC}E_{ext}(t), \tag{6.6}$$

$$\frac{d\alpha_{DP}}{dt} = (-i\omega_{DP} - \gamma_{DP})\,\alpha_{DP} + \kappa_{DP}E_{ext}(t) \tag{6.7}$$

and

$$\frac{d\beta}{dt} = (-i\omega_c - \gamma_c)\,\beta - i\Omega_R\left[\alpha_{LC}(t) + \alpha^*_{LC}(t)\right]. \tag{6.8}$$

The coupling of the cavity modes to the external field is scaled by κ_j. This set of coupled differential equations models the response of our structure for fixed parameters of the cavity and matter modes. It contains both resonant terms as well as anti-resonant contributions. To implement the decoupling mechanism, we chose to set the cavity parameters (ω_j, γ_j and κ_j) and Ω_R to be time dependent: $\omega_j \rightarrow \omega_j(t + t_D)$, $\gamma_j \rightarrow \omega_j(t + t_D)$, $\kappa_j \rightarrow \kappa_j(t + t_D)$ and $\Omega_R \rightarrow \Omega_R(t + t_D)$. These parameters, X, transit from their initial value X^i to their final value X^f proportionally to the rate of charge carrier generation through the switching pulse. As the temporal shape of the experimental pulse is Gaussian we get:

$$X(t + t_D) = X^i + \frac{X^f - X^i}{2}\left(1 + \frac{2}{\sqrt{\pi}}\int_0^{t+t_D} e^{-\left(\frac{\sqrt{4ln2}}{\tau_{switch}}(t'_D)\right)^2} dt'_D\right) \tag{6.9}$$

with τ_{switch} determining the switching process's duration. This time corresponds to the experimental switching pulse.

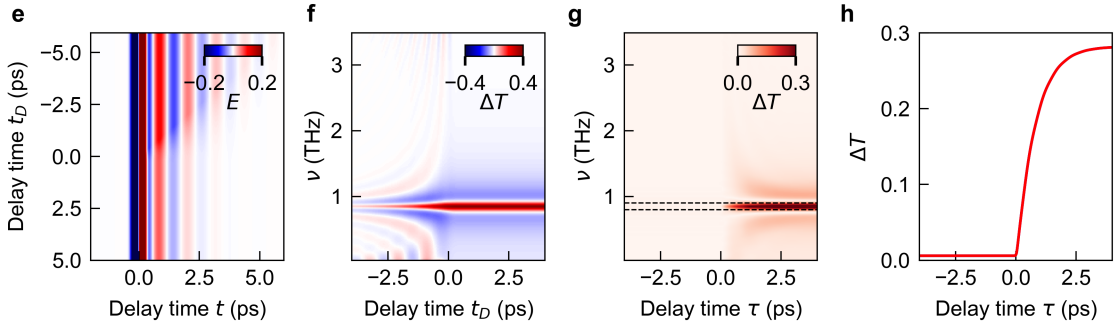

Figure 6.8: Linear response function for a single resonance. (a) Calculated transmitted field transients of a single resonance centred at $\nu_0 = 0.85$ THz, which is rapidly altered by increasing the damping by a factor of two, for various pump delay times t_D. (b) Corresponding differential transmission spectra obtained by Fourier transformation along t, after subtraction of the response without switching. The spectra exhibit oscillations along t_D with a frequency which increases for increasing detuning to the resonance ν_0. (c) Linear response function calculated after transformation of the data into the τ-frame. (d) Differential transmission $\Delta T(\nu, \tau)$ extracted at the resonance frequency ($\nu = 0.85$ THz).

6.3.2 Switching of uncoupled resonances

We first test the model by switching a single uncoupled resonance by increasing the cavity damping by a factor of two. Figs. 6.8 show the resulting time dependent calculations. In Fig. 6.8a, the transient field shows that it is abruptly changed along $t = -t_D$. The Fourier transform of these time domain data (after subtracting the unperturbed transmitted signal), reveals that the single resonance at $\nu_0 = 0.85$ THz is modified through switching (Fig. 6.8b). As intended in the construction of our model, the damping is increased for $t_D > 0$ to simulate the switch-off. This leads to a weakened and broadened transmission at ν_0, clearly visible in the increased differential transmission (red area for $t_D > 0$). At delay times smaller $t_D = 0$ ps, another remarkable feature appears: the perturbed free-induction decay (PFID) [132]. The perturbed decay of the polarization leads to complex, distinct spectral oscillations of ΔT, whose frequencies depend on the spectral separation between the resonance and the delay time t_D. We obtain the spectrally resolved transmission, enabling us to track the time dependent development of the resonance, by transforming the data into the τ-frame (see Chapter 3.4). The proper time dependent transmission function

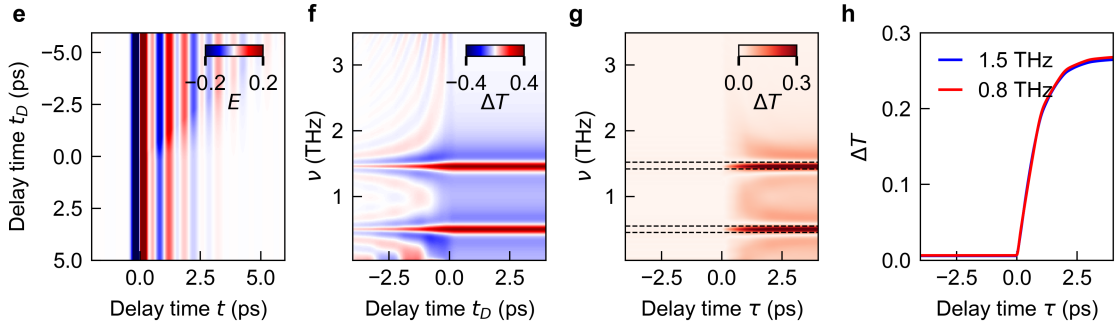

Figure 6.9: Linear response function for two independent resonances. (a) Calculated transmitted field transients of two independent resonances centred at $\nu_0 = 0.5\,\mathrm{THz}$ and $\nu_1 = 1.5\,\mathrm{THz}$, which are rapidly altered by increasing the damping by a factor of 2 for various pump delay times, t_D. (b) Corresponding transmission spectra obtained by Fourier transformation along t, after subtraction of the response without switching. The spectra exhibit oscillations along t_D with a frequency which increases for increasing detuning to the resonances. (c) Linear response function calculated after transformation of the data into the τ-frame, demonstrating that the overall response of uncoupled resonances is obtained by linear superposition. (d) Transmission $\Delta T(\nu, \tau)$ extracted at the resonance frequencies.

$\Delta T(\nu, \tau)$ (Fig. 6.8c), now traces the spectral response of the oscillator during switching. In this time frame, the resonance is switched at $\tau = 0\,\mathrm{ps}$, without a differential signal before time-zero. At the resonance frequency the transmission changes smoothly, without spectral or temporal oscillations (Fig. 6.8d). The switching of a single resonance has thus been shown, but is not sufficient to understand the observed dynamics of our structure.

We add a second uncoupled mode, to test if the deactivation characteristics, that have been observed for decoupling of structures in the ultra- and deep-strong coupling regime (see Chapter 6.2), can be simulated without coupling. In this case, the oscillatory features would stem only from a superposition of two modes with different frequencies. The frequencies of these two modes are chosen to correspond to ν_LP and ν_UP of *Sample A* at the anti-crossing point. The damping of both resonances is rapidly ($\tau_\mathrm{switch} = 100\,\mathrm{fs}$) enhanced, leading to the transmitted THz fields in the time domain frame shown Fig. 6.9a. The time domain data strongly resemble the calculated data of a single resonance (Fig. 6.8 a). The differential transmission in the t_D-frame (Fig. 6.9b) shows for $t_\mathrm{D} > 0$, after the damping

has been increased, the decreased and broadened transmission of both resonances. The PFID, observed for $t_D < 0$ ps, of both resonances superpose, leading to a more strongly structured spectrum between the two resonances (Fig. 6.9b). Yet the transformation into the τ-frame reveals that this superposition does not structure the transition of the uncoupled resonances. Their transition (Fig. 6.9c) remains as smooth as for a single resonance. This is especially clearly visualized by the differential transmission at the frequencies of the two resonances. It is evident, that the switching signatures, observed in our experiments, can not be calculated by uncoupled resonances. In contrast to our polaritons, uncoupled resonances transit smoothly from their initial to final state, lacking the strong oscillatory features observed in the experiment. To sum up, to illustrate the internal mechanisms occurring for light-matter decoupling, we need to couple the cavity resonance to the polarization field of a matter excitation and abruptly deactivate the coupling.

6.4 Subcycle oscillations

We start by examining the coupling of a cavity and a matter system with $\frac{\Omega_R}{\omega_0} = 0.1$, which provides a simplified test bed. Coupling cavity and matter excitation leads to a periodic energy exchange with the vacuum Rabi frequency Ω_R. For a $\nu_0 = \nu_c = 0.85$ THz, the frequency of the LP is $\nu_{LP} = 0.78$ THz and for the UP $\nu_{UP} = 0.96$ THz. The response of a coupled system is determined by the instant polarization of cavity and matter, which is shown in Fig. 6.10a. The real part of the cavity and 90° phase-shifted matter polarization oscillate with the polariton frequencies, while their envelop oscillates with the vacuum Rabi frequency $\Omega_R/2\pi = 0.1 \cdot \omega_0 = 0.085$ THz. The energy is exchanged between the energy stored in the cavity mode, the matter and the coupling mechanism itself. We calculate these mean-field energies from their individual Hamiltonian:

$$\left\langle E_{\text{cavity}} \right\rangle = E_{\text{cavity}} = \hbar\omega_{LC} \left|\alpha_{LC}\right|^2 + \hbar\Omega_R \left(\alpha_{LC} + \alpha_{LC}^*\right)^2, \tag{6.10}$$

$$\left\langle E_{\text{matter}} \right\rangle = E_{\text{matter}} = \hbar\omega_c \left|\beta\right|^2, \tag{6.11}$$

$$\left\langle E_{\text{coupling}} \right\rangle = E_{\text{coupling}} = \hbar\Omega_R \left(\alpha_{LC} + \alpha_{LC}^*\right)\left(\beta + \beta^*\right). \tag{6.12}$$

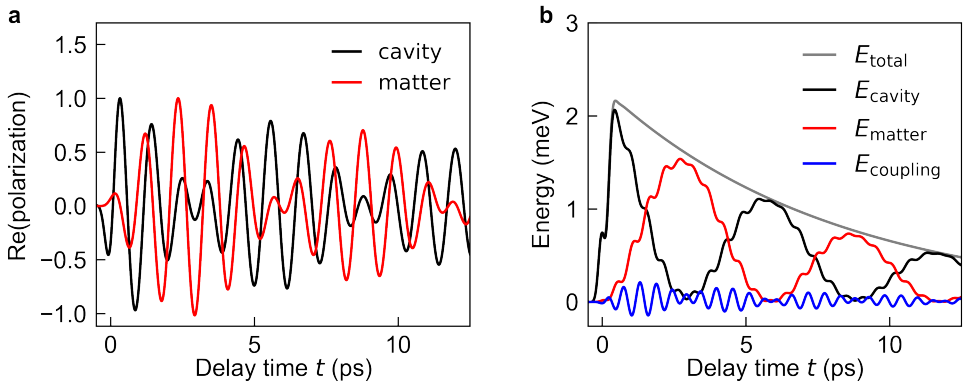

Figure 6.10: Calculations for $\frac{\Omega_R}{\omega_0} = 0.1$. (a) Real part of the polarization of the cavity (black curve) and the matter (red curve) characterized by $\frac{\Omega_R}{\omega_0} = 0.1$. (b) The energy is exchanged periodically between the cavity (E_{cavity}, black curve) and the matter (E_{matter}, red curve) with the Rabi frequency Ω_R. Only a small part of the energy is stored in the coupling mechanism ($E_{coupling}$, blue curve).

For the case of $\frac{\Omega_R}{\omega_0} = 0.1$, the energy distribution as a function of the delay time t is depicted in Fig. 6.10b. The initial high value of E_{cavity} (black curve) at $t = 0\,\text{ps}$ is caused by the external field, which couples only to the cavity and excites the system at $t = 0\,\text{ps}$. After excitation, the energy is periodically transferred to the matter (red curve) and coupling mechanism (blue curve) and back to the cavity. E_{coupling} is relatively small in this example, as it is directly proportional to the coupling strength $\frac{\Omega_R}{\omega_0} = 0.1$. The damping of cavity and matter polarization determine the exponential decrease of the total energy $E_{\text{total}} = E_{\text{cavity}} + E_{\text{matter}} + E_{\text{coupling}}$ (grey curve).

In a next step, we increase the coupling strength between cavity and polarization, which renders the energy distribution more complex. We choose a coupling strength $\frac{\Omega_R}{\omega_{LC}} = 0.57$, matching *Sample A*, which is discussed in Chapter 6.2. Ω_R is set to zero within $\tau_{\text{switch}} = 100\,\text{fs}$, corresponding to the FWHM of our experimental switching pulse. Before switching, in our model the field oscillates at the frequencies of both polaritons ($\nu_{\text{LP}} = 0.48\,\text{THz}$ and $\nu_{\text{LP}} = 1.49\,\text{THz}$). As the calculated time domain data (Fig. 6.11a) show, the transmitted THz field at $t_D = -t$, changes abruptly. The abrupt change is followed by a strongly structured response, apparent in the triangular region defined by $t_D < 0$ and $|t_D| < t$. As soon as the final state is reached, the field oscillates at the uncoupled light mode frequency. This behaviour clearly differs from the switching signatures of

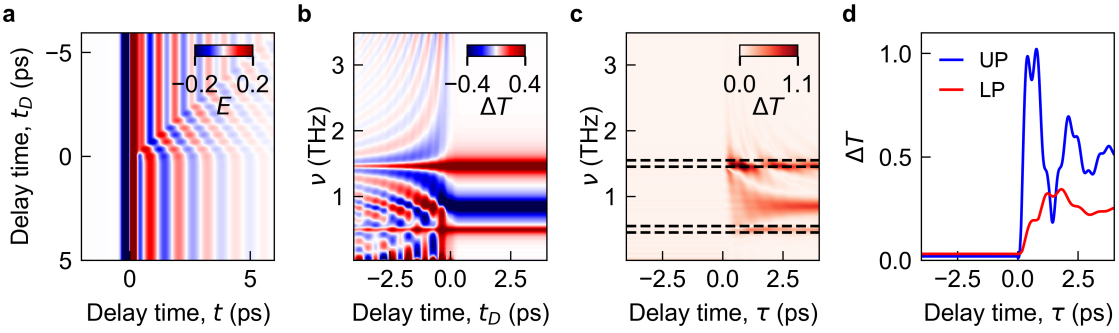

Figure 6.11: Linear response function for coupled resonances. (a) Calculated transmitted field transients of a cavity ($\nu_0 = 0.85\,\mathrm{THz}$) ultrastrongly coupled to a matter resonance ($\nu_c = \nu_0$) with a coupling strength of $\frac{\Omega_R}{\omega_0} = 0.57$. Here, switching occurs by setting Ω_R to zero within $\tau_{switch} = 100\,\mathrm{fs}$. (b) Corresponding transmission spectra obtained by Fourier transformation along t, after subtraction of the response without switching. (c) Linear response function calculated after transformation of the data of (a) into the τ-frame. (d) Transmissions $\Delta T(\nu, \tau)$ extracted at the resonance frequencies of the polaritons, UP and LP (frequency ranges indicated by dashed lines in (c)).

the uncoupled modes. It is reasonable to attribute this specific behaviour to the fact that both polariton resonances are affected at the same time. The periodic signal is observable in $\Delta T(\nu, t_D)$ (Fig. 6.11b): Before zero, the spectrum is highly structured. Even on the resonance frequencies of the polaritons an oscillating variation of the transmission is visible. For $t_D > 0\,\mathrm{ps}$, the polaritons have vanished (apparent from the strong transmission increase at their resonance frequencies) and the uncoupled LC mode is visible at $\nu_0 = 0.85\,\mathrm{THz}$. In the τ-frame (Fig. 6.11c) the peculiar behaviour becomes even more prominent due to the pronounced oscillations in the differential transmission. These oscillations are most pronounced at the resonance frequencies of the extinguished polaritons for $\tau > 0$ (Fig. 6.11d for the LP and UP). The theory therefore demonstrates, that the decoupling of an ultrastrongly coupled system leads to oscillatory features at the resonance frequencies. We want to stress out, that these oscillations can not be modelled by uncoupled resonances. Thus they are a signature of decoupling, only observable if the coupling of two resonances is modified.

To understand these oscillations, arising for a non-adiabatic deactivation of ultrastrong

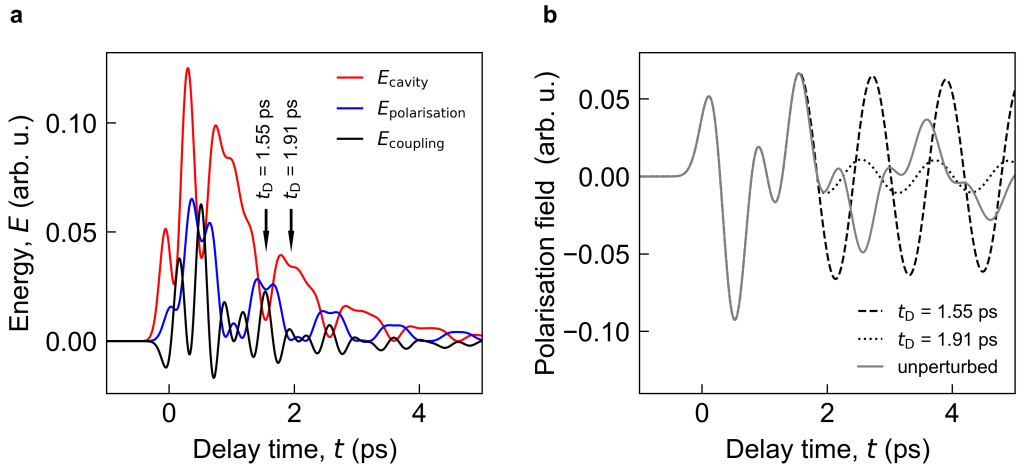

Figure 6.12: Energy and polarization dynamics relevant for the switching process. (a) In a setting characterised by $\frac{\Omega_R}{\omega_0} = 0.57$ and including anti-resonant coupling terms, the energy exchange between the cavity (E_{cavity} , red curve), the electronic excitation (E_{matter} , blue curve), and the coupling mechanism (E_{coupling}, black curve) is strongly structured and exhibits various, qualitatively different situations for switching. (b) Polarization field for two examples of different switching situations for which the cavity energy has a local minimum ($t_D = 1.55$ ps, left arrow in panel a), or a local maximum ($t_D = 1.75$ ps), respectively, lead to different phases and amplitudes of the polarization oscillation after switching (dashed and dotted black curves). Grey curve, polarization field without switching.

coupling, we take a closer look at the energy distribution of the coupled system. The periodic energy exchange between the light and matter modes and the coupling mechanism itself are depicted for the case of $\frac{\Omega_R}{\omega_{LC}} = 0.57$ in Fig. 6.12a. The picture is now more complicated than for case of $\frac{\Omega_R}{\omega_{LC}} = 0.1$: Depending on the delay time t, the energy is split between the cavity (red curve), the matter polarization (blue curve) and the coupling mechanism (black curve). Two fundamentally different switching scenarios now unfold, depending on whether the switching is triggered at the maximum or at the minimum of the cavity or the matter energy. Fig. 6.12b shows that the rapid quench of the coupling leads to periodically oscillating starting conditions for the subsequently freely oscillating matter polarization. Switching during a local minimum of E_{cavity} (at $t_D = 1.55$ ps), the polarization oscillation amplitude of the matter is maximized (Fig. 6.12b, dashed black curve) whereas switching during a local minimum of the matter energy (at $t_D = 1.91$ ps) minimizes the

oscillations (Fig. 6.12b, dotted black curve). Once the switching pulse abruptly interrupts the transfer, the subsequent dynamics of the uncoupled cavity and electronic polarization are defined by the corresponding instantaneous field amplitudes at the time of switching. The rapid oscillations of the deep-strongly coupled fields, progressing faster than a single polariton oscillation cycle, lead to equivalently rapid oscillations of the response function as a function of the switching time. This rapid, oscillating succession of fundamentally different switching conditions is the origin of the sub-polariton-cycle oscillations of the response function observed for the deactivation of ultra- and deep-strong coupling.
Our exploration of this limit of light-matter interaction by an abrupt modulation of Ω_R has revealed a novel class of extremely subcycle, high-frequency oscillatory dynamics of the optical response functions. These oscillations are observable in our experiments, too (see Chapter 6.2). The experimental setting is more complex, since there is another light mode, the DP mode. In the following, we therefore expand our model to best fit our experimental setup and get quantitative accordance between calculations and experiment.

6.5 Determination of the switching time

We use our newly developed theory to investigate the switch-off behaviour of the LP, trying to quantitatively fit our experimental data. We know from the numerical analysis of the bare resonator (see Chapter 5.1), that photo-doping of the switching patch, deactivates the LC mode but also red-shifts the DP mode. This is implemented, as well as the deactivation of the coupling, by setting Ω_R to zero. A fitting procedure, where we optimize γ_{LC}, γ_{DP}, κ_{DP} and κ_{LC}, for a coupling strength of $\frac{\Omega_R}{\omega_0} = 0.57$ and $\tau_{switch} = 100\,\text{fs}$ leads to the differential transmission at ν_{LP} shown in Fig. 6.13 (red line). For comparison, the experimental data (solid black curve and circles) are shown, too. It is apparent that, theory and experiment agree very well regarding the following features: The initial oscillation around $\tau = 0\,\text{ps}$, the subsequent steep rise accounting for most of the transmission change during switching, the pronounced local minimum around $\tau = 1\,\text{ps}$, and the subsequent dynamics up to $\tau = 1.5\,\text{ps}$. The calculated transmission matches that of the experiment within less than 8×10^3 of absolute error (indicated by $\sigma_{\Delta T}$). As the local extrema of ΔT of theory and experiment coincide temporally within this range, the frequencies of the sub-polariton-cycle oscillations are also adequately reproduced. We also estimated the parameter range within

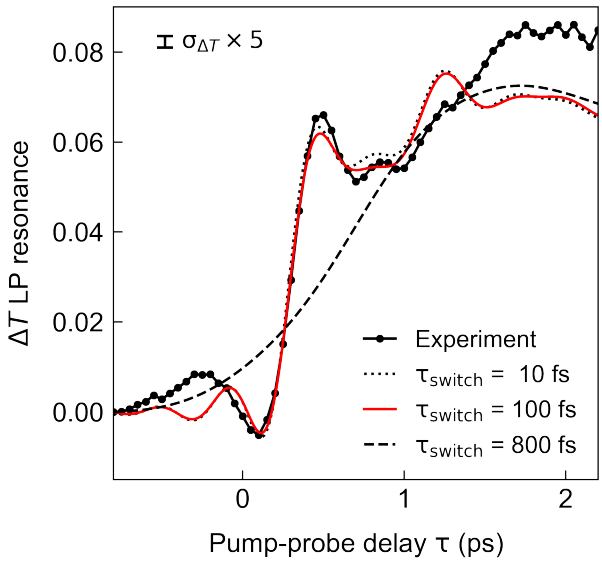

Figure 6.13: Sub-polariton-cycle oscillations of the LP. Calculation of ΔT at the LP resonance for various switching times: $\tau_{\text{switch}} = 10\,\text{fs}$ (dotted curve), $\tau_{\text{switch}} = 100\,\text{fs}$ (red curve) and $\tau_{\text{switch}} = 800\,\text{fs}$ (dashed curve). For reference, the experimental data (solid black curve and circles) are added.

which the calculations satisfactorily reproduce the experiment, by a variation of the fitting parameters (see Appendix A.3).

We now use our model to extract the switching time. We calculated the response of the decoupling of a system characterised by $\frac{\Omega_R}{\omega_0} = 0.57$ for different switching durations τ_{switch}. Our calculations show that the signature oscillations for the switch-off of ultrastrong coupling only occur for sufficiently fast switching. In contrast, long switching durations average out the energy oscillations and lead to a more adiabatic transition (Fig. 6.13, dashed curve). A quantitative comparison with the experimental data allows us to identify the upper limit of the switching time at $\tau_{\text{switch}} = 100\,\text{fs}$. This corresponds to a fraction of $\frac{\tau_{\text{switch}}}{T_{\text{LP}}} = 0.05$, with the oscillation period of the LP, with $T_{\text{LP}} = \nu_{\text{LP}}^{-1}$.

Our calculations therefore suggest, that we indeed deactivate the coupling extremely non-adiabatically. This conclusion is also supported by the following considerations concerning the screening of the electric near-field of the fundamental LC by a photo-induced charge carrier plasma [131]. The plasma is created by femtosecond excitation with near-infrared optical pulses of a duration of 70 fs (FWHM). The pulse photo-excites a carrier density

of $\rho_{\mathrm{switch}} = 3.5 \times 10^{18}\,\mathrm{cm}^{-3}$ which corresponds to an electron plasma frequency of $\nu_{\mathrm{p}} =$ 80 THz. The build-up time of this plasma and therefore of the screening is $t_{\mathrm{screening}} = \nu_{\mathrm{p}}^{-1} =$ 12 fs [89, 131]. As the decoupling mechanism is based on the cut-off of the LC's near-field through the charge carrier plasma (see Chapter 5), which is built within approximately the duration of the switching pulse 70 fs. An upper limit of the decoupling time of 100 fs is clearly justified.

For our most strongly coupled structure, *Sample C*, 100 fs switch-off time correspond to a to a fraction of $\frac{\tau_{\mathrm{switch}}}{T_{\mathrm{LP}}} = 0.02$, with the oscillation period of the LP $T_{\mathrm{LP}} = \nu_{\mathrm{LP}}^{-1} = 5\,\mathrm{ps}$. In summary, our concept of femtosecond reshaping of cavity modes by strongly subwavelength switch elements enables a non-adiabatic, within less than 100 fs, control of light-matter coupling in the deep-strong coupling regime. This result is confirmed by our newly developed theory, which not only allowed for the identification of the upper limit of the deactivation process, but also showed that the oscillatory switch-off behaviour of the polaritons is a signature of the decoupling in the ultrastrong coupling regime.

6.6 Theoretical predictions

The theoretical model already allowed to unambiguously link the high-frequency dynamics we observed in our experiments to the decoupling process. Our model describes coupling between light and matter modes, taking into account anti-resonant interaction terms and the diamagnetic term, which are relevant in the ultrastrong coupling regime. We included time dependent coupling strength Ω_{R}, to account for the abrupt deactivation of light-matter coupling. This theory therefore enables us to investigate non-adiabatic dynamics of internal variables of deep-strong coupling during switch-off. We expand our study by a discussion of the state of the matter after decoupling including the especially interesting situation for a coherent excitation of only the LP. Therefore, considerations regarding the absence of a coherent field, exciting the system, as well as considerations regarding the population of the ground state are presented in the following section.

6.6.1 Coherent energy transfer

In a particularly illustrative picture, we consider the energy redistribution after coherent excitation of only the LP resonance. Therefore we examine the light-matter Hamiltonian for a coherent excitation of only the LP. Diagonalizing the Hopfield matrix [7], leads to the Hopfield coefficients $w_\mathrm{i}, x_\mathrm{i}, y_\mathrm{i}, z_\mathrm{i}$ (i = LP, UP). Via a Bogoliubov transformation, the light-matter Hamilton operator can be expressed in terms of normal-mode polariton operators, $\hat{p}_i, \hat{p}_\mathrm{i}^\dagger$, with $\hat{p}_\mathrm{i} = w_\mathrm{i}\hat{a}_\mathrm{LC} + x_7\hat{b} + y_\mathrm{i}\hat{a}_\mathrm{LC}^\dagger + z_\mathrm{i}\hat{b}^\dagger$. For this unitary transformation, the reverse transform assumes the form [7]

$$\begin{pmatrix} \hat{a}_\mathrm{LC} \\ \hat{b} \\ \hat{a}_\mathrm{LC}^\dagger \\ \hat{b}^\dagger \end{pmatrix} = \begin{pmatrix} w_\mathrm{LP} & w_\mathrm{UP} & -y_\mathrm{LP} & -y_\mathrm{UP} \\ x_\mathrm{LP} & x_\mathrm{UP} & -z_\mathrm{LP} & -z_\mathrm{UP} \\ -y_\mathrm{LP} & -y_\mathrm{UP} & w_\mathrm{LP} & w_\mathrm{UP} \\ -z_\mathrm{LP} & -z_\mathrm{UP} & x_\mathrm{LP} & x_\mathrm{UP} \end{pmatrix} \cdot \begin{pmatrix} \hat{p}_\mathrm{LP} \\ \hat{p}_\mathrm{UP} \\ \hat{p}_\mathrm{LP}^\dagger \\ \hat{p}_\mathrm{UP}^\dagger \end{pmatrix}. \tag{6.13}$$

If only the LP is excited by a coherent field, the polariton operator of the UP is zero ($\hat{p}_\mathrm{UP} = 0$) and $\hat{p}_\mathrm{LP} = Ae^{i\omega t}$, whereby A is given by the external field. The mean-field expectation values for this case then are:

$$\alpha_\mathrm{LC} = w_\mathrm{LP}Ae^{i\omega t} - y_\mathrm{LP}Ae^{-i\omega t} \tag{6.14}$$

and

$$\beta = x_\mathrm{LP}Ae^{i\omega t} - z_\mathrm{LP}Ae^{i\omega t}. \tag{6.15}$$

$E_\mathrm{coupling} = \hbar\Omega_\mathrm{R}\left(\alpha_\mathrm{LC} + \alpha_\mathrm{LC}^*\right)(\beta + \beta^*)$ is proportional to the in-phase quadratures of the cavity field and the polarization and can exceed their individual energies, E_cavity and E_matter, respectively. Fig. 6.14 the combined value depicts the Hopfield coefficients (cf. Fig. 2.3) relevant for the E_coupling if only the LP is excited. $\left(\alpha_\mathrm{LC} + \alpha_\mathrm{LC}^*\right)$ is then dependent on $w_\mathrm{LP} - y_\mathrm{LP} + w_\mathrm{LP}^* - y_\mathrm{LP}^*$ (dashed curve) and $(\beta + \beta^*)$ on $x_\mathrm{LP} - z_\mathrm{LP} + x_\mathrm{LP}^* - z_\mathrm{LP}^*$ (dotted curve). Considering the sign of the combined coefficients, $\left(\alpha_\mathrm{LC} + \alpha_\mathrm{LC}^*\right)(\beta + \beta^*) < 0$ (Fig. 6.14, black curve), leads to a strictly negative E_coupling. This negative coupling energy (Fig. 6.15, red curve) balances the synchronous oscillations of E_cavity (Fig. 6.15, black curve) and E_matter (Fig. 6.15, dashed black curve) and may become a key factor for the switching dynamics.

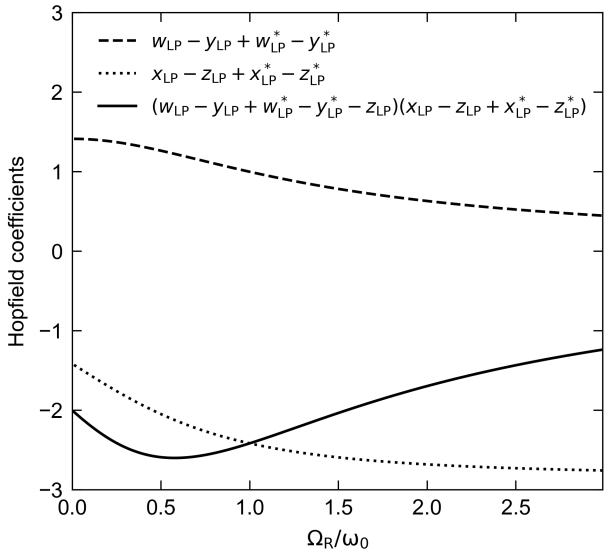

Figure 6.14: Hopfield coefficients of E_{coupling}. The mixing fractions for the cavity $\alpha + \alpha^*$ (dashed curve) and the polarization $\beta + \beta^*$ (dotted curve) as a function of the coupling strength $\frac{\Omega_R}{\omega_0}$ show E_{coupling}, proportional to the field quadratures $\left(\alpha_{LC} + \alpha^*_{LC}\right)(\beta + \beta^*)$ (black line depicting the combined Hopfield coefficients), is strictly negative.

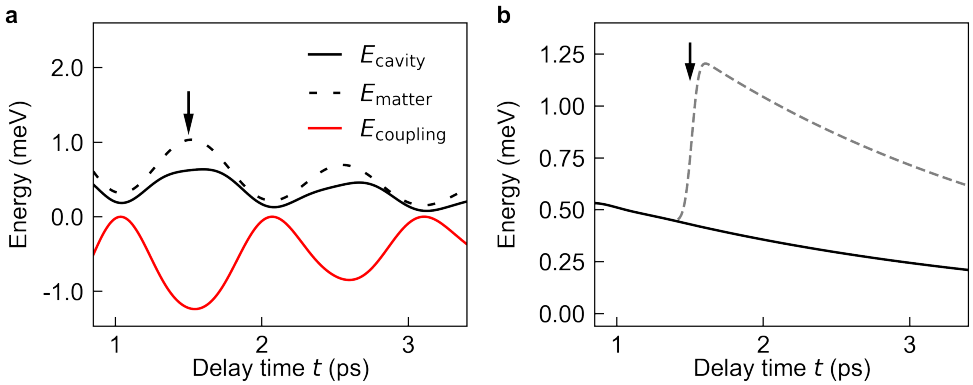

Figure 6.15: Phase-coherent energy transfer during quasi-instantaneous switching of the deep-strongly coupled matter resonance. (a) Energy of the cavity (solid black curve), matter (dashed black curve) and coupling (red curve) when only the LP is excited. The grey and black arrows indicate times close to local minima and maxima of the cavity and matter energies, respectively. (b) Total energy without switching (solid black curve), and for the case that non-adiabatic switching occurs when the cavity energy is maximized (dashed grey curve).

Looking at the total energy of a system where only the LP is excited (Fig. 6.15b, black line), effects of the negative coupling energy when switching-off the coupling strength become clear: If the subcycle switch-off of the coupling occurs when E_{coupling} is close to zero, the total energy is not strongly affected. In contrast, switching during a local minimum of E_{coupling}, the energy stored in the coupling mechanism can be partially transferred into the uncoupled modes, causing a net increase of the total energy (Fig. 6.15b, grey dashed curve).

We have therefore identified a coherent energy transfer from the coupling mechanism to the matter that remains after switching. This energy transfer is also present for an excitation of both the LP and UP, but as the coupling energy is not strictly negative for this case the transfer is not as pronounced and only valid for selected switching times (also see Fig. 6.12b).

6.6.2 Vacuum population of the ground state

Our theory not only allows for predictions on the remaining matter state after switch-off of light-matter coupling, it also enables discussions on the vacuum photon release. The

above discussed energy transfer mechanism works with and without an external THz field. This mechanism may liberate virtual excitations from the vacuum ground state and promote them to real excitations of the matter mode. In conceptual analogy, future experiments may exploit the same mechanism to promote virtual excitations from the incoherent vacuum ground state to real excitations. In combination with recent cutting edge quantum spectroscopy, this concept could form an excellent table-top laboratory to explore quantum electro dynamical phenomena similar to the Unruh-Hawking radiation of black holes [2]. In this setting, the matter mode of our *Sample C* would be populated by 0.32 excitations per resonator, which are expected to modify transport properties or radiate into the far-field, where they could be detected by cutting edge quantum [51] or correlation spectroscopy [10]. The release of vacuum photons of this scenario, and switching our most strongly coupled structure, the AlSb/InAs sixfold QW, which showed a coupling strength of 2.76, would lead to 0.9 released vacuum photons for each resonator. This puts their detection into reach.

7 Conclusion

Vacuum fluctuations manifest themselves mainly indirectly, hence possibilities to study this non-classical form of light are highly sought-after. Cavity polaritons in cQED systems provide an interesting platform to study squeezed quantum vacuum, since they arise for the quantum fluctuations of the electromagnetic field ground state. Due to the anti-resonant terms of the Hamiltonian, the ground state of this system is a squeezed vacuum containing a finite number of virtual photons, which nonlinearly depends on the coupling strength. Non-adiabatically modulating the coupling strength of such a system is predicted to be accompanied by the release of vacuum photons.

In the present work, we wanted to realize two objectives: Firstly, to experimentally explore how far the coupling between subwavelength THz resonators and cyclotron transitions of Landau-quantized 2DEGs can be pushed. And secondly, to non-adiabatically modulate the coupling strength and investigate arising dynamics in the deep-strong coupling regime.

We addressed the first objective, the maximization of the coupling strength and exploration of the deep-strong coupling regime, through dedicated heterostructure design. Our study started with state of the art AlGaAs/GaAs heterostructures hosting multiple 2DEGs - a model system for extremely strong coupling [13, 17–19, 55, 61]. This study of the matter part of light-matter coupling is based on the optimization process of Bayer [93], who found epitaxial limits regarding doping density as well as spatial compactness for the tightly stacked AlGaAs/GaAs QWs. We managed to increase the coupling strength beyond these limits by reconsidering the stacking design. While at first sight, the stacking may seem unattractive, since the light mode decreases strongly in the QW stack, we demonstrated multi-QWs which allowed to significantly increase the coupling strength: Coupling a 12-fold QW stack to the light mode of MM IV resulted in a coupling strength of $\frac{\Omega_R}{\omega_0} = 2$. This marks a new record for Landau polariton systems, exceeding the former record coupling strength of $\frac{\Omega_R}{\omega_0} = 1.43$ achieved by a sixfold QW [17]. The stacking of QWs

has therefore been identified as a promising way to enhance the coupling strength. This is supported by numerical calculations which suggest that the stacking concept may be pushed even further. Thus, as an outlook for this approach, we grew 24- and 48-fold QW stacks. Yet, our coupling experiments revealed that it gets more and more challenging to identify the polaritons for increasing coupling strengths. Hence, more thorough analysis to precisely determine the coupling strength is required.

The GaAs-based model system served as a platform for our investigation of subcycle dynamics in the deep-strong coupling regime in the 2nd part of this thesis. Before that, to further explore how high the coupling strength can be pushed by material development, we went beyond GaAs heterostructures to strengthen the transition dipole moment of the matter excitation. We concentrated on the effective mass of the Landau electrons and chose MBE grown InAs heterostructures, which promise strongly decreased effective masses, compared to GaAs.

Building upon the optimization process of GaAs heterostructures, we grew symmetrically doped tightly stacked $In_{81.5}Al_{18.5}As/In_{81.5}Ga_{18.5}As/InAs$ QWs on step graded buffer systems. The high quality 2D-system exhibited an effective mass of $0.038\,m_e$ approximately half the mass of the electrons in our AlGaAs/GaAs structures. Comparing the coupling of a sixfold AlGaAs/GaAs QW with a sixfold $In_{81.5}Al_{18.5}As/In_{81.5}Ga_{18.5}As/InAs$, clearly shows the effect of the reduced mass: In spite of a lower electron density, the InAs QW stack achieved a coupling strength of $\frac{\Omega_R}{\omega_0} = 1.67$ which surpasses all coupling strengths achieved in sixfold AlGaAs/GaAs QW stacks. However, we did not manage to attain electron sheet carrier densities as high as for GaAs QWs, reaching a limit of the heterostructure layout regarding the doping density. Exceeding this limit resulted in a strong parallel bulk conduction in addition to the transport in the 2DEGs. This rendered the identification of the polaritons impossible. Since the doping density of this system can not easily be further increased, it seems worthwhile to increase the number of QWs in the stack, like in GaAs.

Triggered by these limitations on the doping density, we studied a second InAs-based system: narrow InAs wells embedded in AlSb barriers, which may combine low effective masses with deep quantum confinement. These heterostructures are known for their high defect-induced doping and more importantly for their high doping efficiency [99], caused by their confinement energy. Indeed, InAs QWs of a thickness of 15 nm revealed the potential of extremely high sheet carrier densities of $\rho_{2DEG} > 2 \times 10^{12}\mathrm{cm}^{-2}$, which is

significantly higher than in our InAlAs/InGaAs/InAs heterostructures. The relatively low effective masses of $m^* = 0.046\, m_e$ combined with this extremely high electron density resulted in a record coupling strength of $\frac{\Omega_R}{\omega_0} = 2.76$ for a sixfold QW. This sets a new record largely exceeding even the highest published coupling strength $\frac{\Omega_R}{\omega_0} = 1.8$ [60]. A system characterized by such a strong coupling provides a promising platform to access the highly unusual properties of a deep-strongly coupled light-matter hybrid state such as its nonlinear response under strong optical fields [133].

To create a setting for the realization of the second objective of this thesis - non-adiabatic modulation of light-matter coupling - an ultrafast, switchable THz metamaterial compatible with a heterostructure is required. For our model AlGaAs/GaAs system, we designed a custom tailored active metamaterial, offering ultrafast controllable electro-magnetic properties through photo-excitation of semiconductor patches adapted to the metamaterial design. The semiconductor we chose was InGaAs, as its band gap energy lies well below the band gap energy of the GaAs heterostructure. Hence, the semiconductor switching patch offers the possibility to activate the switching without perturbing a coupled GaAs matter system. The selectivity of the switching process is further enhanced by the geometry of our switching structure, which is limited to the crucial resonator regions. The switch-off of the light mode is induced by a 70 fs pump pulse, which creates photo-excited carriers in the InGaAs patch. The photo-excited charge carrier plasma, that builds up in 12.5 fs, screens the fundamental LC mode of the THz resonators, effectively switching-off the resonance. While we presented this switching concept for two resonator geometries, it is universally applicable to any LC-based THz resonator design. Our study on a sub-picosecond time scale with MM I demonstrated subcycle switch-off of the light mode in less than 1 ps, faster even than one cycle of the light $T_{LC} = 1.25$ ps.

Having successfully demonstrated the prerequisite to non-adiabatically modulate the coupling strength in a Landau polariton system, we next explored the dynamics of deep-strong coupling. We combine the custom tailored switchable resonators and our AlGaAs/GaAs QW stacks, resulting in coupling strengths of up to $\frac{\Omega_R}{\omega_0} = 1.3$. Femtosecond photo-excitation of the integrated InGaAs switch element manipulated the fundamental cavity mode such that it decoupled from the cyclotron resonance. This successful deactivation is evidenced by quasi-steady state measurements shortly (2 ps) after the switching event. Moreover, our time dependent study revealed that the coupling strength

is switched-off more than an order of magnitude faster than the oscillation cycle of light, while exhibiting high-frequency oscillatory dynamics of the optical response function. The extremely fast switch-off of Ω_R marks the first non-adiabatic modulation of the coupling strength in the deep-strong coupling regime.

Thus, we have reached our objective, but wanted to further explore the intriguing dynamics that arises when electrons are non-adiabatically undressed. To this end, we developed a mean-field theory, which enabled the simulation of a time-modulated light-matter coupled system. Our theory takes into account the time dependent coupling strength and anti-resonant interaction terms to account for the deep- and ultrastrong coupling regime. This theory not only allows for the confirmation of the switch-off time of our system, but also enables the analysis of the intriguing physics of the light and matter mode during and after switching. Comparing the experimentally obtained switch-off dynamics with numerical calculations facilitated to establish the switch-off time of less than 100 fs, underlining the non-adiabaticity of the deactivation process. The extremely fast modulation of Ω_R has also revealed a novel class of subcycle, high-frequency oscillatory dynamics of the optical response function in the experiment. Using our model, we were able to link these sub-polariton-cycle oscillations of the transmission to the non-adiabatic extinction of the polariton states. Furthermore, the theory identified a sizeable energy transfer into the matter mode due to the switch-off of the coupling strength. This energy transfer takes place even without coherent excitation.

This work has put into reach the direct detection of vacuum photons, released from the ground state of extremely strongly coupled polaritons. Switching in the demonstrated setting may liberate virtual excitations from the vacuum ground state and promote them to real excitations that radiate into the far-field. The ground state of our AlGaAs/GaAs structures with a coupling strength of $\frac{\Omega_R}{\omega_0} = 1.3$ is populated by an amplitude-squeezed number state containing 0.32 excitations. When radiated into the far-field, these excitations could be detected by cutting edge correlation spectroscopy [10]. Of course, as the number of vacuum photons increases with the coupling strength, switching of our AlSb/InAs structures is obviously attractive. For our most strongly coupled structure, the sixfold AlSb/InAs QW stack characterized by a coupling strength of $\frac{\Omega_R}{\omega_0} = 2.76$ the number of virtual excitations of the light mode reaches 0.9. The increased number of excitations, compared to our GaAs structures, would facilitate their potential detection. In this case, the

switching concept needs to be adapted, requiring a suitable photo-excitable patch material, like InSb, to replace InGaAs. Implementing superconducting metamaterials present another possible solution to control light-matter interaction in an InAs-based system [116].
Beyond the detection of vacuum photons, the control of the vacuum field of deep-strongly coupled structures also paves the way for the observation of other fascinating non-adiabatic dynamics in light-matter hybrid states. Cavity-mediated superconductivity or transport properties controlled by the vacuum field, may now be studied without THz illumination or direct matter excitation. Future structures may include different switching patch materials, complementary control schemes for switch-on of cavity modes or other matter excitations. This could define the groundwork of subcycle control of novel hybrid states created by the coupling to the controllable vacuum field of a cavity.

A Appendix

A.1 Samples

In the following table, the samples that were studied in this thesis are listed.

Material	n_{QW}	Resonator	Name	Wafer
AlGaAs/GaAs	6	MM I, MM III	*GaAs1*	C170607A
AlGaAs/GaAs	6	MM III	*GaAs2*	C180115A
AlGaAs/GaAs	12	MM IV	*GaAs3*	C150521B
AlGaAs/GaAs	24	MM IV	*GaAs4*	C200511A
AlGaAs/GaAs	48	MM IV	*GaAs5*	C200512A
InAlAs/InGaAS/InAs	1	-	*InAs1*	C191216A
InAlAs/InGaAS/InAs	3	-	*InAs2*	C191216B
InAlAs/InGaAS/InAs	3	-	*InAs3*	C200203A
InAlAs/InGaAS/InAs	6	MM IV	*InAs4*	C200224A
InAlAs/InGaAS/InAs	6	MM IV	*InAs5*	C200224B
AlSB/InAs	1	MM II	*InAs6*	C171221A
AlSB/InAs	3	MM IV	*InAs7*	C180328A
AlSB/InAs	6	MM IV	*InAs8*	C200310A
GaAs substrate	-	switchable MM I	-	
AlGaAs/GaAs	3	switchable MM I	*Sample A*	C161025B
AlGaAs/GaAs	6	switchable MM I	*Sample B*	C161025A
AlGaAs/GaAs	6	switchable MM II	*Sample C*	C161025A

A.2 MBE growth of InAs heterostructures

In the following the MBE growth of our InAs based heterostructures are briefly described. They were grown on GaAs substrate grown in (100) orientation in the III-V chamber of the

Regensburg MBE cluster facility of the Bougeard Group, which is described in greater detail in refs. [134–136].

A.2.1 InAlAs/InGaAs/InAs heterostructures

In Chapter 4.2.1, $In_{81.5}Al_{18.5}As/In_{81.5}Ga_{18.5}As/InAs$ heterostructures, grown by M. Prager, are discussed. As high-indium compositions are lattice mismatched to GaAs, direct growth on GaAs substrates results in strain-induced defects and decreased mobility in potential carrier systems. In order to get high quality 2DEGs in the InGaAs/InAs quantum wells, a sophisticated buffer layer structure is employed. Fig. A.1a shows schematically the material composition for a single QW structure. To reduce the strain, a step-graded buffer system with gradually increasing indium content is grown on top of the GaAs substrate. The indium content even exceeds the desired composition ratio, reaching an indium overshoot of 85%. The step graded buffer is followed by 100 nm $In_{81.5}Al_{18.5}As$, to smooth the subsequent active region. This region (Fig. A.1b) consists of 20 nm-thick $In_{81.5}Al_{18.5}As$ barriers, enclosing the InGaAs QW featuring a symmetrically embedded InAs channel. The QW is symmetrically n-doped by a Si δ-doping layer in the InAlAs barriers. The capping of 30 nm InAlAs and 2 nm InGaAs is designed to prevent oxidation of the InAlAs. Fig. A.1c shows the design of multi-QW stacks. The QWs are symmetrically Si-doped, with 20 nm barriers, separating the QWs.
The growth was performed in the III-V chamber of the MBE cluster with a constant arsenic background pressure of about 8×10^{-6} Torr. The substrate temperature was ranging form 340 to 620°C, whereby the QWs were grown at low temperatures. A more detailed description of such structures can be found in other works of our group [104, 105, 137].

A.2.2 AlSb/InAs heterostructures

In order to grow high quality 2DEGs in AlSb/InAs structures on GaAs substrate, a growth scheme, based on the work of ref. [108], was employed. This was further developed to meet the needs for ultimately strong light-matter coupling. The material composition of these structures is shown schematically in Fig. A.2a. The buffer sequence, designed to reduce strain starts with 6 nm AlAs, followed by a 32 nm-thick AlSb buffer to relax strain.

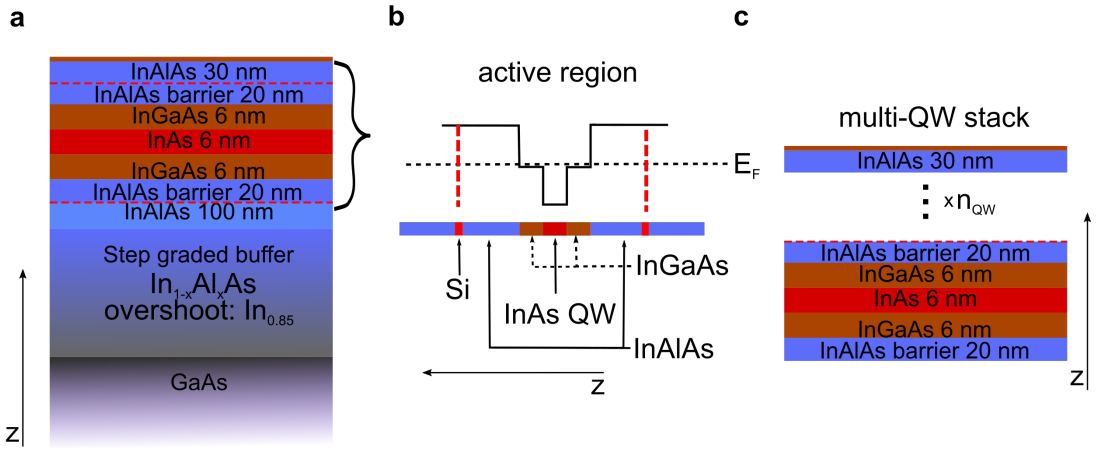

Figure A.1: $In_{81.5}Al_{18.5}As/In_{81.5}Ga_{18.5}As/InAs$ heterostructures. (a) Schematic depiction of the material composition of the heterostructure. The structure was grown on GaAs substrate in z-direction. (b) Layer sequence of the active QW region of the modulation doped InAs heterostructure concept and indication of the energy dispersion of this region. (c) Design of the multi-QW stacks of n_{QW} quantum wells.

This is subsequently followed by 1100 nm $Al_{0.3}Ga_{0.7}Sb$, 500 nm GaSb and a GaSb/SlSb superlattice. The GaSb layer is supposed to reduce the dislocation density. However, GaSb is intrinsically p-type conducting so a thick AlGaAs layer is added to minimize the conduction. A superlattice of ten-periods of GaSb/AlSb was chosen to further improve the morphology and smooth the surface, leading to better transport properties in the subsequent active region. After the buffer layers the active region, consisting of AlSb barriers and a 15 nm InAs QW, follows. The QW is doped by a InAs(Si) inset, where free electrons are provided. This inset is located in the AlSb barrier, 12.5 nm away from the QW. The capping, to prevent the carriers from escaping to the surface was 2 nm thick InAs. In order to further improve transport properties of the 2DEGs, the arsenic background pressure during the QW growth was reduced from 8×10^{-6} Torr to 4×10^{-6} Torr. This was found to be beneficial for the electron mobility in AlSb/InAs heterostructures [101]. The band model of the active region is shown schematically in Fig. A.2b, visualizing the doping concept. Since the coupling strength is dependent on the number of coupled electrons in the system, we also grew samples which contain multiple QWs. The design of such

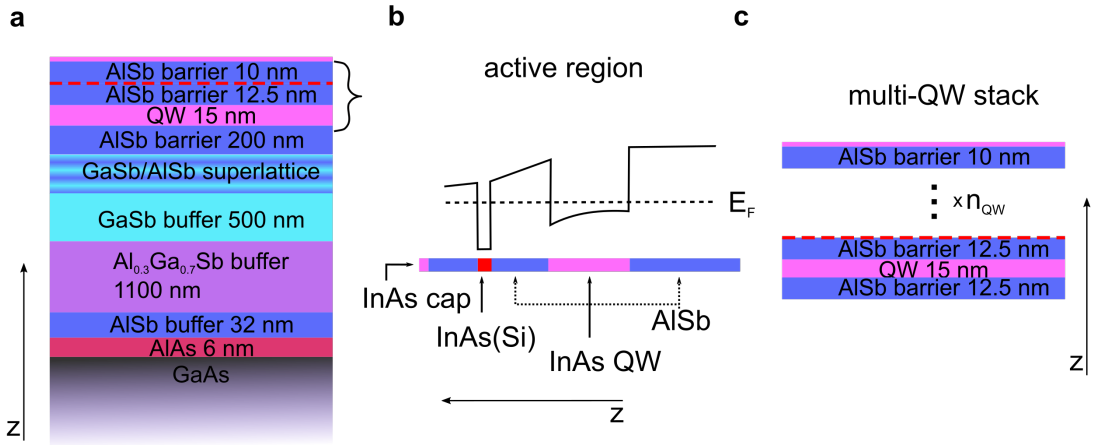

Figure A.2: AlSb/InAs heterostructures. (a) Schematic depiction of the material composition of the heterostructure. The structure was grown on GaAs substrate in z-direction. (b) Layer sequence of the active QW region of the modulation doped InAs heterostructure concept and indication of the band energy dispersion of this region. (c) Design of the multi-QW stacks of n_{QW} quantum wells.

structures is depicted in Fig. A.2c. InAs(Si) insets embedded in 25 nm thick barriers, which separate the QWs. A more detailed description of these structures, and the corresponding growth studies can be found in ref. [113].

A.3 Subcycle oscillations: Quantitative comparison of experiment and theory

In order to quantify the noise of our experiments and further justify our model theory, we analysed the noise level of the time dependent measurement of *Sample A* and determined the parameter range within which the calculations satisfactorily reproduce the experiment. The standard deviation of $\Delta T = 5 \times 10^{-4}$, results from 20 individually measured values of the THz electric field, for each delay step. 10 times this value is visualized in Fig. A.3a as a red-shaded band centred around ΔT of the differential transmission data of the experiment (solid black line). The best fit parameters ($\gamma_{\mathrm{LC,\,min}}$, $\gamma_{\mathrm{DP,\,min}}$, $\kappa_{\mathrm{LC,\,min}}$ and $\kappa_{\mathrm{DP,\,min}}$, see also Fig. 6.13) result in the fit which is also depicted in Fig. A.3a (dashed grey line).

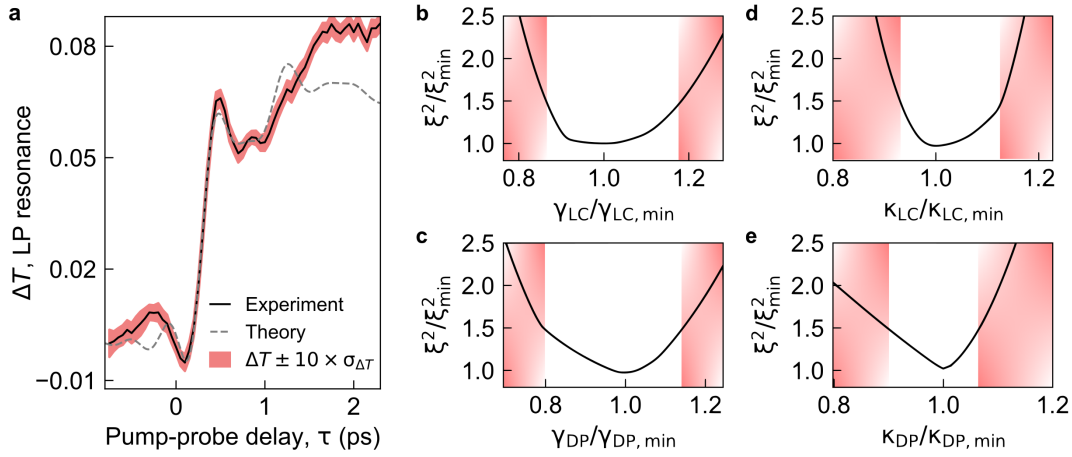

Figure A.3: Quantitative analysis of the stability of the model. (a) Differential transmission of the LP experimentally obtained (black curve) and the calculations using the optimal parameters ($\gamma_{\mathrm{LC,\,min}}$, $\gamma_{\mathrm{DP,\,min}}$, $\kappa_{\mathrm{LC,\,min}}$ and $\kappa_{\mathrm{DP,\,min}}$, see also Fig. 6.13). The red error band centred around ΔT indicates the noise level of the measurement, with the standard deviation $\sigma_{\Delta T}$. (b)-(e) Deviation of the calculation from the best-fit calculation for varied parameters of the cavity modes (γ_{LC}, γ_{DP}, κ_{LC} and κ_{DP}) relative to their optimum values ($\gamma_{\mathrm{LC,\,min}}$, $\gamma_{\mathrm{DP,\,min}}$, $\kappa_{\mathrm{LC,\,min}}$ and $\kappa_{\mathrm{DP,\,min}}$).

To estimate the range of validity of our theory, the parameter range within which the calculations agree sufficiently with the experiment was calculated. Figs. A.3b-e show the quality of the fit relative to the results for the best fit parameters used for Fig. 6.13. The differential transmission data of the calculation T_{th} and the experiment T_{exp} yield the quadratic fit deviation $\xi^2 = \int \partial\tau(\Delta T_{\mathrm{th}} - \Delta T_{\mathrm{exp}})^2$ for each parameter (γ_{LC}, γ_{DP}, κ_{LC} and κ_{DP}). $\xi^2/\xi^2_{\mathrm{min}}$ therefore quantifies the quadratic fit deviation relative to the minimum deviation, ξ^2_{min}, obtained for the best fit parameters. The red-white area marks the parameter range where the deviation from the best fit exceeds 50%, while varying a single parameter. We find that the signatures of the collapse of ultrastrong coupling are fairly stable and are qualitatively reproduced for a large range of these parameters: As sufficient interval we obtain $0.86 < \gamma_{\mathrm{LC}}/\gamma_{\mathrm{LC,min}} < 1.18$, $0.79 < \gamma_{\mathrm{DP}}/\gamma_{\mathrm{DP,min}} < 1.14$, $0.93 < \kappa_{\mathrm{LC}}/\kappa_{\mathrm{LC,min}} < 1.12$ and $0.89 < \kappa_{\mathrm{DP}}/\kappa_{\mathrm{DP,min}} < 1.06$.

Bibliography

[1]W. E. Lamb and R. C. Retherford, "Fine Structure of the Hydrogen Atom by a Mircowave Method", Phys. Rev., 241–243 (1947).

[2]S. W. Hawking, "Black hole explosions?", Nature **248**, 30–31 (1974).

[3]S. W. Hawking, "Particle Creation by Black Holes", Commun. math. Phys., 199–220 (1975).

[4]B. Odom, D. Hanneke, B. D'Urso, and G. Gabrielse, "New measurement of the electron magnetic moment using a one-electron quantum cyclotron", Phys. Rev. Lett. **97** (2006) 10.1103/PhysRevLett.97.030801.

[5]H. B. G. Casimir, "On the attraction between two perfetly conducting plates", Proc. Kon. Nederland Akad. Wetensch., 793 (1948).

[6]Y. Kaluzny, P. Goy, M. Gross, J. M. Raimond, and S. Haroche, "Observation of Self-Induced Rabi Oscillations in Two-Level Atoms Excited Inside a Resonant Cavity: The Ringing Regime of Superradiance", Phys. Rev. Lett. **51**, 1175–1178 (1983).

[7]C. Ciuti, G. Bastard, and I. Carusotto, "Quantum vacuum properties of the intersubband cavity polariton field", Phys. Rev. B **72**, 5553 (2005).

[8]S. de Liberato, C. Ciuti, and I. Carusotto, "Quantum vacuum radiation spectra from a semiconductor microcavity with a time-modulated vacuum rabi frequency", Phys. Rev. Lett. **98**, 103602 (2007).

[9]I.-C. Benea-Chelmus, C. Bonzon, C. Maissen, G. Scalari, M. Beck, and J. Faist, "Subcycle measurement of intensity correlations in the terahertz frequency range", Phys. Rev. A **93**, 043812 (2016).

[10]I.-C. Benea-Chelmus, F. F. Settembrini, G. Scalari, and J. Faist, "Electric field correlation measurements on the electromagnetic vacuum state", Nature **568**, 202–206 (2019).

[11]A. Anappara, S. de Liberato, A. Tredicucci, C. Ciuti, G. Biasiol, L. Sorba, and F. Beltram, "Signatures of the ultrastrong light-matter coupling regime", Phys. Rev. B **79** (2009) 10.1103/PhysRevB.79.201303.

[12]T. Niemczyk et al., "Circuit quantum electrodynamics in the ultrastrong-coupling regime", Nature Physics **6**, 772–776 (2010).

[13]G. Scalari et al., "Ultrastrong coupling of the cyclotron transition of a 2D electron gas to a THz metamaterial", Science **335**, 1323–1326 (2012).

[14]T. Schwartz, J. A. Hutchison, C. Genet, and T. W. Ebbesen, "Reversible Switching of Ultrastrong Light-Molecule Coupling", Phys. Rev. Lett. **106**, 196405 (2011).

[15]J. George, T. Chervy, A. Shalabney, E. Devaux, H. Hiura, C. Genet, and T. W. Ebbesen, "Multiple rabi splittings under ultrastrong vibrational coupling", Phys. Rev. Lett. **117**, 153601 (2016).

[16]F. Yoshihara, T. Fuse, S. Ashhab, K. Kakuyanagi, S. Saito, and K. Semba, "Superconducting qubit–oscillator circuit beyond the ultrastrong-coupling regime", Nature Physics **13**, 44–47 (2017).

[17]A. Bayer, M. Pozimski, S. S., D. Schuh, R. Huber, D. Bougeard, and C. Lange, "Terahertz Light-Matter Interaction beyond Unity Coupling Strength", Nano Lett. **17**, 6340–6344 (2017).

[18]G. L. Paravicini-Bagliani et al., "Magneto-transport controlled by landau polariton states", Nature Physics **15**, 186–190 (2019).

[19]X. Li, M. Bamba, Q. Zhang, S. Fallahi, G. C. Gardner, W. Gao, M. Lou, K. Yoshioka, M. J. Manfra, and J. Kono, "Vacuum Bloch–Siegert shift in Landau polaritons with ultra-high cooperativity", Nature Photonics **12**, 324–329 (2018).

[20]S. de Liberato, "Light-matter decoupling in the deep strong coupling regime: the breakdown of the Purcell effect", Phys. Rev. Lett. **112**, 016401 (2014).

[21]K. Hepp and E. H. Lieb, "On the superradiant phase transition for molecules in a quantized radiation field: the dicke maser model", Annals of Physics **76**, 360–404 (1973).

[22]Y. K. Wang and F. T. Hioe, "Phase transition in the dicke model of superradiance", Phys. Rev. A **7**, 831–836 (1973).

[23]A. F. Kockum, A. Miranowicz, V. Macri, S. Savasta, and F. Nori, "Deterministic quantum nonlinear optics with single atoms and virtual photons", Physical Review A **95**, 063849 (2017).

[24]D. Fausti, R. I. Tobey, N. Dean, S. Kaiser, A. Dienst, M. C. Hoffmann, S. Pyon, T. Takayama, H. Takagi, and A. Cavalleri, "Light-Induced Superconductivity in a Stripe-Ordered Cuprate", Science **331**, 189–191 (2011).

[25]M. Mitrano et al., "Possible light-induced superconductivity in K_3C_{60} at high temperature", Nature **530**, 461–464 (2016).

[26]M. Halbhuber, J. Mornhinweg, V. Zeller, C. Ciuti, D. Bougeard, R. Huber, and C. Lange, "Non-adiabatic stripping of a cavity field from electrons in the deep-strong coupling regime", Nature Photonics **14**, 675–679 (2020).

[27]E. M. Purcell, "Spontaneous Emission Probabilities at Radio Frequencies", Phys. Rev. B, 681 (1946).

[28]Y. Todorov, A. M. Andrews, I. Sagnes, R. Colombelli, P. Klang, G. Strasser, and C. Sirtori, "Strong Light-Matter Coupling in Subwavelength Metal-Dielectric Microcavities at Terahertz Frequencies", Phys. Rev. Lett. **102**, 186402 (2009).

[29]A. Wallraff, D. I. Schuster, A. Blais, L. Frunzio, R. S. Huang, J. Majer, S. Kumar, S. M. Girvin, and R. J. Schoelkopf, "Strong coupling of a single photon to a superconducting qubit using circuit quantum electrodynamics", Nature **431**, 162 (2004).

[30]E. T. Jaynes and F. W. Cummings, "Comparison of quantum and semiclassical radiation theories with application to the beam maser", Proceedings of the IEEE **51**, 89–109 (1963).

[31]I. I. Rabi, "Space quantization in a gyrating magnetic field", Phys. Rev. **51**, 652–654 (1937).

[32]A. Frisk Kockum, A. Miranowicz, S. de Liberato, S. Savasta, and F. Nori, "Ultrastrong coupling between light and matter", Nature Reviews Physics **1**, 19–40 (2019).

[33]J. J. Hopfield, "Theory of the Contribution of Excitons to the Complex Dielectric Constant of Crystals", Phys. Rev. **112**, 1555–1567 (1958).

[34]C. Maissen, G. Scalari, M. Beck, and J. Faist, "Asymmetry in polariton dispersion as function of light and matter frequencies in the ultrastrong coupling regime", New Journal of Physics **19**, 043022 (2017).

[35]S. Ashhab and F. Nori, "Qubit-oscillator systems in the ultrastrong-coupling regime and their potential for preparing nonclassical states", Phys. Rev. A **81**, 042311 (2010).

[36]R. H. Dicke, "Coherence in Spontaneous Radiation Processes", Phys. Rev. **93**, 99–110 (1954).

[37]A. Le Boite, M.-J. Hwang, H. Nha, and M. B. Plenio, "Fate of photon blockade in the deep strong-coupling regime", Phys. Rev. A **94**, 033827 (2016).

[38]A. Ridolfo, M. Leib, S. Savasta, and M. J. Hartmann, "Photon blockade in the ultrastrong coupling regime", Phys. Rev. Lett. **109**, 193602 (2012).

[39]S. Felicetti, G. Romero, D. Rossini, R. Fazio, and E. Solano, "Photon transfer in ultrastrongly coupled three-cavity arrays", Phys. Rev. A **89**, 013853 (2014).

[40]F. Herrera and F. C. Spano, "Cavity-Controlled Chemistry in Molecular Ensembles", Phys. Rev. Lett. **116**, 238301 (2016).

[41]J. Galego, F. J. Garcia-Vidal, and J. Feist, "Cavity-Induced Modifications of Molecular Structure in the Strong-Coupling Regime", Phys. Rev. X **5**, 041022 (2015).

[42]A. Thomas et al., "Tilting a ground-state reactivity landscape by vibrational strong coupling", Science **363**, 615–619 (2019).

[43]R. Chikkaraddy, B. d. Nijs, F. Benz, S. J. Barrow, O. A. Scherman, E. Rosta, A. Demetriadou, P. Fox, O. Hess, and J. J. Baumberg, "Single-molecule strong coupling at room temperature in plasmonic nanocavities", Nature **535**, 127–130 (2016).

[44]F. Schlawin, A. Cavalleri, and D. Jaksch, "Cavity-Mediated Electron-Photon Superconductivity", Phys. Rev. Lett. **122**, 133602 (2019).

[45]A. Thomas et al., "Exploring Superconductivity under Strong Coupling with the Vacuum Electromagnetic Field", arXiv 1911.01459v1 (2019).

[46]N. Bartolo and C. Ciuti, "Vacuum-dressed cavity magnetotransport of a two-dimensional electron gas", Phys. Rev. B **98**, 205301 (2018).

[47]E. Orgiu et al., "Conductivity in organic semiconductors hybridized with the vacuum field", Nature materials **14**, 1123–1129 (2015).

[48]J. Lolli, A. Baksic, D. Nagy, V. E. Manucharyan, and C. Ciuti, "Ancillary Qubit Spectroscopy of Vacua in Cavity and Circuit Quantum Electrodynamics", Phys. Rev. Lett. **114**, 183601 (2015).

[49]M. Cirio, K. Debnath, N. Lambert, and F. Nori, "Amplified Optomechanical Transduction of Virtual Radiation Pressure", Phys. Rev. Lett. **119**, 053601 (2017).

[50]C. M. Wilson, G. Johansson, A. Pourkabirian, M. Simoen, J. R. Johansson, T. Duty, F. Nori, and P. Delsing, "Observation of the dynamical Casimir effect in a superconducting circuit", Nature **479**, 376–379 (2011).

[51]C. Riek, P. Sulzer, M. Seeger, A. S. Moskalenko, G. Burkard, D. V. Seletskiy, and A. Leitenstorfer, "Subcycle quantum electrodynamics", Nature **541**, 376–379 (2017).

[52]M. Eisele, T. L. Cocker, M. A. Huber, M. Plankl, L. Viti, D. Ercolani, L. Sorba, M. S. Vitiello, and R. Huber, "Ultrafast multi-terahertz nano-spectroscopy with sub-cycle temporal resolution", Nature Photonics **8**, 841–845 (2014).

[53]D. Dini, R. Köhler, A. Tredicucci, G. Biasiol, and L. Sorba, "Microcavity polariton splitting of intersubband transitions", Phys. Rev. Lett. **90**, 116401 (2003).

[54]Y. Todorov, A. M. Andrews, R. Colombelli, S. de Liberato, C. Ciuti, P. Klang, G. Strasser, and C. Sirtori, "Ultrastrong light-matter coupling regime with polariton dots", Phys. Rev. Lett. **105** (2010) 10.1103/PhysRevLett.105.196402.

[55]C. Maissen, G. Scalari, F. Valmorra, M. Beck, J. Faist, S. Cibella, R. Leoni, C. Reichl, C. Charpentier, and W. Wegscheider, "Ultrastrong coupling in the near field of complementary split-ring resonators", Phys. Rev. B **90** (2014) 10.1103/PhysRevB.90.205309.

[56]A. Baust et al., "Ultrastrong coupling in two-resonator circuit QED", Phys. Rev. B **93** (2016) 10.1103/PhysRevB.93.214501.

[57]F. Benz et al., "Single-molecule optomechanics in picocavities", Science **354**, 726–729 (2016).

[58]B. Askenazi, A. Vasanelli, Y. Todorov, E. Sakat, J.-J. Greffet, G. Beaudoin, I. Sagnes, and C. Sirtori, "Midinfrared Ultrastrong Light–Matter Coupling for THz Thermal Emission", ACS Photonics **4**, 2550–2555 (2017).

[59]F. Barachati, J. Simon, Y. A. Getmanenko, S. Barlow, S. R. Marder, and S. Kéna-Cohen, "Tunable Third-Harmonic Generation from Polaritons in the Ultrastrong Coupling Regime", ACS Photonics **5**, 119–125 (2018).

[60]N. S. Mueller, Y. Okamura, B. G. M. Vieira, S. Juergensen, H. Lange, E. B. Barros, F. Schulz, and S. Reich, "Deep strong light–matter coupling in plasmonic nanoparticle crystals", Nature **583**, 780–784 (2020).

[61]J. Keller, G. Scalari, S. Cibella, C. Maissen, F. Appugliese, E. Giovine, R. Leoni, M. Beck, and J. Faist, "Few-Electron Ultrastrong Light-Matter Coupling at 300 GHz with Nanogap Hybrid LC Microcavities", Nano Lett. **17**, 7410–7415 (2017).

[62]I. Vurgaftman, J. R. Meyer, and L. R. Ram-Mohan, "Band parameters for III–V compound semiconductors and their alloys", Journal of Applied Physics **89**, 5815–5875 (2001).

[63]C. Cohen-Tannoudji, *Quantum Mechanis Volume 1* (John Wiley and Sons, 1977).

[64]L. D. Landau, "Diamagnetismus der Metalle", Zeitschrift für Physik **64**, 629–637 (1930).

[65]D. Hagenmüller, S. de Liberato, and C. Ciuti, "Ultrastrong coupling between a cavity resonator and the cyclotron transition of a two-dimensional electron gas in the case of an integer filling factor", Phys. Rev. B **81** (2010) 10.1103/PhysRevB.81.235303.

[66]H.-T. Chen, A. J. Taylor, and N. Yu, "A review of metasurfaces: physics and applications", Reports on Progress in Physics **79** (2016).

[67]H. O. Moser, B. D. F. Casse, O. Wilhelmi, and B. T. Saw, "Terahertz Response of a Microfabricated Rod–Split-Ring-Resonator Electromagnetic Metamaterial", Phys. Rev. Lett. **94**, 063901 (2005).

[68]J. B. P. et al, "Magnetism from Conductors and Enhanced Nonlinear Phenomena", IEEE Transactions on Microwave Theory and Techniques (1999).

[69]H.-T. Chen, J. F. O'Hara, A. J. Taylor, R. D. Averitt, C. Highstrete, M. Lee, and W. J. Padilla, "Complementary planar terahertz metamaterials", Optics express **15**, 1084–1095 (2007).

[70]L. Diebel, "Jenseits ultrastarker Licht-Materie-Kopplung: Subzyklen-Kontrolle von Vakuumfeldern in neuartigen THz-Resonatoren", MA thesis (Universität Regensburg, 2020).

[71]E. D. Palik and J. K. Furdyna, "Infrared and microwave magnetoplasma effects in semiconductors", Rep. Prog. Phys. **33** (1970).

[72]J. A. Stratton and L. J. Chu, "Diffraction Theory of Electromagnetic Waves", Phys. Rev. **56**, 99–107 (1939).

[73]M. Henini, *Molecular beam epitaxy* (Elsevier, 2018).

[74]S. Adachi, "GaAs, AlAs, and $Al_xGa_{1-x}As$: Material parameters for use in research and device applications", Journal of Applied Physics **58**, R1–R29 (1985).

[75]K. Inoue, J. Harmand, and T. Matsuno, "High-quality $In_xGa_{1-x}As$/InAlAs modulation-doped heterostructures grown lattice-mismatched on GaAs substrates", Journal of Crystal Growth **111**, 313–317 (1991).

[76]L. J. van der Pauw, "A method of measuring the resistivity and hall coefficient on lamellae of arbitrary shape", Philips Technical Review **20**, 220–224 (1958).

[77]P. Drude, "Zur Elektronentheorie der Metalle", Annalen der Physik **306**, 566–613 (1900).

[78]T. Ihn, *Semiconductor Nanostructures: Quantum states and electronic transport* (Oxford University Press, 2010).

[79]F. Langer, "Lightwave-driven quasipatricle acceleration", PhD thesis (Universität Regensburg, 2018).

[80]J. Mornhinweg, "Subcycle THz Switching of Ultrastrong Light-Matter Coupling", MA thesis (Universität Regensburg, 2018).

[81]S. Dexheimer, *Terahertz Spectroscopy: Principles and Applications* (Taylor and Francis Group, 2007).

[82]R. W. Boyd, *Nonlinear optics*, Fourth edition (Academic Press, 2019).

[83]R. Huber, A. Brodschelm, F. Tauser, and A. Leitenstorfer, "Generation and field-resolved detection of femtosecond electromagnetic pulses tunable up to 41 THz", Applied Physics Letters **76**, 3191–3193 (2000).

[84]M. Knorr, J. Raab, M. Tauer, P. Merkl, D. Peller, E. Wittmann, E. Riedle, C. Lange, and R. Huber, "Phase-locked multi-terahertz electric fields exceeding 13 MV/cm at a 190 kHz repetition rate", Opt. Lett. **42**, 4367–4370 (2017).

[85]K. Reimann, "Table-top sources of ultrashort THz pulses", Reports on Progress in Physics **70**, 1597–1632 (2007).

[86]A. Leitenstorfer, S. Hunsche, J. Shah, M. C. Nuss, and W. H. Knox, "Detectors and sources for ultrabroadband electro-optic sampling: Experiment and theory", Applied Physics Letters **74**, 1516–1518 (1999).

[87]Q. Wu and X. Zhang, "Free-space electro-optic sampling of terahertz beams", Applied Physics Letters **67**, 3523–3525 (1995).

[88]A. Yariv, *Quantum Electronics* (Wiley, 1988).

[89]R. Huber, "Ultraschneller Aufbau von Coulomb-Korrelationen untersucht mit Femtosekunden-Terahertz-Spektroskopie", PhD thesis (Technische Universität München, 2004).

[90]F. Blanchard et al., "Generation of 1.5 μJ single-cycle terahertz pulses by optical rectification from a large aperture ZnTe crystal", Opt. Express **15**, 13212–13220 (2007).

[91]D. J. Kane and R. Trebino, "Characterization of arbitrary femtosecond pulses using frequency-resolved optical gating", IEEE Journal of Quantum Electronics **29**, 571–579 (1993).

[92]J. T. Kindt and C. A. Schmuttenmaer, "Theory for determination of the low-frequency time-dependent response function in liquids using time-resolved terahertz pulse spectroscopy", The Journal of Chemical Physics **110**, 8589–8596 (1999).

[93]A. Bayer, "Ultrastrong thz light-matter interaction in custom-tailored semiconductor heterostructures", PhD thesis (Universität Regensburg, 2017).

[94]L. Pfeiffer, K. W. West, H. L. Stormer, and K. W. Baldwin, "Electron mobilities exceeding $10^7 cm^2$/Vs in modulation-doped GaAs", Applied Physics Letters **55**, 1888–1890 (1989).

[95]C. M. Hurd, S. P. McAlister, W. R. McKinnon, B. R. Stewart, D. J. Day, P. Mandeville, and A. J. SpringThorpe, "Modeling parallel conduction in GaAs/$Al_xGa_{1-x}As$ heterostructures", Journal of Applied Physics **63**, 4706–4713 (1988).

[96]U. Ekenberg, "Nonparabolicity effects in a quantum well: Sublevel shift, parallel mass, and Landau levels", Phys. Rev. B **40**, 7714–7726 (1989).

[97]M. Gross and S. Haroche, "Superradiance: an essay on the theory of collective spontaneous emission", Physics Reports **93**, 301–396 (1982).

[98]Q. Zhang et al., "Superradiant Decay of Cyclotron Resonance of Two-Dimensional Electron Gases", Phys. Rev. Lett. **113**, 047601 (2014).

[99]H. Kroemer, "The 6.1A family (InAs, GaSb, AlSb) and its heterostructures: A selective review", Physica E **20** (2004) 10.1016/j.physe.2003.08.003.

[100]G. Tuttle, H. Kroemer, and J. H. English, "Electron concentrations and mobilities in AlSb/InAs/AlSb quantum wells", Journal of Applied Physics **65**, 5239 (1989).

[101]C. Nguyen, B. Brar, C. R. Bolognesi, J. J. Pekarik, H. Kroemer, and J. H. English, "Growth of InAs-AlSb quantum wells having both high mobilities and high concentrations", Journal of Electronic Materials **22**, 255–258 (1993).

[102]T. Akazaki, J. Nitta, H. Takayanagi, T. Enoki, and K. Arai, "Improving the mobility of an $In_{0.52}Al_{0.48}As/In_{0.53}Ga_{0.47}As$ inverted modulation-doped structure by inserting a strained InAs quantum well", Applied Physics Letters **65**, 1263–1265 (1994).

[103]A. Richter, M. Koch, T. Matsuyama, C. Heyn, and U. Merkt, "Transport properties of modulation-doped InAs-inserted-channel $In_{0.75}Al_{0.25}As/In_{0.75}Ga_{0.25}As$ structures grown on GaAs substrates", Applied Physics Letters **77**, 3227–3229 (2000).

[104]M. Trottman, "Characterisation of III-Vsemiconductor hybrid systems for spinorbitronic functionality", PhD thesis (Universität Regensburg, 2020).

[105]J. Loher, "Two-dimensional hole systems in Indium-based quantum well heterostructures", PhD thesis (Universität Regensburg, 2015).

[106]F. Capotondi, G. Biasiol, D. Ercolani, V. Grillo, E. Carlino, F. Romanato, and L. Sorba, "Strain induced effects on the transport properties of metamorphic InAlAs/InGaAs quantum wells", Thin Solid Films **484**, 400–407 (2005).

[107]L. L. Chang and L. Esaki, "Electronic properties of InAs-GaSb superlattices", Surface Science **98**, 70–89 (1980).

[108]C. Charpentier, "Molecular beam epitaxial growth of high-quality Sb-based III /V semiconductor heterostructures", PhD thesis (ETH Zurich, 2014).

[109]C. Nguyen, B. Brar, H. Kroemer, and J. H. English, "Surface donor contribution to electronsheet concentrations in not-intentionally doped InAs-AlSb quantum wells", Appl. Phys. Lett. **60**, 1854 (1992).

[110]R. Venkatasubramanian, D. L. Dorsey, and K. Mahalingam, "Heuristic rules for group IV dopant site selection in III–V compounds", Journal of Crystal Growth **175-176**, Molecular Beam Epitaxy 1996, 224–228 (1997).

[111]B. Bennett, M. Yang, B. Shanabrook, J. Boos, and D. Park, "Modulation doping of InAs/AlSb quantum wells using remote InAs donor layers", Applied Physics Letters **72**, 1193–1195 (1998).

[112]C. Gauer, J. Scriba, A. Wixforth, J. P. Kotthaus, C. R. Bolognesi, C. Nguyen, B.Brar, and H. Kroemer, "Energy-dependant cyclotron mass in InAs/AlSb quantum wells", Semiconductor Science and Technology **9**, 1580–1583 (1994).

[113]V. Zeller, "Ultrastrong light-matter coupling in Landau-quantized electron systems", MA thesis (University of Regensburg, 2019).

[114]S. S. Krishtopenko, A. V. Ikonnikov, A. V. Maremyanin, K. E. Spirin, V. I. Gavrilenko, Y. G. Sadofyev, M. Goiran, M. Sadowsky, and Y. B. Vasilyev, "Cyclotron resonance study in InAs/AlSb quantum well heterostructures with two occupied electronic subbands", Journal of Applied Physics **111**, 093711 (2012).

[115]J. Keller et al., "Landau polaritons in highly nonparabolic two-dimensional gases in the ultrastrong coupling regime", Phys. Rev. B **101**, 075301 (2020).

[116]J. Keller, G. Scalari, F. Appugliese, E. Mavrona, S. Rajabali, M. J. Süess, M. Beck, and J. Faist, "High T_c Superconducting THz Metamaterial for Ultrastrong Coupling in a Magnetic Field", ACS Photonics **5**, 3977–3983 (2018).

[117]G. Scalari, C. Maissen, S. Cibella, R. Leoni, P. Carelli, F. Valmorra, M. Beck, and J. Faist, "Superconducting complementary metasurfaces for THz ultrastrong light-matter coupling", New Journal of Physics **16**, 033005 (2014).

[118]G. Günter et al., "Sub-cycle switch-on of ultrastrong light-matter interaction", Nature **458**, 178–181 (2009).

[119]Q. Zhang, M. Lou, X. Li, J. L. Reno, W. Pan, J. D. Watson, M. J. Manfra, and J. Kono, "Collective non-perturbative coupling of 2D electrons with high-quality-factor terahertz cavity photons", Nature Physics **12**, 1005–1011 (2016).

[120]M. R. Hashemi, S. Cakmakyapan, and M. Jarrahi, "Reconfigurable metamaterials for terahertz wavemanipulation", Reports on Progress in Physics **80**, 094501 (2017).

[121]D. Shrekenhamer, S. Rout, A. C. Strikwerda, C. Bingham, R. D. Averitt, S. Sonkusale, and W. J. Padilla, "High speed terahertz modulation from metamaterials with embedded highelectron mobility transistors", OPTICS EXPRESS **19** (2011).

[122]H.-T. Chen, W. J. Padilla, J. M. O. Zide, A. C. Gossard, A. J. Taylor, and R. D. Averitt, "Active terahertz metamaterial devices", Nature **444**, 597–600 (2006).

[123]W. Zhu, A. Liu, T. Bourouina, D. Tsai, J. Teng, X. Zhang, G. Lo, D. Kwong, and N. Zheludev, "Microelectromechanical maltese-crossmetamaterial with tunable terahertz anisotropy", Nature Communications **3**, 1274 (2012).

[124]K. Shih, P. Pitchappa, M. Manjappa, C. P. Ho, R. Singh, B. Yang, NavabSingh, and C. Lee, "Active MEMS metamaterials for THz bandwidth control", Appl. Phys. Lett. **110**, 161108 (2017).

[125]R. Singh, J. Xiong, A. K. Azad, H. Yang, S. A. Trugman, Q. X. Jia, A. J. Taylor, and H.-T. Chen, "Optical tuning and ultrafast dynamics of high-temperature superconducting terahertz metamaterials", Nanophotonics **1**, 117–123 (2012).

[126]X. Liu, H. Liu, Q. Sun, and N. Huang, "Metamaterial terahertz switch based on split-ring resonator embedded withphotoconductive silicon", Applied Optics **54** (2015).

[127]H.-T. Chen, J. F. O'Hara, A. K. Azad, A. J. Taylor, R. D. Averitt, D. B. Shrekenhamer, and W. J. Padilla, "Experimental demonstration of frequency-agile terahertz metamaterials", Nature Photonics **2**, 295–298 (2008).

[128]M. Kafesaki, N. H. Shen, S. Tzortzakis, and C. M. Soukoulis, "Optically switchable and tunable terahertz metamaterials through photoconductivity", Journal of Optics **14** (2012) 10.1088/2040-8978/14/11/114008.

[129]Y. Hu et al., "Ultrafast Terahertz Frequency and Phase Tuning by All–Optical Molecularization of Metasurfaces", Advanced Optical Materials **7** (2019) 10.1002/adom.201901050.

[130]W. J. Padilla, A. J. Taylor, C. Highstrete, M. Lee, and R. D. Averitt, "Dynamical Electric and Magnetic Metamaterial Response at Terahertz Frequencies", Physical Review Letters **96**, 107401 (2006).

[131]R. Huber, F. Tauser, A. Brodschelm, M. Bichler, G. Abstreiter, and A. Leitenstorfer, "How many-particle interactions develop after ultrafast excitation of an electron–hole plasma", Nature **414**, 286–289 (2001).

[132]B. Fluegel, N. Peyghambarian, G. Olbright, M. Lindberg, S. W. Koch, M. Joffre, D. Hulin, A. Migus, and A. Antonetti, "Femtosecond Studies of Coherent Transients in Semiconductors", Phys. Rev. Lett. **59**, 2588–2591 (1987).

[133]J. Mornhinweg, M. Halbhuber, C. Ciuti, D. Bougeard, R. Huber, and C. Lange, "Tailored subcycle nonlinearities of ultrastrong light-matter coupling", Manuscript submitted for publication. (2020).

[134]U. Wurstbauer, "Herstellung und Charakterisierung von Mangan dotierten III–V Halbleiterheterostrukturen", PhD thesis (Universität Regensburg, 2008).

[135]C. Gerl, "Hochbewegliche zweidimensionale Lochsysteme in GaAs/AlGaAs Heterostrukturen", PhD thesis (Universität Regensburg, 2009).

[136]M. Utz, "Epitaxie von (Ga,Mn)As", PhD thesis (Universität Regensburg, 2012).

[137]M. Prager, "Realisation of near-surfacetwo-dimensional electron gases ininas-based quantum wells", MA thesis (Universität Regensburg, 2018).

Acknowledgements

At the end of this work, I would like to express my gratitude for the extensive support I received during my thesis. In particular, I would like to thank the following persons without whom this work would not have come about:

Prof. Dominique Bougeard for offering the opportunity to join his group and participate in this exciting research project. I want to express my gratitude for the excellent supervision and for being available for inspiring scientific discussions and help at any time.

Prof. Christoph Lange for the experimental supervision, his expertise in numerical simulations and constant flow of new ideas. I especially want to thank him for including me in the USC-team and the numerous discussions we had.

Prof. Rupert Huber for granting access to the cutting edge spectroscopy setup and other scientific laboratories and of course for the interesting and fruitful discussions about experimental results.

Joshua Mornhinweg for the cooperation in every part of my doctoral thesis and for sharing his knowledge about spectroscopy techniques and computers.

Viola Zeller for her great work and design ideas which substantially forwarded our research project. I also really cherish the time we spent training various skills.

Laura Diebel for the collaboration in different laboratories, her knowledge of Comsol and of course the design of the Butterfly-resonator. I also highly appreciate the time spent apart from work.

Michael Prager for the growth and electrical characterisation of InAs-based heterostructures, his constant help regardless of the topic and the sharing of memes.

Dr. Dieter Schuh, Imke Gronwald, Martin Fruthmayer for their help in a wide variety of aspects.

Jürgen Raab for his knowledge of THz-spectroscopy, fruitful discussions, answering stupid questions and especially for the time we spent in the coffee kitchen.

Christoph Schmied, Stefan Schlauderer and Josef Riepl for the support and sometimes fun in the kHz-laboratory.

Thomas Mayer for numerous discussions on different topics and the great time in and out of the office.

Dr. Andreas Bayer for his great ground work regarding ultrastrong coupling and MBE growth.

The whole AG Bougeard for three amazing years.

My family and Michael for the constant support and everything.